Understanding and Improving Hole Transport in Hydrogenated Amorphous Silicon Photovoltaics

by

Eric C. Johlin

B.S., California Institute of Technology (2009)
S.M., Massachusetts Institute of Technology (2012)

Submitted to the Department of Mechanical Engineering
in partial fulfillment of the requirements for the degree of

Doctor of Philosophy in Mechanical Engineering and Computation

at the

MASSACHUSETTS INSTITUTE OF TECHNOLOGY

September 2014

Signature redacted

Author .....
Department of Mechanical Engineering
August 4, 2014

Certified by ..... Signature redacted
Jeffrey C. Grossman
Professor of Material Science and Engineering
Thesis Supervisor

Certified by ..... Signature redacted
Tonio Buonassisi
Associate Professor of Mechanical Engineering
Thesis Supervisor

Signature redacted

Accepted by .....
David Hardt, Professor of Mechanical Engineering
Chairman, Department Committee for Graduate Studies

Understanding and Improving Hole Transport in Hydrogenated Amorphous Silicon Photovoltaics

by

Eric C. Johlin

Submitted to the Department of Mechanical Engineering
on August 4, 2014, in partial fulfillment of the
requirements for the degree of
Doctor of Philosophy in Mechanical Engineering and Computation

Abstract

While hydrogenated amorphous silicon (a-Si:H) solar cells have been studied extensively for the previous four decades, the low performance of the devices is still not well understood. The poor efficiency (below 10%, even in research-scale devices) is believed to be mainly due to the low hole mobility of the bulk material, but there is little is known about the physical phenomena responsible for this deficient mobility. This work explores the atomic structures causing the inefficient hole transport in a-Si:H, as well as a novel rout toward improvement.

First, a large ensemble of computational a-Si:H structures (216 Si atoms, with ~10% H) is created, representing over 600,000 atoms. This ensemble is analyzed using density-functional theory (DFT) calculations, and statistical correlations are made between discovered defective atomic structures and strong hole trapping. It is observed that a self-trapping defect arising from a reversible atomic rearrangement in the presence of a hole is most strongly correlated with deep trapping, followed by floating bonds, or over-coordinated silicon defects. Dangling bonds, or under-coordinated silicon defects, despite their traditional indictment for the responsibility of trapping in the literature, are found not to correlate with strong hole traps.

Experimental films are produced using plasma enhanced chemical vapor deposition (PECVD), in *p-i-n* solar cell device configurations. By varying the chamber pressure, a set of devices with widely ranging properties are produced, varying hydrogen content and bonding configuration, stress, and density. These devices are then characterized using time-of-flight (ToF) photocurrent-transient measurements, allowing the direct measurement of hole transport though the intrinsic layer, and thereby the calculation of the material hole mobility. It is found that the peak mobility occurs at both intermediate (compressive) stress and hydrogen contents, with rapid linear declines in mobility as this maximum is deviated from (with respect to film stress).

The computational ensemble of a-Si:H is then extended to include the experimentally-observed variables of stress and hydrogen concentration. A second ensemble of lower hydrogen content (~5%) is created, and both hydrogen contents are relaxed at three differing stress states (-1, 0 and +1 GPa), extending the full

simulation to approximately 2 million atoms across over 8 thousand structures. It is found that the modification of the stress and hydrogen content of computational samples correlates to shifting regimes of defect prevalence - increased hydrogen content and increasing compressive stress are both correlated with increased floating bond concentration. Low absolute values of stress correspond to increased ionization displacement defects. High tensile stress is observed to increase strong hole traps, without substantial increases in any of the previously explored defects, which is attributed to lattice expansion allowing further hole delocalization around trapping structures which would be otherwise less favorable due to the high kinetic penalty of strong wavefunction confinement. These relationships are then correlated to the aforementioned experimental results, and further experimentally vetted, where possible.

Finally, as the observed shifting nature of defects in a-Si:H makes the further improvement of the bulk material untenable, methods are explored for utilizing the beneficial properties of the material (namely the strong bulk absorption and robust surface states) to achieve improved hole extraction (or effective mobility) from devices. Specifically, nanohole structured hydrogenated amorphous silicon (nha-Si:H) devices are created as a proof-of-concept, showing up to 50% increases in efficiency over equivalent planar devices, for low-performing materials.

Thesis Supervisor: Jeffrey C. Grossman
Title: Professor of Material Science and Engineering

Thesis Supervisor: Tonio Buonassisi
Title: Associate Professor of Mechanical Engineering

Acknowledgments

First and foremost I would like to thank my advisors, Profs. Jeff Grossman and Tonio Buonassisi. They have both been invaluable in my time here, and have provided a fantastic graduate experience. I was warned extensively when first starting at MIT against being co-advised, as it was assumed that the increased load of meetings, group responsibilities and conflicting demands from the two PIs would make the experience miserable. I am exceedingly glad that I ignored these warnings – the actual situation could not be further from "miserable." While there were naturally a somewhat larger number of meetings, group responsibilities, as well as the occasional miscommunication of priorities, these were massively eclipsed by the complementary knowledge and attitudes, as well as tireless support and encouragement that Tonio and Jeff provided. The constant remarks in the last few months during my PhD of coworkers asking "Why are you still here?! You can graduate!" coupled with my reluctance to leave, may be the best testament to how Jeff and Tonio, as well as their respective groups, made my time here unquestionably wonderful.

Next I would like to thank my collaborators and friends. First, working with Dr. Christie Simmons was one of the true highlights of my research here. Although we did not work together on the same project for long, her guidance benefited my learning immensely, and made my work much more enjoyable. I am also grateful to Lucas Wagner and Ahmed Al-Obeidi for their help with my computational work, and interference lithography, respectively. I would also like to thank: my collaborators at KFUPM for their support, hospitality, and scientific assistance, particularly Prof. Nouar Tabet, Prof. Syed Said, Dr. Amir Abdallah, and Dr. Tesleem Asafa; my collaborators on the project at MIT – Prof. Alexie Kolpak, Dr. Davide Strubbe, Prof.

Tim Mueller, Jonathan Mailoa, Dr. Niall Mangan, and Dr. Tim Kirkpatrick for their helpful assistance and discussions; my roommates, James (Russell) McClellan, Ronan Lonergan, Amit Gandhi and Tamas Szalay for their friendship, encouragement, and patience on the inevitable days when I'd come home frustrated from failed experiments or just spending too much time in the cleanroom; and my good friends Natasha (Al) Cayco Gajic, Katherine Smyth, Howard Kang, and Jennifer Scherer, for their incredible compassion and enrichment of my life, and willingness to listen to my undoubtedly mind-numbing monologues on my research.

Finally I want to thank my parents for being so amazingly supportive throughout my entire academic career, and life in general, and providing the countless opportunities to me which made this all possible.

Contents

List of Figures

List of Tables

References to Published Works

The exploration of the influences of atomic structure on hole trapping in Chapter 2 follows the publication:

> E. Johlin, L. K. Wagner, T. Buonassisi, and J. C. Grossman, "Origins of Structural Hole Traps in Hydrogenated Amorphous Silicon." Phys. Rev. Lett. 110, 146805 (2013).

The work related to the time-of-flight measurements in Chapter 3 and connection of experimental hole mobility to computed hole trap depths and atomic defects in Chapter 4 follow the publication:

> E. Johlin, C.B. Simmons, T. Buonassisi, and J.C. Grossman, "Hole-Mobility-Limiting Atomic Structures in Hydrogenated Amorphous Silicon." Phys. Rev. B. Accepted. (2014).

Nanohole structuring, the experiments thereof and the computational simulation of the devices found in Chapter 5 appear in:

> E. Johlin, A. Al-Obeidi, T. Buonassisi, and J.C. Grossman, "Nanohole Structuring for Improved Hole Transport in Hydrogenated Amorphous Silicon Photovoltaic Devices." In Preparation (2014).

The work herein has also appeared in the following presentations:

> "Nanohole Structuring of Hydrogenated Amorphous Silicon for Photovoltaic Applications." Spring MRS Meeting, San Francisco, CA, 25 April 2014.

"Influence of Structural Phenomena on Time-of-flight Hole Mobility in Hydrogenated Amorphous Silicon Thin Films." Fall MRS Meeting, Boston, MA, 28 November 2012.

"Stress-Based Mitigation of Strong Hole Traps in Hydrogenated Amorphous Silicon." Spring MRS Meeting, San Francisco, CA, 10 April 2012.

"Statistical Diagnosis and Mitigation of Structural Hole Traps in Hydrogenated Amorphous Silicon." Spring MRS Meeting, San Francisco, CA, 27 April 2011.

"Density Functional Theory Calculations of the Role of Defects in Amorphous Silicon Solar Cells." APS March Meeting, Portland, OR, 15 March 2010.

Chapter 1

Introduction

1.1 Why Photovoltaics?

World energy consumption is predicted to increase by 40% over the next 20 years – by 2034 use is anticipated to be at over 750 quadrillion BTU annually [1]. Concomitantly, the need to not only slow the rise of global CO_2 emissions, but to actually reduce their production in order to curb climate change has become increasingly clear [2]. The requirement of meeting this rising demand, coupled with the need for carbon-free energy production necessitates the investment in new energy sources.

Furthermore, it is becoming indisputable that non-renewable energy cannot provide even a moderate-term solution, as evidence mounts that the depletion of global fossil and nuclear fuel resources is approaching. Examining the total global energy resources in Fig. 1-1, we see the total remaining supplies of fossil fuels (gray-scale) dwarfed in scale by the mere annual availability of renewable energy sources. Recent models predict total depletion of all global fossil fuel resources by 2112, with only coal remaining after 2042 [3]. This further solidifies the need to transition to renewable energy sources in the near term.

The yellow cube superscribing the entirety of other all other known energy resources in Fig. 1-1 represents the energy from solar irradiation on the continents of earth in a single year. The enormity of this readily capturable and widely available source of

power suggests that solar energy is an ideal candidate to meet these needs for high levels of carbon-free energy production.

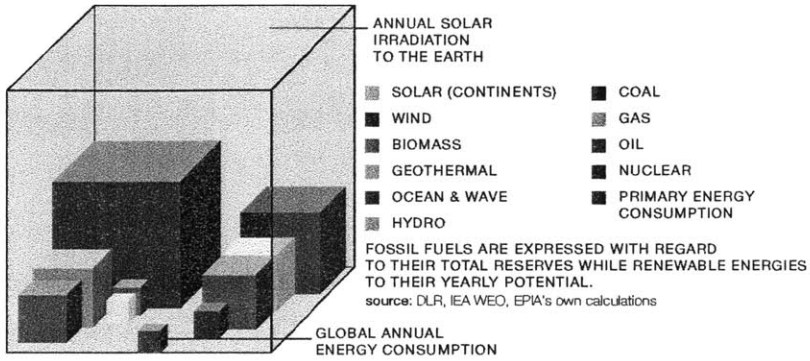

Figure 1-1: Comparison of anticipated total global resources of fossil and nuclear fuels, as well as a annual resource of renewable energy sources, with the 2011 estimated global energy consumption indicated in orange. Reproduced from [4]

In order to efficiently utilize this resource however, solar energy must be converted to a usable form, ideally electricity, in a cost-effective manner, with photovoltaics being the most direct, and often best method of achieving this. While photovoltaics are becoming increasingly attractive from a cost-per-watt perspective, the price of the bulk absorber material still represents a considerable fraction of the cost of a full photovoltaic module [5].

1.2 Why a-Si?

Hydrogenated amorphous silicon (a-Si:H) was studied widely in the late 1980s and early 1990s, when PV was just becoming inexpensive enough to put into small calculators other consumer devices. Fig. 1-2 shows the annual output of journal publication on amorphous silicon (results for papers containing "amorphous silicon," or "a-Si" in their titles), as well this same trend normalized to an approximate 2.6% yearly growth in the number of scientific publications worldwide [6]; the rapid peak and then slow decline of publications can be seen, even with the recent boost of interest the material has received in study for its use in passivization of crystalline silicon

devices. This diminishing excitement seems to be largely correlated with the limited efficiency improvements in these devices, slowing to a standstill at a 13.4 % efficiency for multi-junction a-Si cells (including nc-Si layers) as shown in Fig. 1-2, and the current 10.1% record for single-junction, purely a-Si:H cells, achieved in 2009 [7]. While we are beginning to understand the causes of this stagnation of efficiency improvements, let's first look into why the material is of interest to photovoltaic development to begin with.

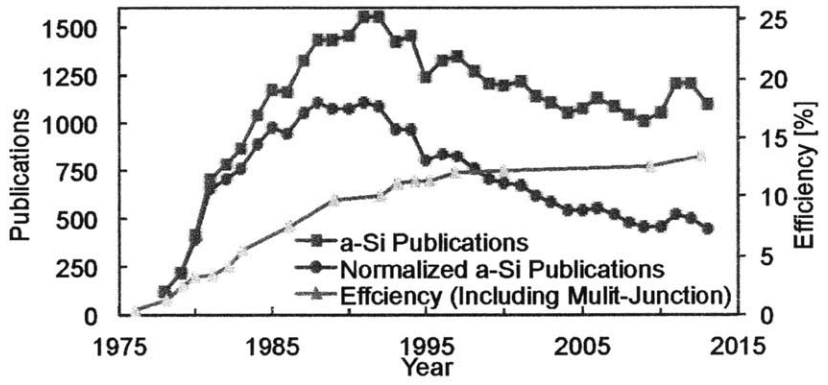

Figure 1-2: Approximate number of amorphous silicon journal publications per year, along with same data normalized to an estimated 2.6% annual increase in publication output, plotted along side a-Si:H device efficiency over time, including multi-junction devices incorporating nc-Si layers. Efficiency data from: http://www.nrel.gov/ncpv/images/efficiency_chart.jpg

1.2.1 Advantages of a-Si:H

One significant advantage of a-Si:H over its crystalline counterpart is the low cost of the material itself – films are deposited from silane (SiH_4), directly from the gas phase, precluding the requirements of multi-stage purification, melting and resizing (sawing) necessary for the production of the more popular crystalline silicon photovoltaic devices. There exist multiple methods of depositing a-Si:H from vapor, but first method used to produce the material is still the most common today [8]. Plasma enhanced chemical vapor deposition decomposes silane (SiH_4) into SiH_3 radicals, which then form the surface layer of the growing film, allowing for the potential for significant

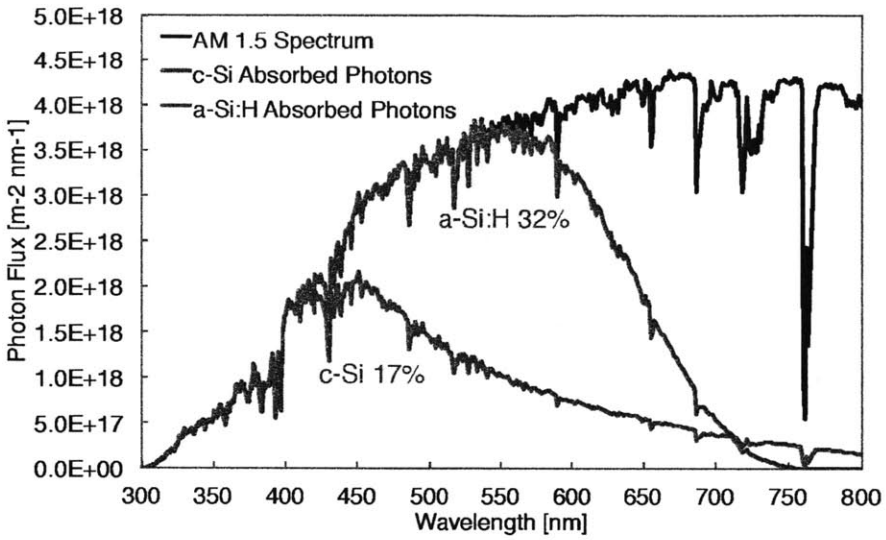

Figure 1-3: Comparison of the number of photons absorbed from the AM1.5 spectrum by 500 nm thick layers of c-Si and a-Si:H. The c-Si absorption data is from Ref. [11].

incorporation of hydrogen into the amorphous silicon films [9]. Deposition pressure, power, temperature and the frequency driving the plasma all influence the ion energy of the species bombarding the substrate to produce the growing film, and the variation of these parameters can thereby alter many of the film properties, including hydrogen content, bonding configurations, film density, porosity, and intrinsic stress (see Ref. [10]). This incorporation of hydrogen improves the electrical properties of a-Si:H beyond those of pure a-Si (which can be deposited via sputtering or ion implantation of silicon into crystalline silicon). The reasons for this improvement are still under some debate, but with the prevailing theory being the passivization of otherwise-present dangling bonds. Furthermore, hydrogen gas can be added to the silane source, the dilution of which can substantially modify the hydrogen content as well, although often not in a straightforward manner – moderate hydrogen dilution will actually often reduce hydrogen content in films, compared to a pure silane deposition, as the additional hydrogen plasma is believed to selectively etch hydrogen from the SiH_3 forming layer composing the surface of the films. [8]

A second advantage of a-Si:H films also comes from this deposition method – the use of RF plasma to aid in the decomposition of silane into the radicals that produce the film allows a-Si:H devices to be formed at low temperatures, often below 200° C, and thereby on a wide variety of substrates, including glasses, plastics, and metals. The vapor-phase formation of the films also allows for coating of textured, or otherwise non-uniform or flat surfaces, as well as on flexible or curved substrates. As balance-of-systems components are becoming a significant factor in the costs of traditional photovoltaic systems (standard glass and aluminum frame modules), novel, applications-incorporated PV devices (product- or building-integrated) are becoming increasingly attractive.

Many material properties of a-Si:H are also quite ideal: first, the strong optical absorption of the material allows very thin devices to be made while still absorbing a large fraction of the visible spectrum. We demonstrate this in Fig. 1-3, comparing the absorption of a 500 nm thick layer of a-Si:H to that of c-Si (neglecting reflection in either case). While the crystalline silicon material absorbs approximately 17% of the incident photons in the AM 1.5 spectrum, the amorphous material absorbs almost twice as much, at 32% [11]. This increase in absorption is due to the direct band gap of the material (a photon does not require a phonon to be absorbed, due to the lack of a need for a transition in momentum-space for absorption in a-Si, as present in c-Si). This can be observed in Fig. 1-3, as the direct transition in crystalline silicon occurs at ~3.4 eV, corresponding to ~365 nm light, and it is seen that at around this wavelength the absorption of the two materials begins to diverge. This increased absorption allows a-Si:H devices to be made much thinner than those of c-Si, thereby using less material, and compounding the cost savings further. This thinness also allows devices made of a-Si:H to be far more flexible than a thicker crystalline material, further adding to the potential for novel applications.

The electronic band gap in hydrogenated amorphous silicon is also quite ideal, and the variable nature of the physical properties of the material also allows some tuning of the band gap. Gap energies from ~1.5 eV up to 1.75 eV are possible. These are represented in Fig. 1-4 as the width of the red rectangle. This allows a

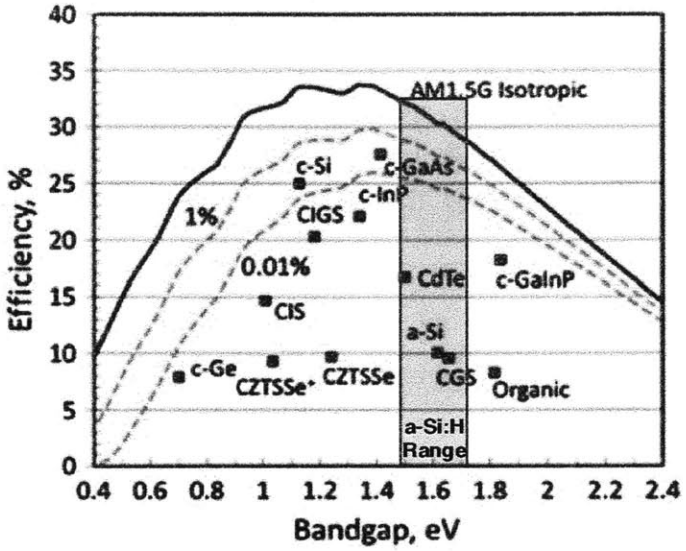

Figure 1-4: Theoretical efficiency (Shockley-Queisser limit) as a function of absorber band gap. Dashed lines show the limits for radiative efficiencies of 1 and 0.01%. Red box shows the range of possible band gaps in a-Si:H. Adapted from Ref. [12].

Shockley-Queisser efficiency limit of the material of almost 33%, similar to that of c-Si. Furthermore, as more reasonable levels of radiative recombination are assumed, the relative efficiency to c-Si slightly increases. The tunability of the a-Si:H band gap, especially when nanocrystalline silicon (nc-Si:H, a material similar to a-Si:H in terms of deposition, but including small crystallites in the amorphous matrix, and a more narrow band gap) is included, allows for easily deposited multijunction cells of even higher theoretical efficiencies.

1.2.2 Issues with a-Si:H

As mentioned before, despite these quite ideal properties, the efficiencies of a-Si:H materials remain around 10% for small area, research devices, and only around 8% for actual commercial technologies [7]. The inclusion of nc-Si:H and the use of multi-junction cells improves this up to currently 13% [13], but this is still far below even modest quality c-Si devices, easily reaching 17%. The main cause for this deficiency is the low hole mobility of the material.

In order for charge to be collected in an PV device, the excited charge carriers (electrons and holes) must be separated, and transported to opposing terminals in the device. In a-Si:H PV devices, this is normally achieved by the use of a *p-i-n* junction; an intrinsic (undoped) bulk layer of amorphous silicon, often around 500 nm in thickness, with *p*- and *n*-doped layers on either side. The *n* and *p* regions of a-Si:H have very high dopant concentrations, with a low doping efficiency (percent of dopant atoms providing their respective charge carrier), causing the transport in these layers to be far inferior to the intrinsic bulk, and are thus made quite thin, usually 20-30 nm to avoid excessive recombination therein. The heavy doping of these layers also works to fully deplete the intrinsic region of the device, allowing one to approximate the field across the device to be linear, and thus provides a constant drift force to excited carriers in the intrinsic region.

In the simplest model, one can estimate the total length an average charge carrier can travel within the device before recombination, l_{drift}, as a product of the mobility of the carrier μ_c, the mean recombination time $\overline{\tau}_c$, and the field in the device $\vec{E}$:

$$l_{drift} = \mu_c \overline{\tau}_c \vec{E}. \tag{1.1}$$

Using this, we can estimate the probability P_c that a charge carrier will be able to transit an arbitrary distance, d_t before recombining as

$$P_c[d_t] = 1 - Exp(-\frac{l_{drift}}{d_t}). \tag{1.2}$$

For a device with an intrinsic layer thickness of d_i, we can estimate the collected charge (J) as an integral over this thickness of the generation rate, G multiplied by the probability of collection at said thickness, expressed as

$$J = \int_0^{d_i} G[x] P_c[x] dx \tag{1.3}$$

and with the power produced by the device simply defined as $W = JV$, where V is the produced voltage.

As a first-order approximation, ignoring the variation of the maximum power point on J and V, as well as the dependence of the voltage on the current (and thus again mobility), while also assuming that the field is independent of mobility and generation, we see that the cell power is related to the mobility of the device with a dependence of

$$P \sim Exp[-\mu_h]. \tag{1.4}$$

This indicates that at a fixed cell thickness, and low mobilities, as the mobility increases, the power will increase sharply as the cell transitions from having most carriers recombining before reaching the junction, to allowing more and more of the cell to be producing collectible current. As the mobility increases further, the benefits will diminish as the probability of collection from much of the cell approaches reasonable values, and the increasing mobility is only marginally reducing the recombination risk of the furthest carrier transport. While this basic model is useful for considering the general implications of mobility, to get a more quantitative view we need to examine a more complete model.

Ref. [14] provides a much more in depth (and accurate) view of the dependence of power on mobility. By first computing the voltage from the quasi-Fermi levels (from doping, generation and recombination estimates), charge density (from mobility and generation), and collection width (similar to l_{drift}, above), the maximum power-point voltage ($V = 2/3V_{OC}$) and current are combined to give the equation

$$P = ((2/3)V_{OC})^{3/2}(\mu_h \varepsilon \varepsilon_0 (qG)^3)^{1/4} \tag{1.5}$$

where q is the fundamental charge, ε, the material relative permittivity, and ε_0, the permittivity of free space.

From examination of Eq. 1.5, we can see that in this more complex model we observe similar qualitative behavior to that of our simple relationship in Eq. 1.4 – at low values of μ_h the power will increase quickly due to the $P = (\mu_h)^{1/4}$ dependency, and then will slow as μ_h approaches larger values. It is important to note that this

more complex model is examining the case of power saturation not solar efficiency optimization, and thus there is no limit on generation, making the application limited to low mobility values (the power becomes non-physical for single-sun illuminated photovoltaic devices when the efficiency nears, and consequently surpasses the theoretical limit).

We can examine this relationship quantitatively in this low mobility regime – plotted in Fig. 1-5 we show the dependence of the simulated power (P; top) as well as collection width (d_c; bottom) on hole mobility, on log-log scales.

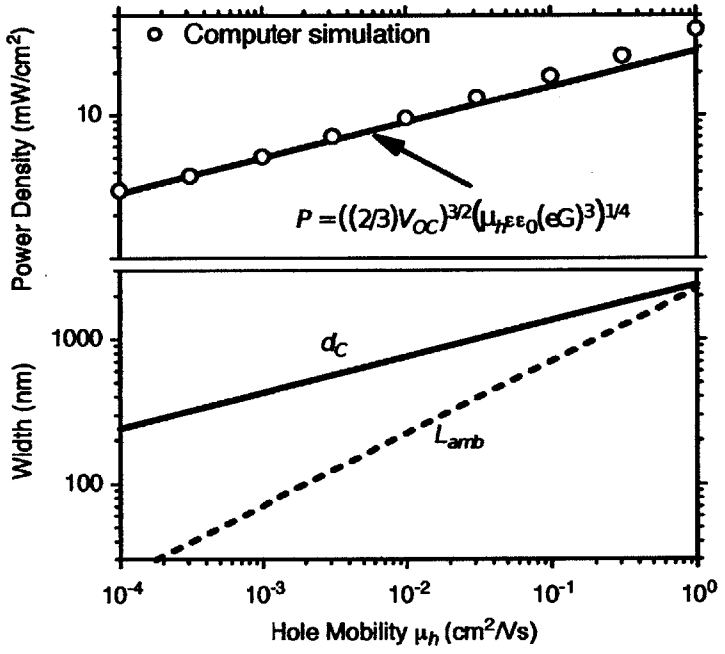

Figure 1-5: **Top**: Simulated power density of a-Si:H model devices as a function of mobility, both analytically in the form of Eq. 1.5 (line), as well as full device simulations (dots). **Bottom**: Dependence of depletion collection region in the devices simulated above, as well as the ambipolar diffusion length (L_{abm}), also as a function of hole mobility. Reproduced from Ref. [14].

Also shown is the ambipolar diffusion length (L_{abm}), which is the length of carrier travel in the absence of a gradient in electric potential. This term is neglected from the analytical examination (solid line, top) but included in the full device simulations to which the model is compared (top, circles). It can bee seen that the diffusion lengths

are quite small in this model, and thus only begin influencing the simulation (seen as deviation of the circles from the line) at mobilities in excess of $\sim 10^{-1}$ cm^2/Vs, again supporting the assumption that drift current in the large depletion region is dominating the transport in these devices. It can be seen that a factor of 10 increase in mobility, say from 10^{-3} to 10^{-2} cm^2/Vs, moves the simulated efficiency from ~5% to ~9%, giving a $10^{1/4} \approx 1.77\times$ efficiency improvement. This makes clear why the optimization of hole mobility is essential to maximizing the efficiency of amorphous silicon photovoltaic devices.

The work composing this thesis focuses largely on the origins of this low mobility, both computationally and experimentally, as well as a possible route of improvising the hole collection in a-Si:H devices.

Chapter 2

Origins of Structural Hole Traps in Hydrogenated Amorphous Silicon

2.1 Introduction

2.1.1 Motivation

Over the last four decades, much work has been done toward understanding both the origins of the low efficiency of hydrogenated amorphous silicon (a-Si:H) solar cells, and how the properties limiting efficiency can be improved. Two main factors have been attributed to this low overall efficiency – the Staebler-Wronski effect (SWE) [15], (a performance degradation under exposure to light; normally around a 10% current drop in optimized cells [16]), and the inherent low hole mobility in the material (typically around 5 orders of magnitude lower than crystalline silicon) [17, 16], although the causes of both of these properties are still not fully understood. This uncertainty is rooted in the inherently disordered nature of amorphous materials, which severely complicates theoretical analysis. For our purposes here, we focus on the defects contributing to the initial low mobility, although there is substantial evidence that by improving this property, the degradation from the SWE can be curtailed as well [18, 19, 20].

2.1.2 Previous Work

Extended discussions concerning the nature of the defects limiting the hole mobility of the material have appeared in the literature over the past decades. Early works asserted that the major defect was the dangling bond (3-fold, under-coordinated Si atoms), controlling both the deep, mid-gap states directly [21, 22, 23], as well as the shallower band-tail states (often through secondary mechanisms, e.g. conversion between dangling and weak bonds) [24, 25, 26, 27, 23]. Floating bonds (5-fold over-coordinated Si atoms; Fig. 2-2a) were also implicated [28, 29, 30, 31, 32], although this alternate theory never seemed to gain much traction. The reliance on mid-gap states controlling the initial mobility have since declined, with both computational and experimental works providing evidence that the band-tails control the mobility of holes, and that these states are expressed independent of mid-gap state concentrations [33, 34]. This culminated in Ref. [14], showing the efficiency of an a-Si:H cell is controlled not simply by the mobility, but the mobility as determined by the extended valence band-tail states. We reproduce this relationship in Fig. 2-1, depicting the saturated power density under constant volumetric excitation for a *p-i-n* device, with a dramatic increase in power generation as the valence band-tail width is reduced. The estimated valence band-tail width from experimental measurements for a-Si:H is indicated on the plot as 45-50 meV, placing the material at the far limit of disrupted transport, although other sources predict even higher values [35].

This rethinking of the source of poor efficiency being due to these extended band-tails has been accompanied by an evolution of alternate theories on the sources of the states composing them, indicting other structural phenomena, such as strained bonds or filaments [36, 37, 38, 39], movement of hydrogen [40, 41, 42, 43], and incorporation of mono- and di-vacancies in the material nanostructure [44], as correlated to the trapping of holes in the material. Despite this plethora of investigations, there has been little consensus as to the nature of the band-tail traps, which, we believe, is exacerbated by a lack of studies on statistics of causal relationships between atomic structure and hole trapping.

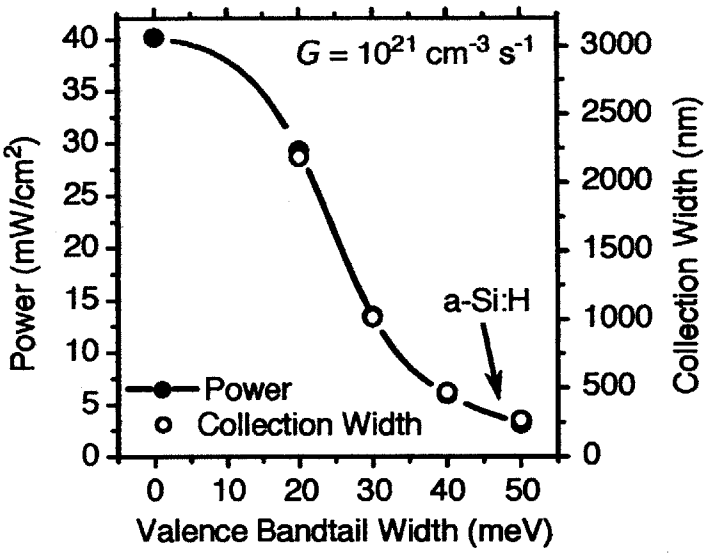

Figure 2-1: Saturated power density of a simulated p-i-n amorphous silicon solar cell, under constant volumetric excitation. Adapted from Ref. [14].

2.1.3 Outline

In this chapter, we address this uncertainty through three main contributions: first, we create and validate a large ensemble of *ab-initio* hydrogenated amorphous silicon structures, providing what we believe is an accurate computational model of the bulk material. Second, through the application of statistics to density-functional theory-determined properties of our ensemble, we explore the relative contributions of wide-ranging structural defects to hole trapping distributions, allowing us to concomitantly clarify the prevalence and severity of these defects in our ensemble. Finally, using this data, we are able to provide insight into a possible trap state in which reversible silicon atom displacements allow holes to self-trap in highly stable (deep trap) configurations (Fig. 2-2b), with a stronger correlation to substantial trap states than any other examined defect.

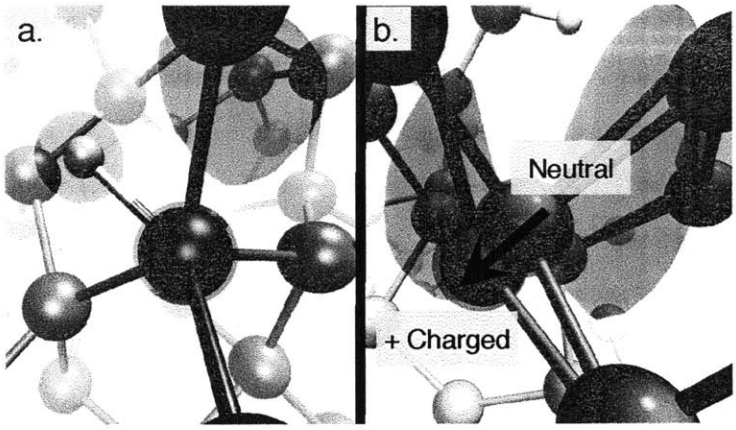

Figure 2-2: Hole 50% probability location density (red) for: **a.** floating bond defect, and **b.** reversible atomic displacement causing hole self-trapping. The central defect atoms are in blue, and show hole wave function localization near said defects.

2.2 Methods

2.2.1 Ensemble Modeling

Computer modeling of amorphous materials has two conflicting needs: on the one hand, accurate treatment of electrons is required, and on the other, to accurately reproduce the bulk disordered system, large samples of atomic configuration space are necessary. Calculating a large set of geometries and taking the ensemble as a whole for the purpose of analysis allows us to approximate the diversity of configurations present in a bulk layer, while balancing between the prohibitive computational expense of inordinately large structures, and the inaccuracies of few, small geometries. To this end, our work is performed on a set of 2700 virtual samples (split into 1200 sample training and 1500 sample test subsets) of 216 Si and 20 H atoms (as shown in Fig. 2-3), with the size chosen to minimize computational expense, while reducing finite size errors due to the (charged) periodic system and the amorphous network. An approximate 10% hydrogen atomic concentration was chosen to fit with the nominal concentration set in experimental materials optimized for PV performance [45].

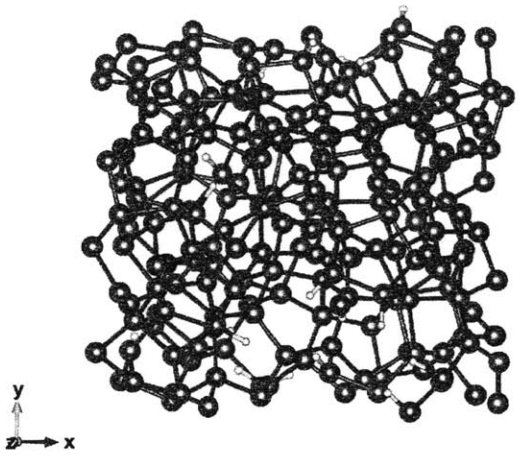

Figure 2-3: Example simulated a-Si:H structure, containing 216 Si (gray) and 20 H (white) atoms in a period cell.

2.2.2 Sample Creation

Our structures are initially produced by randomizing a crystalline silicon network in the method described by Wooten-Winer-Weaire (WWW) [46], using a Keating [47] potential to determine the energy of the bond changes. Hydrogen is added at the beginning of the simulated annealing, substituting two hydrogen atoms for one randomly selected bond in the then-still crystalline lattice, to maintain full bond coordination. The amorphization is performed congruently with the WWW process (with the hydrogen simply treated as an unbonded silicon atom, although naturally with a different potential), resulting in a local minimum energy structure. The geometry is then relaxed using the density-functional theory (DFT) package SIESTA [48], using a variable unit cell, the PBE approximation [49] with a DZP basis, and sampling at the gamma point. To validate the use of a single k-point, a selection of characteristic samples were examined with a 2x2x2 k-point grid and the energies of the structures did not change to any measurable extent (less than 0.05 eV in the total energy). The input files used for the DFT calculations are included in Appendix B.

2.2.3 Hole Trap Depth Measurement

Previous studies have mostly examined the energy level of the highest occupied molecular orbital (HOMO) as a metric for the hole trap depth of a structure. While this approach does indeed give the positive-charge ionization energy of the initial geometry, it also presents potential problems: first, the accuracy of this energy level for reasonable time scales cannot be assured, as substantial atomic relaxation could occur during the presence of the hole in the localized area, especially in regions with already relatively low ionization energy. Furthermore, beyond the introduction of uncertainty into the distribution of ionization potentials, simply using the HOMO level to infer the hole trap depth ignores the possibility of self-trapped holes.

For these reasons, the a-Si:H geometries in our ensemble are re-run from the neutral configuration with one electron removed (a net +1 eV charge applied), and again allowed to fully relax within density-functional theory (DFT). This provides us with the positive charge energy of the sample (E_+). We use this in combination with the neutral charge configuration energy (E_0) to compute the adiabatic ionization potential, $I_n = E_0 - E_+$, of the structure - a measure of how energetically expensive it is for a hole to be present in a given structure in our virtual bulk amorphous silicon material.

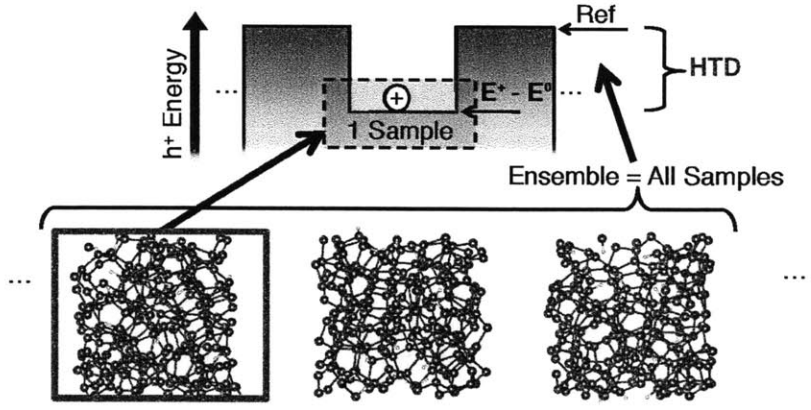

Figure 2-4: Diagram depicting the calculation of hole trap depths as the ionization potential of a sample relative to the ensemble.

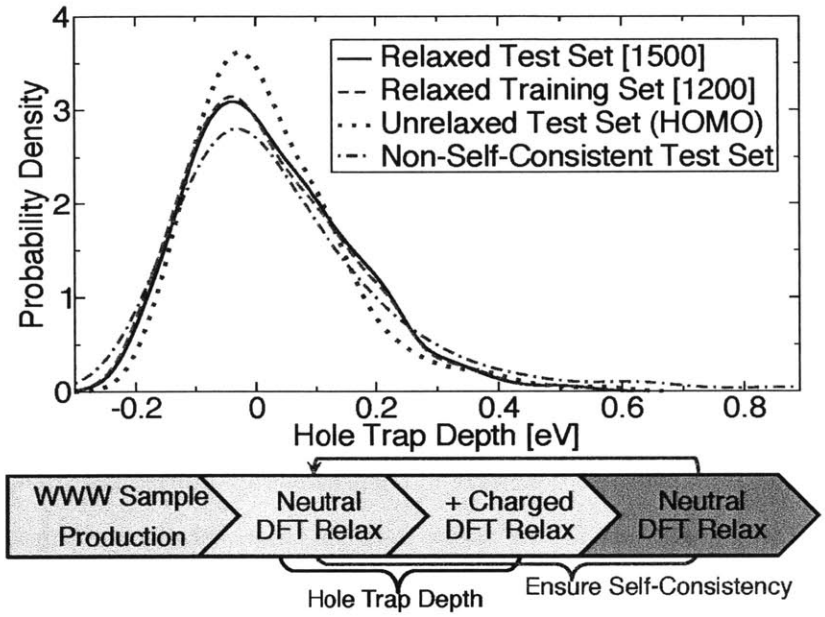

Figure 2-5: Comparison of the test set (used to verify and display trends) to the training set (used to determine trends), as well as to the test set before the positive charge relaxation (misses many trap structures; appears overly-ideal), and the test set before the application of the self-consistency requirement (includes some absolute relaxations; includes unphysical hole traps). The flow diagram below depicts the sample creation process.

Once the ionization potential has been determined for all 2700 samples, we select a reference energy, I_0, from which to base the calculation of each samples' hole trap depth $HTD_n = I_n - I_0$, as depicted in Fig. 2-4. It is necessary to take the hole trap depth as a relative quantity, as it is the energy change between any given sample and the set as a whole that determines the difficulty of a hole moving from one location in a material to the next. We select the mode ionization potential as the reference energy of our ensemble so that the movements within the bulk of the distribution will correspond to a hole trap depth of ~0 eV. The comparison of the fully relaxed ensemble to that of simply using the unrelaxed energy (or HOMO energy level of the neutral sample) is illustrated in Fig. 2-5.

Our full ensemble of 2700 structures was initially split into a 1200 sample training set, which was exclusively used to determine all correlations and trends, and an uncorrelated 1500 sample set, used to verify the trends and conclusions drawn from the former [Fig. 2-5]. This separation of the training and test sets allows us to independently search for (in the training set), and confirm and present (in the test set) correlations between our structures and their hole trap depths, thereby precluding any chance of over-constraining our analysis to the specifics of the samples that we are examining. All plots in this work (unless otherwise noted) are shown using the 1500 sample set to strictly prevent sample bias in our results.

To ensure self-consistency in this method, the sample geometries must be fully reversible between the uncharged and charged states, as an irreversible relaxation caused by the removal of an electron would be expressed as a large energy difference, but would not indicate a case of strong hole trapping. This reversibility is verified through re-neutralizing the charged geometry, allowing it to relax fully again, and comparing this third structure with that of the original neutral sample. In the fairly rare cases in which changes are present, the re-neutralized sample is then set as the base configuration, and the process repeated until the neutral energies converge. All samples were found reversible between the neutral and charged states after at most two of the above-described steps. It is interesting to note that the process of hole addition causing a favorable relaxation could actually be capturing some real physical

occurrence (as electric biasing of a-Si:H does show cell efficiency improvements and works to reverse some SWE degradation [50]; and the introduction of an electron to a hole trap location has been previously offered as an explanation for the SWE [17]), but for the scope of this study the phenomena was simply used as a limit on the phase-space of our set to ensure self-consistent hole trap depth measurements. The flow of this process, as well a comparison to the non-self-consistent ensemble, is also depicted in Fig. 2-5.

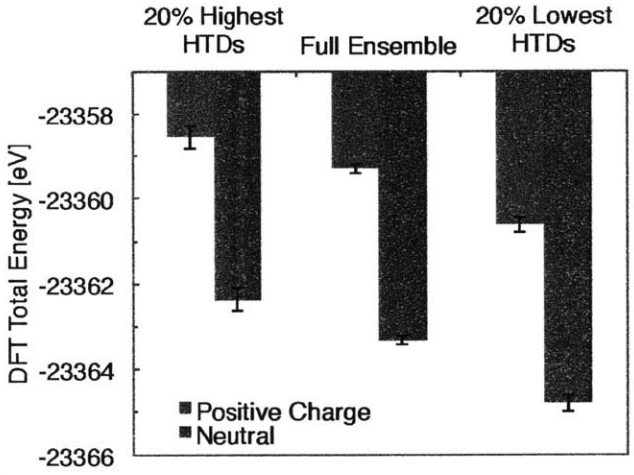

Figure 2-6: Correlation between structural hole trap depth and total energy, showing the samples with the highest hole trap depths have a statistically higher energy than the full ensemble average and the lowest hole trap depth samples. Error bars represent 95% confidence intervals.

Finally, we note that there is a correlation between the total energy of our relaxed structures, both in the positive and neutral charge states and the hole trap depths of the structure. As shown in Fig. 2-6, we see a slight correlation between the structural energy of both positive and neutral charge samples and the hole trap depth of the highest and lowest 20% of the distribution. This is likely due to samples with higher levels of electronically-measurable disorder having a slightly higher probability of containing strong hole trapping features. In the coming sections we explore the specific forms of disorder responsible for these correlations with increased hole trapping.

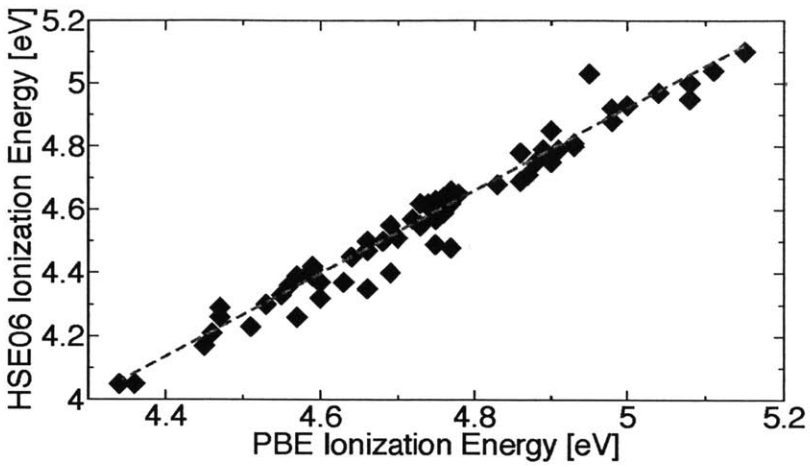

Figure 2-7: Compairson of PBE- and HSE06-calculated ionization energies, with a linear regression shown in the red dashed line.

Measurement Validation

We will begin by analyzing the potential for error in our structure creation method – in order to confirm the accuracy in the comparison between our charged and uncharged structural energies, we re-calculated 60 of the final structure energies (in both the charged and uncharged states) using the HSE06 hybrid functional implemented in the Vienna Ab initio simulation package (VASP). The 60 structures were selected at random, but verified to represent the full range of observed hole trap depth values (specifically expressing trap depths from -0.20 to 0.37 eV). We found a very strong correlation between the PBE-calculated energy difference to the HSE06-calculated energy difference, as shown in Fig. 2-7, with a RMS deviation (root-mean-square of the residuals) of 0.04 eV in the PBE energies.

Somewhat interestingly, the correlation with the HSE06 energies did provide an energy ratio of approximately 1.3, indicating that the energies predicted by PBE-DFT are somewhat below those calculated by the hybrid functionals. This is likely due to band gap underestimation, and would simply result in a linear scaling of the abscissa of our plots involving the hole trap depths of our samples, if desired. While this could indicate a shift in the quantitative values predicted for our hole traps, it does not

change our qualitative results (the relative strength and proportion of different defect states) which our conclusions rely on. We have chosen to leave our results in terms of the PBE energies, for ease of verification using the supplied structures and input files. The structures used for this validation have been set as the first 60 structures in the supplied database.

We also note that due our analysis resting on relative energies we preclude any errors resultant from charge being introduced into a periodic system, as such corrections are simply based on the periodic cell geometry, and thus would cancel upon the subtraction of our ionization potentials from our reference (median) level [51]. Furthermore, the requisitely large size of our supercells (216 Si atoms) prevents significant errors in our trap depth energies resulting from offsets in the potential alignment [51], and has been verified to be large enough prevent self-hybridization of the hole wavefunction across multiple periodic cells.

2.2.4 Structure Validation

In order for any conclusions drawn from our ensemble of a-Si:H geometries to have physical meaning, we must first confirm a reasonable level of verisimilitude between our virtual samples and experimental measurements of tangible films. Several properties were matched to empirical properties of a-Si:H by design - we selected and fixed the hydrogen content of our samples at around 10% (20 H atoms per 216 Si atoms), as this is reported to be common "high-quality" or "device quality" films [45].

Furthermore, while the material can express a wide range of intrinsic stresses [10], we fix our samples in their mechanical ground state, targeting an overall neutral stress condition. It is important to note that this does not preclude the incorporation of bond strain into our structures, but simply mandates the total strain on the full structure be (very nearly) neutral.

In addition to a variety of stresses, a-Si:H also exhibits a vast array of microstructural phenomena, such as nanovoids, hydrogen clusters, and both under- and over-coordination defects. While we expressly did not introduce any of these aspects into

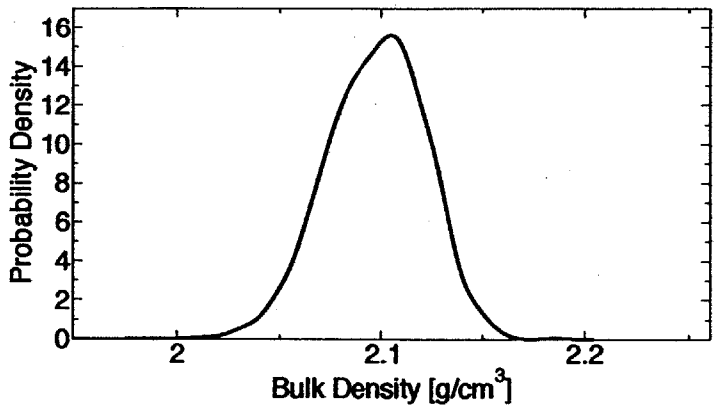

Figure 2-8: Distribution function of sample densities in the ensemble created for this work. This is compared to experimental values in the text.

our ensemble manually, we did observe that they were naturally incorporated into some of our structures by virtue of our sample creation technique.

We have qualitatively verified similarity between various structural parameters, such as bulk density: as seen in Fig. 2-8, we observe an average density of our samples of about 2.09 g/cm^3. Experimental densities in a-Si:H have been observed in a wide range (from 1.47 to 2.30 g/cm^3), with values of ~2 to 2.25 g/cm^3 apparently normal for films of our hydrogen content (~10%) [52], fitting well with our average value of 2.09 g/cm^3.

Next, we examine the radial pair distribution function [Fig. 2-9], a measurement of the local order in our samples. Comparing to two different experimental measurements, of pure amorphous silicon, line A from Ref. [53], and hydrogenated amorphous silicon (with a fairly high hydrogen content of ~21%, likely increasing disorder and accounting for why the first peak appears quite lower than the other samples), line B from Ref. [54], we again see quite nice correlation between our film and the experimental measurements, indicating a strong agreement between the local order in our geometry ensemble and physical samples.

The ensemble's average bulk modulus (determined by targeting a compressive stress in the DFT "relaxation," and measuring the observed change in the structure volume) also compares quite well to experimental values: we observe a bulk modulus of

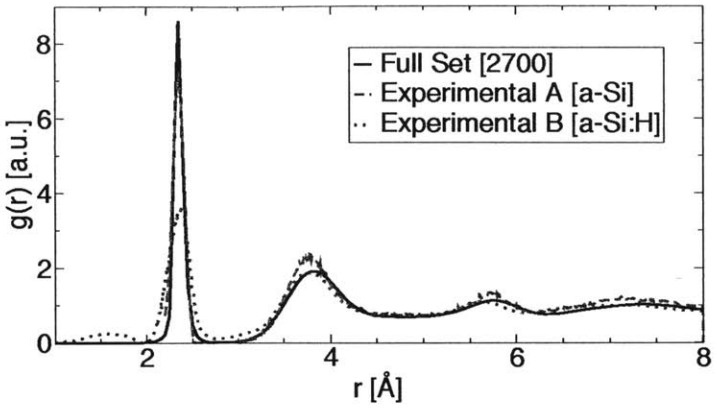

Figure 2-9: Radial distribution function (g[r]) of both the structures in the ensemble created for this work and two experimental works: A - Experimental data from [53]; B - Experimental data from [54]

approximately 65(1) GPa, whereas physical films have been measured at 66 GPa [45]. the total energy of the amorphous silicon structures over the corresponding crystal geometries.

Finally, for electronic and energetic correlations, we confirmed (as recently recommended by Drabold [36]) that the additional total energy of the structures produced for this study above the corresponding crystalline geometry match results obtained via recent differential scanning calorimetry experiments [55, 56] remarkably well (0.07-0.15 eV/atom experimental; 0.07-0.17 eV/atom in our calculations).

2.2.5 Ensemble Analysis

Having established and vetted a computational set of a-Si:H structures, we are able to explore causation between geometric features and hole trapping as follows: by calculating a hole trap depth distribution of our full ensemble (using kernel density estimation [57, 58]), we can compare this to conditional distributions with samples expressing certain features removed. If the conditional distribution does not contain hole trap states, then we can say that either the removed defect causes hole trap states, or there is a common cause between it and the trap states.

While the potential selections for these conditions are enormous, and many tested (average/extrema bond lengths and angles, density, etc.) criteria showed no statistically relevant relationships, we present three here that we believe demonstrate interesting characteristics of our set. For "improvement," we are most strongly considering a decrease in the positive hole trap depths, although narrowing of the distribution in general is beneficial, with the limiting case (a perfect crystal) being a Dirac distribution. It is also important to note that the number of samples present in the conditional set determines the resolution of the distribution, and so for each conditional ensemble we list the number of samples meeting the applied criteria in brackets after the sample label in the legend of the plot.

2.3 Results

2.3.1 Coordination Defects

We begin by investigating the oft-asserted culprits behind the deepest hole traps: dangling, and floating bonds. In order to define dangling, and floating bonds, we inspect the local environment of each silicon atom in each structure, noting the 4th- and 5th-closest atomic distances: a short 5th-closest distance indicates a floating bond, while a long 4th-closest distance indicates a dangling bond. Through the examination of the probability distribution of over-coordinated Si atoms (short 5th-closest distance in a structure) and under-coordinated Si atoms in Fig. 2-10a, are able to define what we consider bonding: we take the minimum of the 5th bond distribution at 2.75 Å as the cutoff criterion. Analyzing this distribution and its role on the hole traps in our ensemble, we observe several interesting phenomena. First, the prevalence of floating bonds exceeds those of dangling bonds in our ensemble, supporting the views of Pantelides [30], that floating bonds are the more-abundant coordination defect in a-Si:H. Second, we see that the floating bond is substantially more defined, although both defects are indeed continuously present from distances of $\sim$2.5 to 3.2 Å. Examining the conditional probability distribution of the ensemble [Fig. 2-10b],

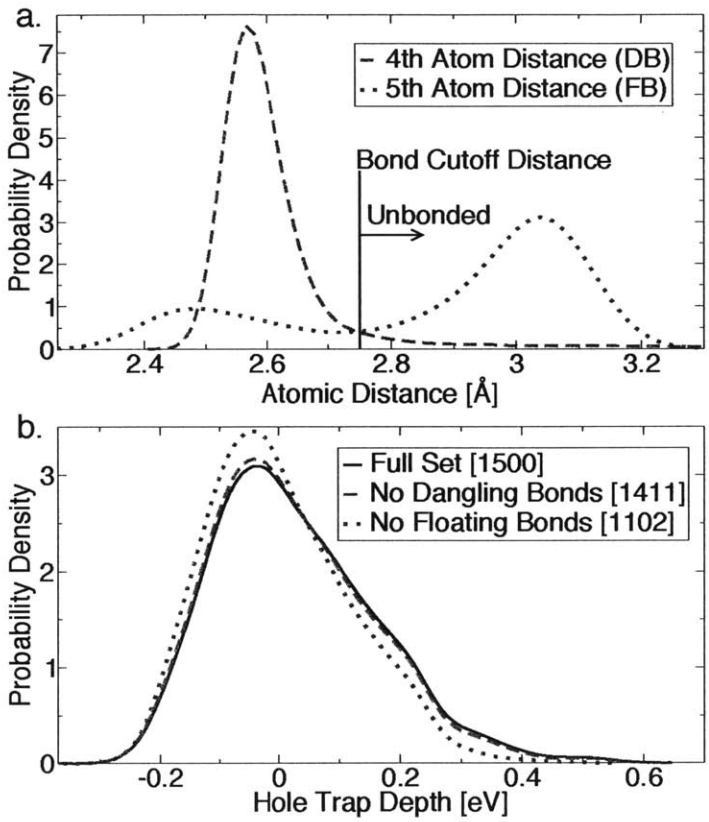

Figure 2-10: **a.** Distributions of the longest 4th and shortest 5th atomic distances prevalent in each sample (see text for clarification) **b.** Hole trap depth distributions displaying relative strength of dangling bond and floating bond coordination defects.

we observe that the removal of floating bond-containing samples idealizes the distribution substantially more than the removal of dangling bond-containing samples. This indicates that floating bonds are not only more prevalent in our ensemble, but correlate more strongly to hole traps as well. Finally, we notice that while the removal of all floating and dangling bond samples from our ensemble does improve the distribution (most notably around +0.2 eV), there still remains a substantial density of hole trap structures that are unexplained by these coordination defects.

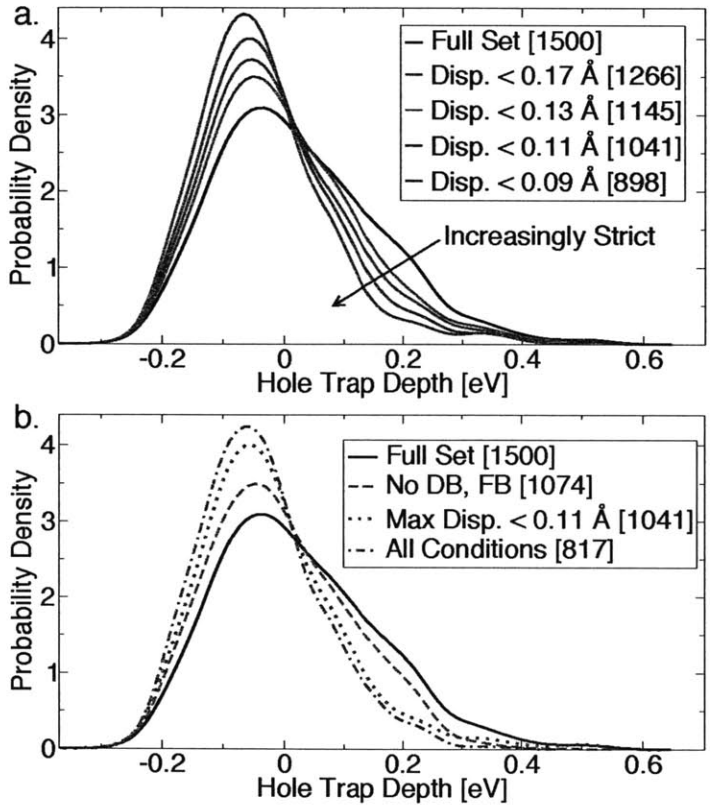

Figure 2-11: Hole trap depth distributions **a.** displaying the effect of an increasingly strict "maximum displacement" criterion continually excluding reversible displacement defects, and **b.** compared to coordination defects, and the congregation of all listed defect.

2.3.2 Ionization Displacement

To understand these remaining hole traps, we next examine the maximum silicon atom displacement in our samples under hole introduction (referred to from here as "displacement" for succinctness). As seen in Fig. 2-2b, substantial displacement can occur during charge introduction into a sample. This is important for three reasons: first, the hole preferentially localizes near the displacing atom, indicating that the displacement is allowing the hole to self-trap in the reconfigured structure. Second, the displacement is entirely reversible - by limiting our sample phase-space to structures with repeatable hole trap depths under relaxation we ensure (and have manually verified) that the displacement observed is indeed a metastable defect promoting hole self-trapping and not simply a lowering of the total energy of the system. Finally, the displacement is accompanied by substantial hole trap depths: as seen in Fig. 2-11a, by applying an increasingly strict "maximum allowed displacement" criterion to the conditional probability distributions of hole traps in our ensemble, we observe increasingly idealized distributions, indicating that the prevalence of reversible atomic displacement is strongly correlated with hole trap depth. Furthermore, comparing the conditional distribution excluding structures featuring high displacements to that in which we exclude coordination defects [Fig. 2-11b], we observe that the influence of self-trapped holes linked to atomic movement outweighs even those of the dangling and floating bonds combined. The confluence of all these conditions together, however, improves the distribution even further, indicating that these features are indeed distinct, and complementary in their influence on hole trapping.

Statistical Significance

All trends mentioned above are confirmed using a Kolmogorov-Smirnov test to be statistically relevant. This test determines the probability that the conditional probability distribution presented is representative of a true distribution unique from their parent distribution. In other words, it gives a metric for the probability that the hole trap distribution is being significantly modified by the conditions applied. Tests were

performed using kernel widths from both the normal distribution approximation, and with an increased width on the order of the error determined by the comparison between the PBE and HSE06 functionals (a standard deviation of 0.04 eV). The conditional distribution featuring the removal of dangling bonds yields a rejection probability (a probability that the distribution is unchanged by the application of the condition) of 17.7%, too high to be considered statistically relevant. This is expected as the removal of dangling bonds has little influence on our distribution, as seen in Fig. 2 of the main text. The "no floating bonds" condition, however, gives a rejection probability of 4.67x10-10, and the "no displacements greater than 0.13 Å" condition yields a rejection probability of 1.48x10-11, both overwhelmingly small enough to be considered statistically significant, further supporting our assertion that PBE calculations are of sufficient accuracy for our study.

Further Analysis of Ionization Displacement

In Fig. 2-12, we examine solely the highly displaced (under ionization) atoms in our ensemble, measuring how said displacement changes the ideality (i.e., proximity to the "perfect" crystal structure [4-fold coordination, 109° bond angles, etc.]) of this selection of atoms, with positive values indicating motion toward ideal structures and negative, away. While these displacements exhibited no uniform transition toward or away from ideal structures (nominal bond lengths, angles or coordination), we did observe a slight average movement away from the ideals, which in the case of in bond lengths and (to a lesser degree) average coordination was in fact statically relevant (signal was present within the standard error of the correlation), possibly indicating that the hole is pushing the system into what would often be a less favorable energy state in the neutral charge configuration, but the relaxation of the hole over this area provides enough of a energetic benefit to offset the less favorable geometry.

We should note that none of these structural "problems" alone (when looked at over an entire sample, as opposed to only displaced atoms) yielded any correlation with hole trapping, however. For example, while there is a statistically relevant trend of the bond lengths of the ionization-displaced atoms moving away from the ideal crystal

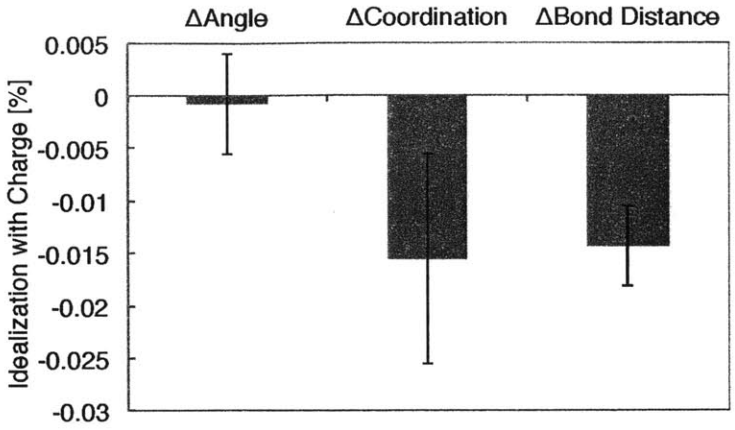

Figure 2-12: Average movement toward the ideal structure (c-Si configuration) of ionization-displaced atoms measured by metrics of bond angles, average coordination, and bonding distances. The error bars represent the 95% confidence intervals the trends.

length (and, as shown before, a correlation between ionization-displaced atoms and deep hole traps), we observed no statistically relevant trend between bond lengths in the full sample and the strength of hole trapping.

2.3.3 Hole Localization

Lastly, we examine the correlation between the hole trap depth of the structure and the localization length of the hole wave function in the charged state. The localization length is computed via the method presented by Resta and Sorella [59], and Silvestrelli [60]. As seen in Fig. 2-13, we observe a strong bias toward negative trap depths (hole barriers) in the samples with the shortest hole localization lengths, whereas the structures with highly delocalized holes (long lengths) express higher trap depths. While the correlation is quite strong in the short localization length regime, as the length increases the correlation to stronger traps appears to increase, peak, and then reduce, suggesting a balance between two opposing forces: structural phenomena energetically favoring the hole to localize nearby, balanced against the kinetic energy driving the hole to delocalize. This lends credence to the ionization displacement effect, in that it motivates the view that the displacements are occur-

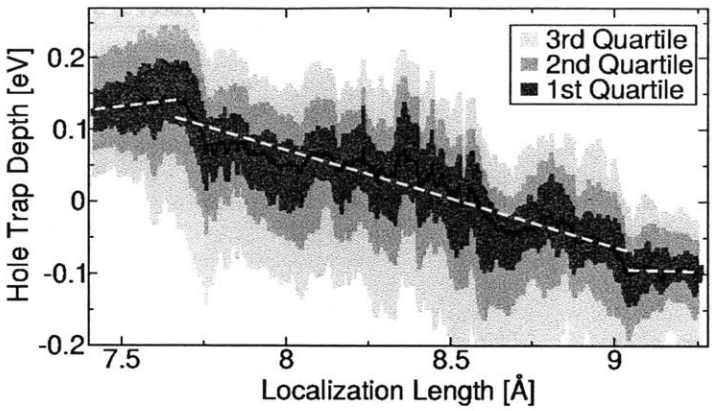

Figure 2-13: Correlation showing peak hole trap depth at an intermediate hole wave function localization length. The grey solid areas represent quartiles in the trap depth probability distributions, with the black line indicating the center of the distribution, and the dashed white line a piecewise linear regression to the data.

ring to allow a relative delocalization of the hole in its confined state to mitigate this "over-confinement" energy penalty.

2.4 Conclusions

The major contributions of this work can be summarized as, first, the demonstration that ionization-induced atomic displacement expresses the strongest causal relationship to hole trapping of any of the investigated structural features. This bolsters the view that a-Si:H is indeed a fluctuating material, in contrast to the static geometry of its crystalline counterpart. Second, we provide evidence for the exoneration of dangling bonds as the major coordination defect in the material, and instead implicate floating bonds as the more significant contribution to limiting hole mobility. Finally, we provide further evidence as to the importance of moderate delocalization of the hole wave function in producing deep trap states. While these results do challenge some previous theories, many of the more recent contributions are in no way mutually exclusive, and some well-supported by these findings - for example, the recent work by Drabold [55, 38], correlating the presence of the tail electron states proximate to

static bond-distorted "filaments," fits well with our observations that the highest trap states are correlated with higher levels of delocalization.

The results presented here provide insight into potential methods of preventing these traps, and thereby improving the material electronic transport properties. For example, recent advances in the understanding of stress [61, 62, 10] could be used in leveraging strain in samples to prevent atomic displacements, as could attempts at targeted annealing to crystallize or re-amorphize regions under which metastable displacement defects are present.

While these correlations advance the understanding of the nature of structural hole trapping defects in hydrogenated amorphous silicon, we believe that far more knowledge can be gleaned from the created ensemble of geometries. To this end, the entire set of 2700 a-Si:H structures has been made freely available online (available: http://journals.aps.org/prl/supplemental/10.1103/PhysRevLett.110.146805/a-Si_Structures.zip), with the hope that a readily available large ensemble of amorphous silicon geometries will foster further discoveries based on statistical analysis of the set, and eliminate any future need to rely on anecdotal analysis of single structures.

Finally, we hope that beyond the specific system of a-Si:H, both the statistical methods utilized here, as well as the results supporting the importance of self-trapping defects could prove useful in the study of any disordered systems concerned with band-tail states (for example, disordered organics and polymers).

Chapter 3

Experimental Measurement of Hole Mobility

3.1 Introduction

3.1.1 Motivation

While computational studies into the atomic structures correlating to hole trap depths (as explored in Chapter 2) yield many insights into potential causes of the low mobility in a-Si:H, in order to determine the validity of these explanations, it is important to provide experimental evidence supporting our conclusions.

3.1.2 Previous Work

Multiple studies have provided excellent frameworks for measuring hole mobilities experimentally in hydrogenated amorphous silicon [63, 64, 65], and while there exist works analyzing the influence of deposition parameters on hole mobility [66, 67], there have been none to our knowledge which have explored the influence of both material stress and hydrogen content (both seen to vary widely as film deposition conditions are modified [10]) on hole mobility in a-Si:H. In order to determine the origins of the low hole mobility in a-Si:H it is essential that we first understand how the material properties are influencing this parameter. This is crucial as hydrogenated amorphous

silicon does not simply refer to a single ideal material, as in crystalline systems, but rather a spectrum of bonding configurations, densities, stresses, and hydrogen contents, all of which influence the external parameters of the material, undoubtedly including the transport of charge carriers.

3.1.3 Outline

In this chapter we work to establish a basic relationship between material properties, and hole mobility. First, we discuss the theory behind, and setup of a time-of-flight transient photocurrent measurement apparatus, used to measure hole mobilities. Next, through experimental measurements of a-Si:H hole mobility over a wide range of deposition conditions, we correlate the mobility with independent measurements of film intrinsic stress, and hydrogen concentration and bonding configuration. Finally, we show that the peak mobility values occur at moderately compressive values of stress, away from the extrema of either hydrogen bonding concentration.

3.2 Theory of Time-of-Flight Measurements

The essential idea behind time-of-flight transient photocurrent (ToF) measurements lies in the recording of the movement of mirror charges compensating a sheet of the interrogated carrier as it drifts through the material under an applied electric field. This is normally achieved by photoexciting a large number of carriers at the front side of a device, with a doped layer present at that front surface designed to quickly extract all of the charge carriers that are not being examined (*e.g.* if holes are being monitored, then an *n*-type material is used to immediately extract electrons). A bias is applied across the device from slightly before the excitation to until all charge carriers are recollected at the back of the device, providing an external drift force to drive the carriers to the rear contact. The current through an external circuit connecting the two ends of the devices is monitored. This current arises from charge accumulating on the rear contact of the device as the sheet of carriers moves through

the device, approaching this back contact. The ToF measurement mechanism is depicted in Fig. 3-1.

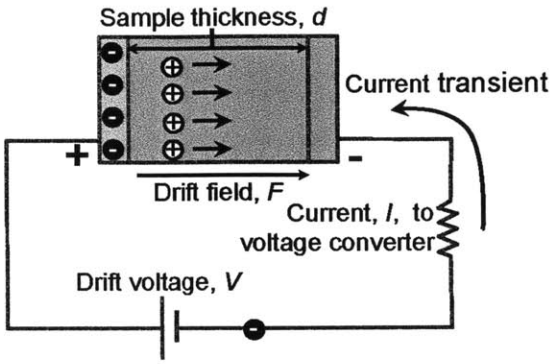

Figure 3-1: Schematic depiction of the time-of-flight measurement mechanism for hole transport measurement in a *n-i-p* configured device. Adapted from figure by C.B. Simmons.

3.2.1 Ideal Transport

The movement of the charge through the measured material of thickness d induces a collection of mirror charge, Q_m on the back contact, as a function of the charge sheet (n carriers of fundamental charge q) position in the bulk from the back contact, x

$$Q_m[x] = \frac{nqx}{d} \tag{3.1}$$

This requires a current, I_m to flow through the external circuit to supply this charge

$$I_m = \frac{\partial Q_m}{\partial t} \tag{3.2}$$

and combining equations 3.2 and 3.1, while assuming a linear field, and thus a constant carrier velocity we see the current is defined by

$$I_m = \frac{nq\mu_{drift}F}{d}, \tag{3.3}$$

where F is the applied electric field to the device, and μ_{drift} is the drift mobility of the measured carrier, simply defined as $dx/dt/F$, or the velocity of carriers with respect to the electric field present.

We can then determine that the sheet of carriers reaches the back contact (*i.e.* transits the device thickness, d) after a transit time

$$\tau_{drift} = \frac{d}{\mu_{drift} F}. \tag{3.4}$$

Knowing that the field is determined by the applied voltage, V, with the form

$$F = \frac{V}{d}, \tag{3.5}$$

and through the measurement of the transit time evidenced by the lack of need for further mirror charge eliminating the current flow through the external circuit, allows the computation of the drift mobility of the tested species as

$$\mu_{drift} = \frac{d^2}{\tau_{drift} V}. \tag{3.6}$$

Equation 3.6 makes it clear that accurate determination of both the drift time, as well as the thickness of the sample are essential to accurate measurements of the mobility. To address the former, and to make the measurement more robust to systematic errors in the measurement of the applied voltage (losses in application of the bias) and transit time (delays from the measurement system), the measurement is repeated at several different applied voltages, and the mobility is calculated from the slope of the linear regression of the product of the cell thickness and field as a function of the drift time, or

$$\mu_{drift} = \frac{\Delta d^2/V}{\Delta \tau_{drift}}. \tag{3.7}$$

To address the latter (measurement of d) we cleave all samples and take cross-sectional measurements to accurately determine the device thickness (see Fig. 3-5).

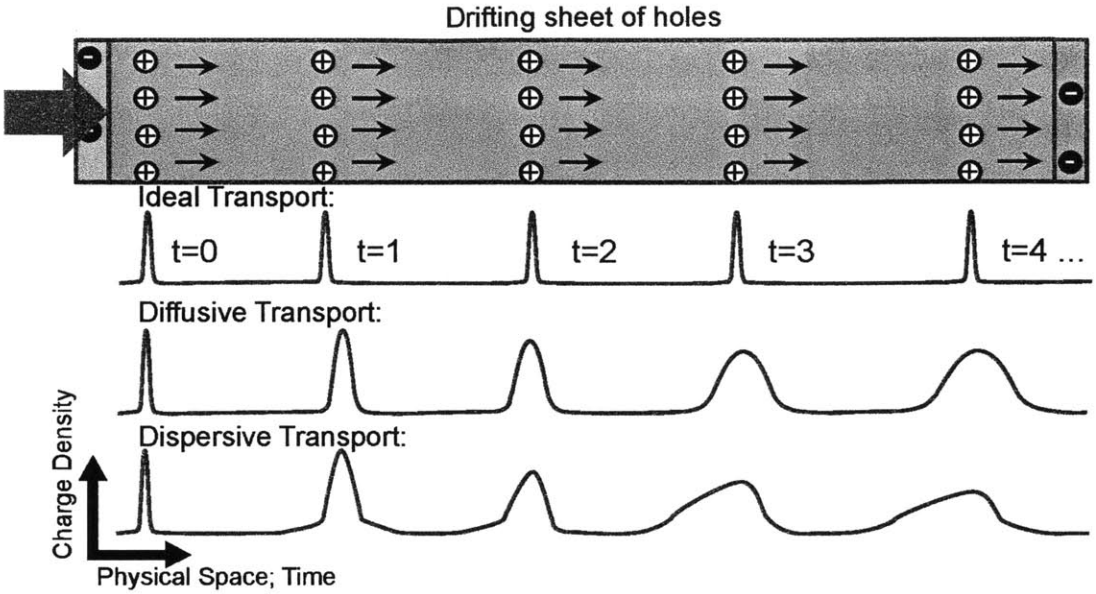

Figure 3-2: Diagram showing ideal, diffusive, and dispersive transport variations on the charge density moving through the material. Ideal transport indicates a single sheet of holes; diffusive shows a Gaussian relaxation of the sheet; and dispersive shows an asymmetric profile as carriers are trapped and released into band-tail states.

3.2.2 Non-Ideal Transport

So far, this description of the measurement of the time of flight mobility has assumed both non-diffusive transport (*i.e.* that the carriers remain a solid sheet of charge as they move through the material), as well as non-dispersive transport (*i.e.* that the carrier profile remains symmetric, and is not subject to the trapping, filling and release of defect states as it transits the material). A comparison of the influences of these deviations from the ideal measurement are depicted in Fig. 3-2. While all physical materials will show some slight character of the two non-ideal transport mechanisms, the level to which they are present are determined by the dielectric relaxation time, and band-tail density of states, respectively.

In order for diffusion to not dominate our measurement signal, we need the carriers to complete their transit before the charge sheet is entirely degenerated into a

distribution so broad its transit time cannot be accurately determined. This indicates

$$\tau_{drift} \ll \tau_{DR} \tag{3.8}$$

where τ_{DR} is the dielectric relaxation time of the material, or the time required for a charged region to equilibrate with the surrounding material. This gives us the more specific requirement

$$\frac{d^2}{\mu_{drift}} \ll \frac{\epsilon\epsilon_0}{\sigma} \tag{3.9}$$

where ϵ is the relative permittivity of the sample, ϵ_0 is the permittivity of free space, and σ is the sample conductivity. This requirement is at odds with the requirements of our measurement, namely that the transit time must be long with respect to the resolution of the measurement device. Practically, these both impart requirements on the necessary device thicknesses in order to both resolve the transit of the carriers (large d) and have the transit occur before the the charge sheet relaxes beyond resolution (small d). It is entirely possible for many systems that these lengths be incompatible (*i.e.* the requirements overlap making no values of d satisfy both), in which case the measurement is not possible without resolving one of these issues. It should be noted that this can often be overcome by heating or cooling the sample, as increasing the temperature generally increases μ_{drift}, ϵ and σ, with the specific relation between the properties for the material determining the effectiveness of the method.

The case of dispersive transport is less straightforward to model, but also less likely to cause failure of the measurement. Trapping and release of charge carrier from band-tail states causes a change in the exponential decay of the current transient both before and after time τ_{drift}. This is generally written as

$$I_{t<\tau_{drift}} = t^{-(1-\alpha_1)} \tag{3.10}$$

$$I_{t>\tau_{drift}} = t^{-(1+\alpha_2)} \tag{3.11}$$

where $\alpha_{1,2}$ are simply decay parameters used to describe the ideality of the signal.

In the special case where the transport becomes non-dispersive (*e.g.* the temperature is high enough to allow rapid re-emission from traps) we see $\alpha_1 = \alpha_2 = 1$. The modeling of these decay parameters $\alpha_{1,2}$ have received considerable attention, with the hope that they can be used to deduce the band-tail states. The review of this literature is beyond the scope of this work, but for more information please see Refs. [68, 69, 70, 71].

3.2.3 Sample Measurement

In practice, for the determination of mobility these different alpha values are manifest in a change in slope of the current transient, when plotted on a log-log scale. This allows for determination of τ_{drift} as the point (or more realistically, region) where slope transitions. This is depicted in Fig. 3-3, showing the two regimes of constant power-decay, as well as their intersection determining the transit time τ_{drift}. The liner fits are determined either through a least-squares regression over an estimated linear region of the curve, or hand-fit to the linear regions, both yielding values within the systematic error of the measurement. Furthermore, once a slope ($\alpha_{1,2}$) has been established for one applied bias (V) for a sample device, it is held constant for the subsequent bias applications. This is essential as at high bias conditions (low transit times) the rounding from the internal capacitance of the system on the short timescales makes determination of α_1 more difficult. Conversely, at low bias conditions (long transit times) the non-ideal transport disrupting the flow carriers, leading to a lower, noisier signal make determination of α_2 more difficult, for reasonable transit times. This is also demonstrated in Fig. 3-3 – the green curve is well characterized by the two linear regimes, although shows increased noise in the collection region, whereas the purple curve shows a less ambiguous collection regime, the transport region is overly rounded.

Once τ_{drift} has been established for all investigated voltage conditions (usually 5-7 per device, at 2-3 devices per sample), the plot of the product of the cell thickness and field as a function of the drift time is constructed, and the slope (Eq. 3.7) is determined. This is shown for two samples in Fig. 3-4, the higher slope line

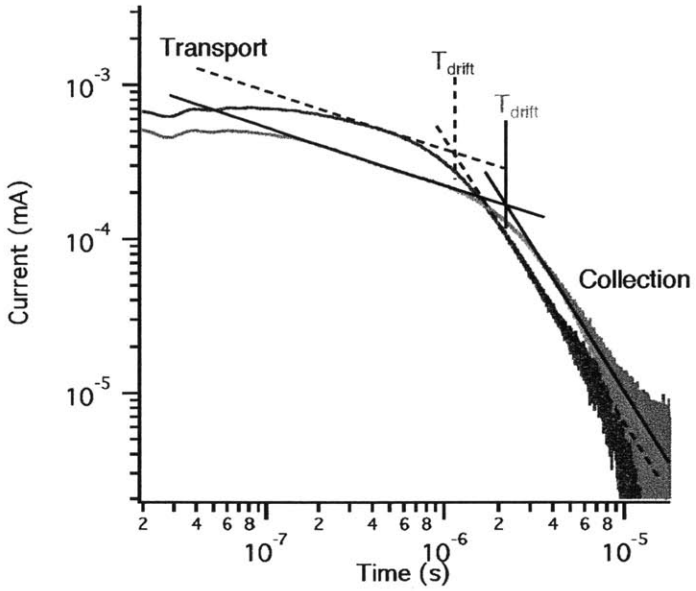

Figure 3-3: Example of two time-of-flight transients showing the linear collection and transit regimes on the log-log scale, along with the drift time,τ_{drift} determined by the intersection of the extrapolation of the two linear regimes.

corresponding to the higher mobility sample. Because the uncertainty at the extrema voltages is often higher due to the phenomena depicted in Fig. 3-3, the mobility is calculated for three regressions: the full set of data, and the data excluding the highest and lowest bias voltages. The mobility is reported as the average of these values, with the variance of the three used to calculate the uncertainty of the reported mobility.

3.3 Fabrication and Pre-Mobility Characterization

3.3.1 Device Deposition

3-inch diameter, <100>orientation, single crystal silicon (c-Si) wafers were used as the substrates for all devices. The wafers were p-type, doped with boron to resistivities of 0.01-0.02 ohm-cm, and used as the rear contact. Immediately before deposition, substrates were cleaned with solvents followed by 7:1 buffered oxide etching (BOE) to remove any native oxide. Wafers were inspected visually to ensure the surface was uni-

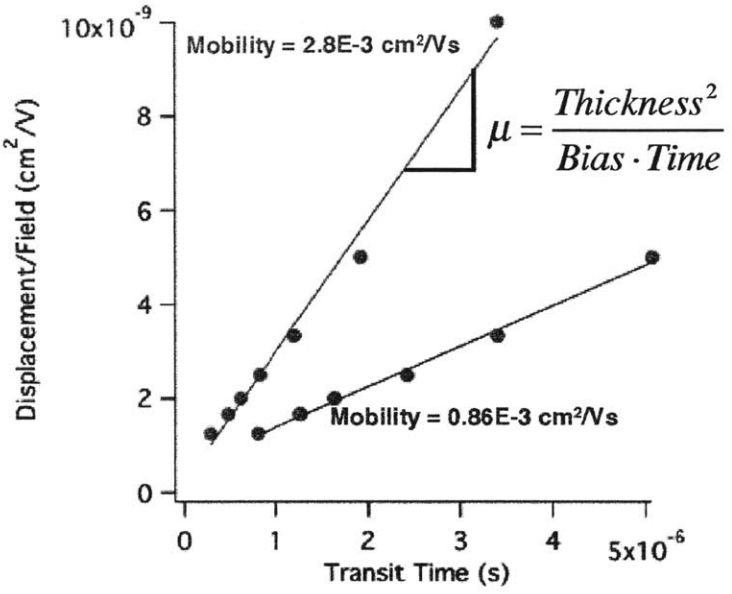

Figure 3-4: Plot of the bias-thickness product as a function of transit time, used for the calculation of mobility. Adapted from figure by C.B. Simmons.

formly hydrophobic. All a-Si:H depositions were performed using a plasma-enhanced chemical vapor deposition (PECVD) tool built by Surface Technology Systems. The depositions were performed with a RF frequency of 13.56 MHz, at a discharge power of 30 W, using a 182.4 cm^2 platen (grounded), and the platen and upper electrode heaters were fixed at 200° C. The platen to electrode spacing was 25 mm.

Before deposition an "etchback" was performed on the chamber, consisting of a plasma cleaning using C_4F_8 to remove any remnants of previous films. The chamber is then conditions using first an oxygen plasma etch to remove remaining fluorine from the etchback process, followed by a SiO_2 deposition of ~100 nm to both promote adhision to the chamber walls and coat any remaining impurities. The *p*-type a-Si:h is then deposited in 50 nm thickness to prevent oxygen or other contamination, and to ensure the deposition is occurring nominally.

The devices were fabricated with sequential *p*, *i*, and *n* layer depositions, all in a single chamber. The intrinsic layers were deposited using pure silane with a flow rate of 55 SCCM. Doped a-Si:H layers were produced by adding dilute phosphine (1% in

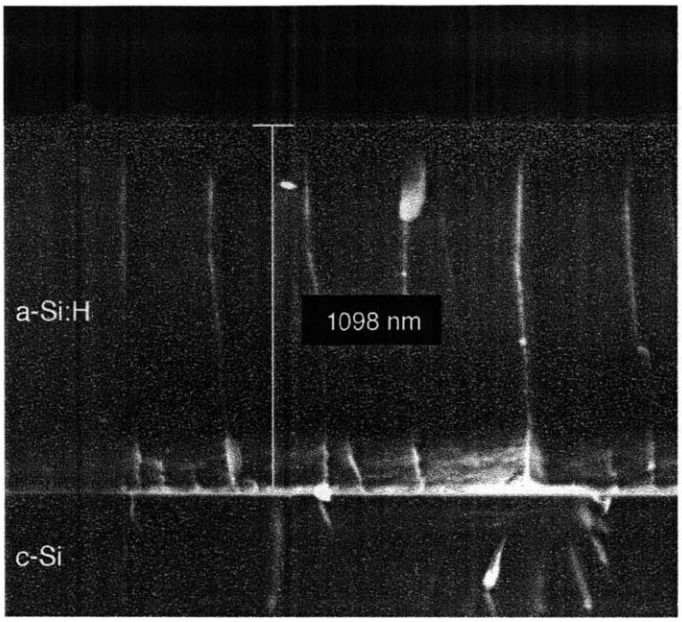

Figure 3-5: Cross-sectional SEM micrograph of normal a-Si:H device. The a-Si:H layer thickness is demarcated via the green measurement bar, and the shading on the left indicates the a-Si:H film and c-Si substrate.

hydrogen balance) to the silane depositions for the n-type, and dilute diborane (5%, in argon balance) for the p-type layers, at flow rates of 55 and 20 SCCM, respectively. The n-i-p layer thicknesses were 25 nm, 1000 nm, and 30 nm, respectively. The relatively large thickness was chosen to facilitate the measurement of the time-of-flight hole mobility. Devices were inspected under dark-field illumination at 10-20x magnification to ensure no "bubbles," pin-holes or delamination was present in the films after the substrate cooled to room temperature. Substrate curvature measurements (see below) for stress determination were conducted immediately before substrate cleaning, and after film deposition.

Cross-sectional SEM images (Fig. 3-5) were taken to determine the thickness of the amorphous layers, critical for accurate calculation of the mobility. Top contacts were 25 nm thin gold contacts, with a 5 nm titanium adhesion/blocking layer between the contact and the doped a-Si:H surface. Contacts were deposited using electron beam evaporation at 20°C. The front contacts determined the device sizes, with each device being 2x2 mm squares, and spaced at 5 mm between the edges of the devices. The

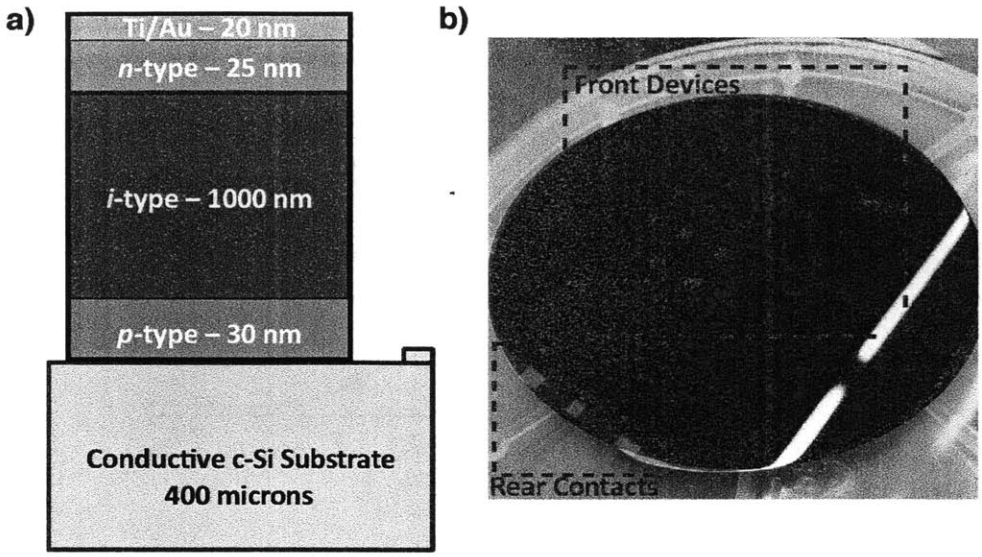

Figure 3-6: **a)** Schematic of time-of-flight device configuration, consisting of a semi-transparent Au (18 nm) contact, with a Ti adhesion layer (2 nm), followed by a *n-i-p* a-Si:H stack of the approximate thicknesses demarcated, all on top of a degenerately-doped conductive crystalline silicon substrate. Rear contacts are deposited directly on the substrate with the same Ti/Au deposition as the front contacts. **b)** Photograph of a full sample on a 3" wafer, showing 25 devices and 3 rear contact spots.

devices were centered on the substrates to avoid the variation in material thickness present at the far edges of the substrate, and 10-25 devices were present on each substrate. Identical contacts were additionally deposited directly onto the substrate surface to provide points for contacting the wafer. Devices were confirmed to have an open circuit voltage of >0.7 V under AM1.5 illumination prior to further testing, in order to ensure good quality of the deposited layers and contacts. Trials were performed before the main sample deposition to ensure the thin contact layer did not influence the stress of the samples, within the standard measurement error of ~5-10 MPa.

3.3.2 Raman Crystallinity Measurements

All depositions included a quartz substrate adjacent to the silicon substrate. Both the silicon and quartz substrates were used for confirming the amorphous nature of our

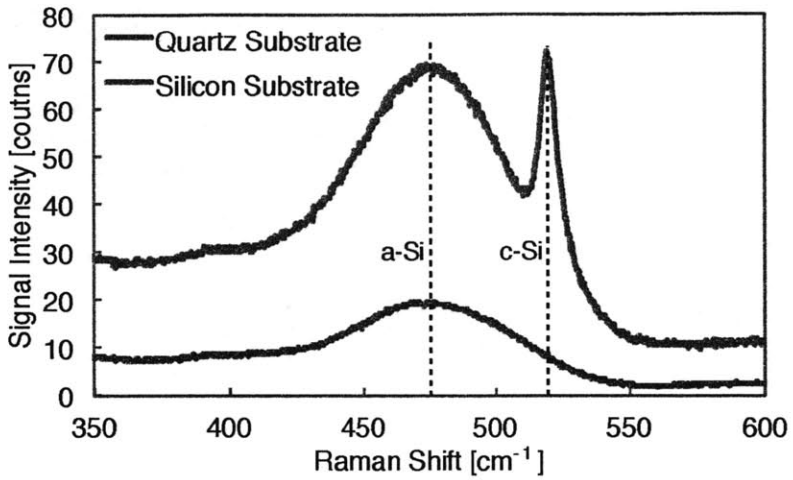

Figure 3-7: Raman traces of a-Si:H films deposited on quartz and c-Si wafers. The c-Si peak is present in only the c-Si substrate trace.

samples, with the quartz substrate specifically chosen to remove any possible interaction of the crystalline silicon substrate with the Raman signal. Raman measurements were performed on a Horiba LabRam-HR800. Care was taken to ensure proper focus of the probe beam, essential to minimizing the substrate influences convolved into the measurements of the crystalline silicon substrate samples.

3.3.3 Hydrogen Content

Measurements of hydrogen content are performed using Fourier transform infrared (FTIR) spectroscopy, using a Perkin-Elmer Spectrum 400 FTIR spectrometer. All measurements are performed on c-Si double-side polished wafers, with a circular spot size of 8.5mm in diameter. Traces are taken and averaged 10 times, and measured with a 0.5 cm^{-1} precision. Hydrogen content calculations are first done by filtering the interference fringes present in the data in the Fourier domain, baselining the data to the trace minimum below the 2000 cm^{-1} peak, and fitting two Gaussian peaks to the data. The Gaussian functions are then integrated, and normalized by the values recommended in Ref. [72]. Integration of the 2000 cm^{-1} peak corresponds to silicon monohydride concentrations, and the 2090 cm^{-1} peak corresponds to the concentration

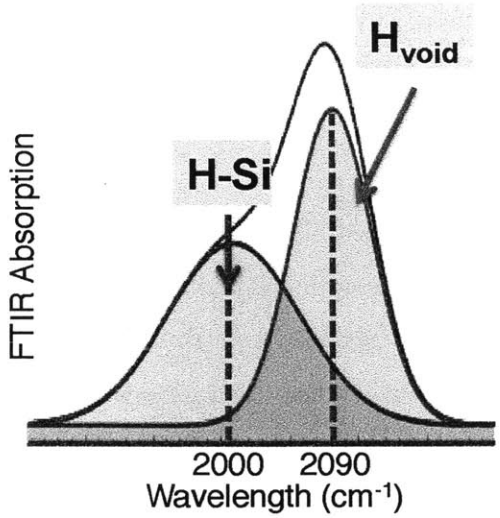

Figure 3-8: Diagram showing deconvolution of 2000 and 2090 cm^{-1} peaks in the FTIR trace of a-Si:H, allowing determination of the hydrogen content in the silicon monohydride and polyhydride/void configurations, respectively.

of silicon polyhydride as well as hydrogenated voids, as shown in Fig. 3-8. Results are shown in Fig. 3-11b. The dashed line in Fig. 3-11b corresponds to the point at which peak heights are no longer resolvable, and thus serves as a noise floor for our measurement. The difference of the noise floor level for the two hydrogen contents is due to the different scaling factors needed for the two hydrogen contents [72].

3.3.4 Stress

Stress measurements are performed by a comparison of the substrate curvature before and after deposition. Substrate curvatures are measured using a Toho FLX-2320-S, with substrate thicknesses measured using a calibrated micrometer with 1 micron precision, immediately before the first curvature measurement. Our stress calculations assume a <110> c-Si biaxial modulus of 1.805x10^{11} Pa. Measurements are performed 5 times on each of two orthogonal substrate orientations, and then averaged for the final stress, with the standard error in the measurements represented in the error bars

in Fig. 3-11. Film stress, σ_f, is calculated using Stoney's formula

$$\sigma_f = \frac{E_s h_s^2 \Delta\kappa}{6 h_f (1 - \nu_s)} \tag{3.12}$$

where E_s, h_s, and ν_s are the substrate Young's modulus, thickness, and Poisson ratio, respectively, h_f is the film thickness, and $\Delta\kappa$ is the change radius of curvature of the system before and after film deposition. Curvature measurements are confined to the inner portion of the wafer to ensure the assumptions of Stoney's formula hold. [73] The measurements represent the total film stress (intrinsic stress + thermal stress), although thermal stresses in these films are quite small (likely between 7-14 MPa [74]) due to both the similar coefficients of thermal expansion between a-Si:H and the c-Si substrate, as well as the fairly low deposition temperatures (200° C).

3.3.5 Deposited Sample Data

ID	Pressure mTorr	Thickness nm	Stress MPa	σ_{stress} MPa	Time s	Rate nm/s
1	200	1290	-516.7	10.4	4219	0.306
2	250	1260	-345.1	5.2	3388	0.372
3	275	700	-355.9	5.7	2460	0.285
4	300	1250	-179.0	0.1	2519	0.496
5	325	1010	-229.8	8.6	2483	0.407
6	350	770	-164.1	4.3	2079	0.370
7	350	1080	-150.8	5.6	2230	0.484
8	375	950	-98.3	4.2	2006	0.474
9	375	895	-89.4	7.3	1906	0.470
10	390	874	-76.9	20.7	1802	0.485
11	400	1136	-51.1	5.0	1888	0.602
12	400	920	-43.0	6.0	1732	0.531
13	400	1150	12.7	0.7	1888	0.609
14	425	853	17.7	3.4	1529	0.558
15	450	988	67.1	11.2	1529	0.646
16	475	999	111.7	4.6	1419	0.704
17	500	1000	154.2	2.8	1280	0.781
18	525	950	165.1	1.4	1213	0.783
19	600	1180	247.8	2.4	967	1.220
20	600	1080	279.8	1.3	967	1.117
21	700	1043	290.1	11.7	832	1.254
22	800	1100	377.2	4.4	796	1.382

Table 3.1: Deposition conditions and film properties determined during deposition for all samples investigated here. σ_{stress} represents the standard error of the mean for the stress measurements.

3.4 Time-of-Flight Hole Mobility Measurements

3.4.1 System Overview

The custom-built time-of-flight setup used an Ekspla NT342B-10-W400 tunable laser, operating at a relatively short wavelength of 400 nm to ensure absorption was dominantly at the device surface. The pulse duration was 5 ns running at 10 Hz, and directed through a Coherent continuously variable attenuator (C-VARM), in order

to decrease the pulse energy to ~1 nJ. Bias voltages were applied using a Hewlett-Packard 33120A function generator, set to initiate from the signal of the laser Q-switch. Applied voltages ranged from 0.9 to 10 V. Measurements were taken using an Agilent 54855A oscilloscope, which records 1000-2000 averaged traces in order to obtain the photocurrent transients. A background trace of identical length, taken with the laser blocked at the source, was obtained immediately prior to each measurement and subtracted from the signal. A diagram of the setup is shown in Fig. 3-9.

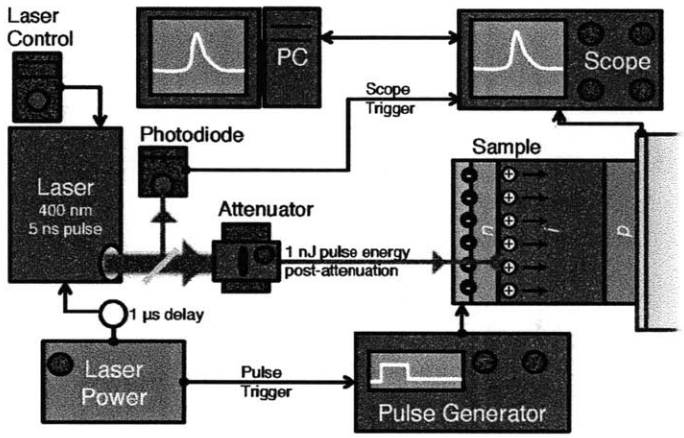

Figure 3-9: Schematic of the time-of-flight setup used for hole mobility measurements. An image of the setup is shown in Fig. 3-10.

3.4.2 ToF Measurement

The experimental measurement of hole mobility begins by mounting the sample to a vertical stage, allowing placement of the devices in front of a fixed beam path. The sample is contacted with two micro-manipulator probes, with the front of the device corresponding to the n-type region, as electrons should be extracted in order to measure the hole transport. The back contact is connected to the scope to measure the current transient occurring from he charging of the rear contact. The connections are made with two BNC cables of equal length, and the shielding shorted to the table surface. The length of the BNC cables are minimized to avoid excessive RF interference from the firing of the laser. Furthermore, for the particular setup used

here, we found that if the oscilloscope was placed in the plane of the table, excessive RF noise would be convoluted with the signal, so it was held on a cart below the plane of the optics setup.

The laser is next put in a low power ("adjust" setting) mode at a 532 nm wavelength, and the sample is aligned into the beam path by monitoring the signal output on the oscilloscope until maximized. Once aligned, the laser is set to full power at 400 nm wavelength for the measurements.

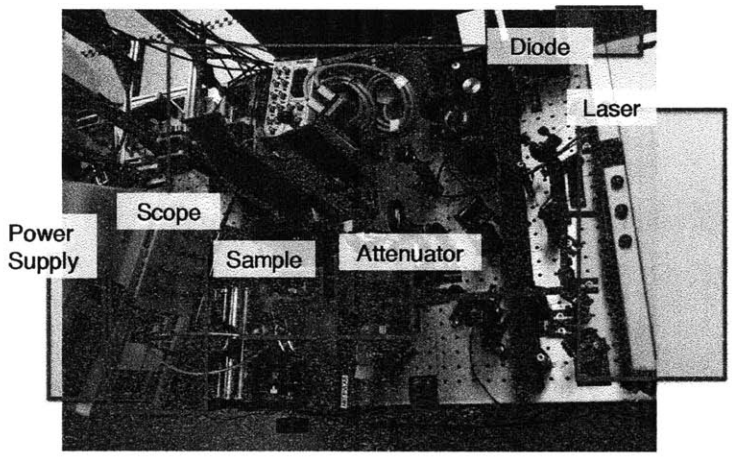

Figure 3-10: Image of the time-of-flight setup, with the key components highlighted. A schematic diagram of the setup is shown in Fig. 3-9.

The measurement begins by a custom LabVIEW program configuring the oscilloscope over GPIB to acquire a set of 1000-2000 measurements, triggered on a signal from a photodiode viewing the laser. The laser power supply sends a signal every 0.1 seconds, initiating the application of the bias voltage from the function generator. After a set delay of $\sim$2 μs, determined to allow full relaxation of the space charge region inside the *n-i-p* device to equilibrium, and thus maintain a nearly constant electrical potential across the device, the laser is fired. The function generator produces a square wave signal for $\sim$500 μs total, deemed both long enough to allow the entirety of the transient to be captured, while still allowing re-equilibration of the device to the ground state between measurements. The beam passes through a variable attenuator, adjusted to allow only $\sim$1 nJ of pulse energy through, and then hitting

the sample. The trace is recorded and averaged on the oscilloscope, which finally transfers the averaged trace to the computer for analysis. Each device is measured at four or more values of V (1-10 V), which is essential to accurately measure mobility, as it is observed both here and elsewhere [17] that ToF mobilities from single-voltage measurements are dependent on the applied bias. Immediately prior to each measurement a background trace of identical length, taken with the laser blocked at the source, is obtained and subtracted from the signal, to remove additional noise from the laser power supply and firing.

The obtained traces are plotted on a log-log scale, and then processed via a two-component piecewise linear regression to obtain the transit time, as shown in Fig. 3-3. A range of at least 5 transit times at different applied voltages is then used to fit a second linear regression, the slope of which provides the hole mobility of the sample, as shown in Fig. 3-4. An average of two devices were analyzed for each sample, and the results averaged to give the final mobility. The measurement uncertainty is represented as the error bars in Fig. 3-11.

3.5 Results and Discussion

3.5.1 Experimental Mobility

While our films are produced via variations in deposition pressure, we present our experimental trends with respect to the measured film stress, as this provides a coordinate that is both indicative of the physical properties of the material (as opposed to the deposition apparatus), as well as easily, reliably, and accurately measurable.

As shown in Fig. 3-11, the mobilities of our a-Si:H films span an order of magnitude, peaking with a mobility of $\sim$.01 cm2/Vs (similar to that observed in Ref. [75]) at the intermediate compressive stress of approximately -51 MPa, and declining rapidly on either side. It is also interesting to note that the mobility declines somewhat more rapidly in the tensile stress regime than the compressive. We also observe that the silicon monohydride (Si-H) concentration is monotonically increasing as compressive

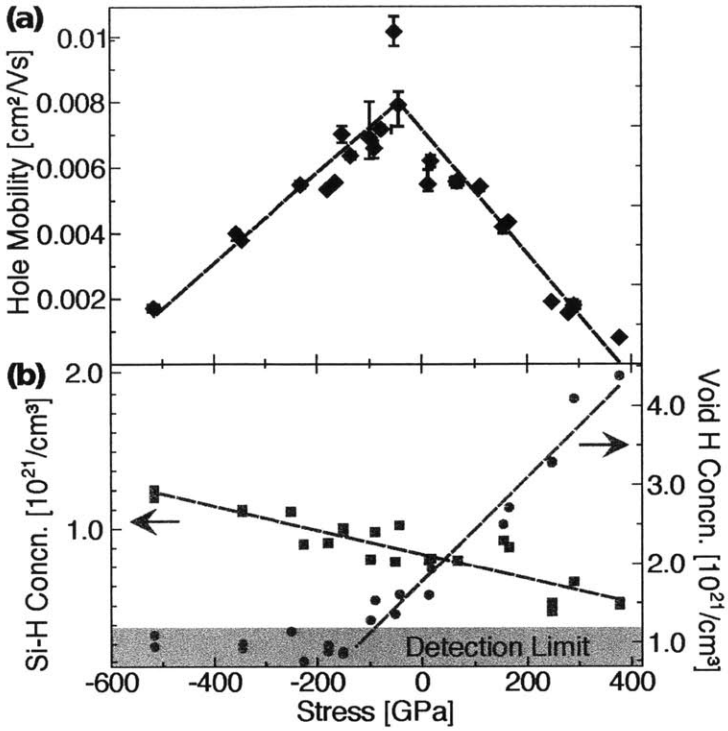

Figure 3-11: Mobility **(a)**, and film hydrogen content **(b)** separated into voids (red), and Si-H bonded H (blue), as a function of film stress. Dashed lines represent linear regressions. Error bars represent the standard error of the mean values.

stress increases, and that the hydrogenated void content starts to increase above its detection limit at stresses > -100 MPa.

While high mobility value of 0.0102 cm^2/Vs at -51 MPa appears somewhat anomalous, we could find no evidence to discredit the results and justify removal from the set – the sample appears still fully amorphous in Raman measurements, remains in good agreement with neighboring samples in terms of hydrogen content in both bonding configurations, and was measured over four different devices. While the variance was higher than most other samples (as seen in the larger error bar for the mobility), the measurements were still quite consistent. It is also interesting to note that in this entire region (~-100 to +50 MPa) the variances in mobility are substantially higher than those of other samples. This could be partially due to the mobilities being higher, and thus the measurement setup having a more difficult time measur-

ing fast transport, but the particular higher variance in samples with even slightly higher mobilities than their neighbors (e.g. the -43 MPa sample) suggests that these highest mobility materials may be in a metastable configuration, and that the slight variances, even across a sample, could be detrimental to the performance.

We note that the peak mobility here occurs at an intermediate (non-extrema) position for stress and hydrogen concentration in both bonding configurations. This is interesting as it goes against the conventional wisdom of optimizing device performance by limiting the polyhydride/void hydrogen (2090-2100 cm^{-1}) peak, and suggests that either this configuration can be somewhat beneficial to the optimization of mobility, or occurs coincidentally with other variables optimal for higher mobility.

3.5.2 Table of Results

ID	Pressure mTorr	Stress MPa	Si-H cm^{-3}	Void H cm^{-3}	Mobility cm^2/Vs	$\sigma_{mobility}$ cm^2/Vs
1	200	-516.7	1.07E+21	1.07E+21	1.71E-03	3.5E-05
2	250	-345.1	1.00E+21	1.05E+21	3.78E-03	2.0E-05
3	275	-355.9	1.09E+21	1.14E+21	3.98E-03	9.9E-05
4	300	-179.0	8.48E+20	9.04E+20	5.32E-03	2.4E-05
5	325	-229.8	9.66E+20	7.97E+20	5.47E-03	8.8E-05
6	350	-164.1	1.28E+21	1.59E+21	5.55E-03	8.8E-05
7	350	-150.8	9.13E+20	9.43E+20	7.02E-03	2.5E-04
8	375	-98.3	9.55E+20	1.46E+21	6.90E-03	1.1E-03
9	375	-89.4	9.82E+20	1.53E+21	6.59E-03	2.2E-04
10	390	-76.9	9.66E+20	1.68E+21	7.17E-03	1.4E-04
11	400	-51.1	7.87E+20	1.29E+21	1.02E-02	4.6E-04
12	400	-43.0	1.02E+21	1.61E+21	7.91E-03	4.0E-04
13	400	12.7	7.67E+20	1.53E+21	5.50E-03	4.4E-04
14	425	17.7	8.45E+20	1.93E+21	6.21E-03	1.6E-04
15	450	67.1	8.34E+20	2.04E+21	5.58E-03	1.4E-04
16	475	111.7	*	*	5.43E-03	9.2E-05
17	500	154.2	6.92E+20	2.73E+21	4.20E-03	2.0E-04
18	525	165.1	9.02E+20	2.71E+21	4.34E-03	3.6E-05
19	600	247.8	6.40E+20	3.03E+21	1.91E-03	2.0E-05
20	600	279.8	6.92E+20	3.09E+21	1.56E-03	1.5E-05
21	700	290.1	7.22E+20	4.09E+21	1.80E-03	1.6E-04
22	800	377.2	6.19E+20	4.12E+21	8.09E-04	3.4E-05

Table 3.2: Hole mobility and hydrogen content data as determined for all samples in this study. The "*" denotes measurements that could not be taken, due to sample damage. $\sigma_{mobility}$ represents the standard error of the mean for the mobility measurements.

3.6 Conclusions

In this chapter we have discussed a basis for the experimental measurement of hole mobility in a-Si:H, and performed such measurements over a wide range of samples. We observe a peak mobility value that occurs at intermediate values of compressive stress, and hydrogen content and bonding in the two configurations. We see a sharp falloff in the directions of either increasing tensile or compressive stress, with the

tensile stress falloff more rapid. We also see a higher variance at higher mobility values, even beyond what would be expected from the uncertainty in shorter transit times.

The following chapter is largely devoted to understanding the origins of these phenomena, investigating the interplay between three main defects: floating bonds (FB), ionization displacement (ID) defects, and lattice expansion (LE) allowing favorable hole delocalization.

Chapter 4

Influence of Hydrogenated Amorphous Silicon Microstructure on Hole Mobility

4.1 Introduction

4.1.1 Motivation

While a-Si:H PV devices have lingered in the ~10% efficiency range for more than a decade, and the low hole mobility has been widely accepted as the main barrier to efficiency improvements [33], there remains much disagreement as to the detailed atomic structures responsible for the deficient mobility.

4.1.2 Previous Work

Several recent studies attempt to identify the dominant (or, more realistically, the range of) structural defects responsible for trapping holes in a-Si:H, with theories ranging from the traditional dangling bond (DB; silicon under-coordination) [24, 25, 26, 27, 23] and less prevalent floating bond [30, 32] explanations, to larger-scale features such as filamentary structures [55] and voids [76, 77], to metastable structures such as hydrogen motion [78] and hole self-trapping defects.

Our own previous computational investigation into structures influencing hole trapping in a-Si:H found that a particular self-trapping defect showed the strongest correlation with deep hole traps – it was shown that local rearrangement of the a-Si:H atomic structure under the addition of a hole to the system allowed for more energetically-favorable localization of a hole in the proximate region (and was thus referred to as an ionization displacement defect) [79], as discussed in Chapter 2. Floating bonds, or over-coordinated Si atoms, showed the second largest correlation in our ensembles, while DBs contributed little to the band-tail trap states. Additional works have experimentally measured hole mobilities in deposited films over ranges of deposition conditions [80, 66, 75], and modeled the densities of band-tail states implied from these measurements [68, 71, 81, 82, 70]. Studies have also sought to measure densities of coordination defects experimentally, namely through EPR, although recent work has shown that such results are challenging to interpret because of the importance of the surrounding geometry on the measurement of the coordination defect [83]. However, despite this abundance of work, a detailed understanding of the atomic structure of hole trapping mechanisms over a range of experimental deposition conditions (necessary to satisfactorily sample the large configuration space possible for a-Si:H) is still lacking.

4.1.3 Outline

In this chapter we aim to connect atomic structure to observed mobility through a series of investigations, leveraging computational simulations to correlate atomic-level phenomena with empirical mobility trends, providing insight into the shifting regimes of prevalent defects. The work is conducted in three main thrusts:

First, by extending our previous computational study of structural defects in a-Si:H to include variations in both biaxial stress and hydrogen concentration, we are able to determine how changes in on the bulk material properties of a-Si:H shift the dominant defects responsible for hole trapping.

Second, through comparison of our computational ensembles to the physical samples created in the Chapter 3, we are able to hypothesize on the sources of defects in

the various experimental conditions of the material observed in the previous chapter, as well as design additional experiments to validate these theories.

Finally, we deconvolute the stress and hydrogen contents in our previously-deposited films, and measure the change in the hole mobility after the stress has been modified without influencing the hydrogen content. This thereby provides experimental evidence to corroborate our computational theories as to the dominant defects and their sources in the continuum of experimental samples produced.

4.2 Methods

4.2.1 Computational Sample Creation

The computational results in Ref. [79] show that ID defects are predominately responsible for the deep band-tail traps in an a-Si:H ensemble with ~10% H and neutral stress. It is known that both the stress and hydrogen content vary depending upon the deposition condition [10]. Here, we capture these variations in our computational models by comparing six different ensembles comprised of two hydrogen contents (~10% and ~5%) and three stress states (-1, 0, +1 GPa), and we show that these changes in the film properties correspond with a modification in the prevalence and impact of defect types listed above.

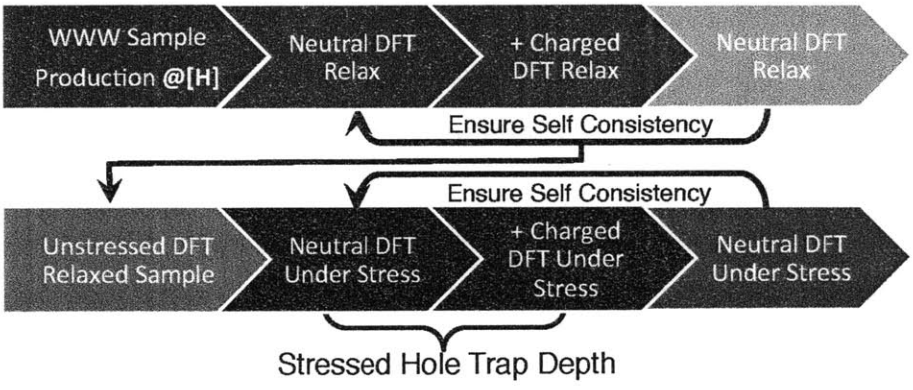

Figure 4-1: Flowchart from Fig. 2-5, modified to include application of stress; depicting the sample generation process.

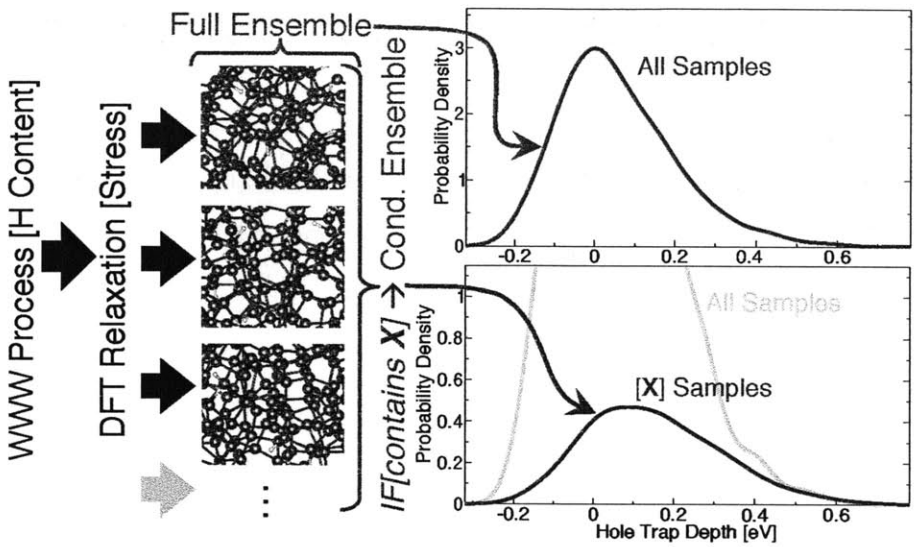

Figure 4-2: Schematic representation of computational sample creation and analysis process.

Computational samples are constructed by first generating 216 Si + 10 or 20 H atom structures using a modified WWW [46] process, then relaxing the structures and computing the total energies in the density functional theory (DFT) package SIESTA [48]. The procedures are identical to those discussed and tested in our previous work [79], with the only modifications being the targeting of specific stress states, and an additional ensemble created with a lower, ~5% hydrogen concentration. Hole trap depth (HTD) analysis also proceeded identically to the above-mentioned work, investigating ensembles of 1200 a-Si:H structures, allowing full relaxations both before and after introduction of the hole into the system, converging these structures to ensure the hole-induced relaxations are fully reversible, and taking the energy difference between these structures as the ionization potential of the structure. This energy is subtracted from the peak of the ionization potential distribution, giving the HTD of a specific structure in the ensemble. After being created, these structures are analyzed to determine the level of presence of various defects. These factors are then used to filter the ensembles to create the conditional probability density

plots, allowing for the examination of the influence of a single feature on the full trap distribution. This process is depicted in Fig. 4-2.

Finally, it is important to note that we choose sample properties of stress and hydrogen content to be on the scale of those experimental samples observed, but toward more extreme values to explore trends within a more reasonable sampling size. While modeling conditions identical to physical films is possible, the size of ensembles needed to make unambiguous, statistically significant comparisons between similar films would become computationally prohibitive.

4.2.2 Back-Side Film Deposition Validation

In our experiments we utilize additional depositions of a-Si:H on the back sides of our substrates to independently manipulate the stress state of the front side film (by forcing bending or relaxation of the substrate). We have verified that, to our measurement capability, hydrogen content and bonding configuration are not changing during deposition of the back-side deposited (BSD) films for stress modification, and that the front films are not being influenced by the second deposition process itself. This was done in three steps – first back side films were deposited on wafers that were covered by a secondary substrate. This allowed us to isolate the influence of the film being deposited on the surface from the conditions the film was subjected to in the PECVD. We observed no measurable change in the mobility of the sample before and after measurement. Second, we co-deposited a BSD film on a test sample, along with a new, clean c-Si fragment. FTIR analysis was then performed on both substrates, with the latter substrate used as a background for the former, allowing us to isolate influence of the front film. We observed no noticeable change in neither the FTIR signal nor the hydrogen content measurements. Third, we confirmed this lack of change by repeating the previous experiment, followed by etching away the back film, and re-measuring the hydrogen content, again observing the FTIR absorption traces, and computed hydrogen contents, to be indistinguishable from the initial measurements.

4.3 Results and Discussion

4.3.1 Computational Hole Traps

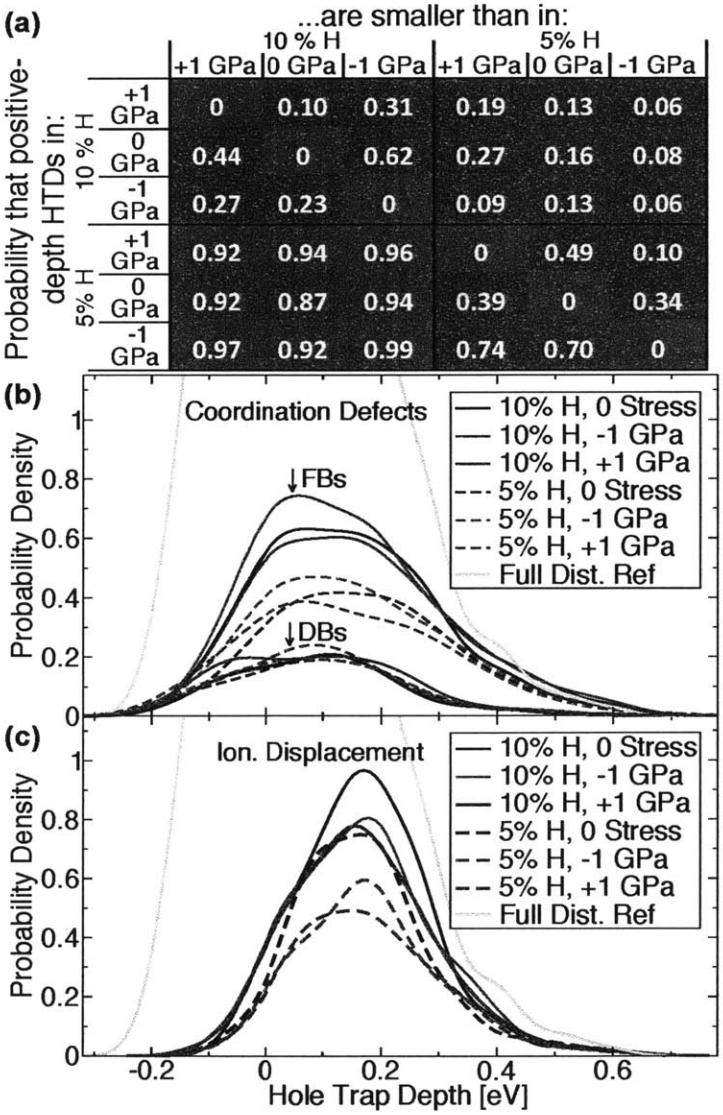

Figure 4-3: **(a)** Probabilities that positive HTD tails in the row ensembles are smaller than those in the columns. **(b,c)** Conditional probability density distributions of the hole trap depths of computational samples containing: **(b)** FBs and DBs, and **(c)** IDs. Light gray lines reference full HTD distributions (10% H, no stress).

In Fig. 4-3, we explore the nature of the extended tails in the distributions of hole trap depths of samples within our six computational ensembles. Specifically, the positive-depth band tails here are of critical importance to hole transport as hole trap time is exponentially dependent on trap depth [70]. In Fig. 4-3a, we examine the probabilities (computed using a single-sided two-sample Kolmogorov-Smirnov test) of the positive-depth traps in the ensemble of a given row being smaller than that in a corresponding column. The red-to-blue coloration denotes the low-to-high probability continuum. We observe that the lower hydrogen ensemble has nearly ubiquitously lower trap values than the higher hydrogen states, evident in the >0.9 probabilities in the lower-right quadrant of the table. This indicates that at a fixed stress, decreasing hydrogen content corresponds to decreased band tail HTDs. Within a given hydrogen content, however, we see no ensembles that are clearly (p >0.9) smaller than their counterparts.

In Fig. 4-4 we display the full hole trap depth distribution peaks and tails (on a semi-log scale). One can note the similarity in the extended positive-trap depth tale on this scaling, elucidating the need for statistical analysis in the form of the probability table in Fig. 4-3a. The coincidence of the peaks at 0 eV is mandated by our trap depth scaling as we elect to use this point (statistical mode) as the representative "bulk" of the material, and thus giving any alternate energy as the propensity for a hole to exist in that location, relative to the bulk. While the negative trap depth tails vary as well, these are less interesting for transport as isolated barriers to hole motion in a three dimensional environment will not disrupt hole movement across a gradient (such as the drift-based transport dominant in a-S:H PV) to the same degree that attractive traps will.

To understand the more complex behavior of the band tails under stress application, as well as gain insight into the causes of the increasing tails with increasing hydrogen, we decompose the distributions to investigate the specific trap levels and prominence of FBs, DBs (Fig. 4-3b), and IDs (Fig. 4-3c) within our ensembles.

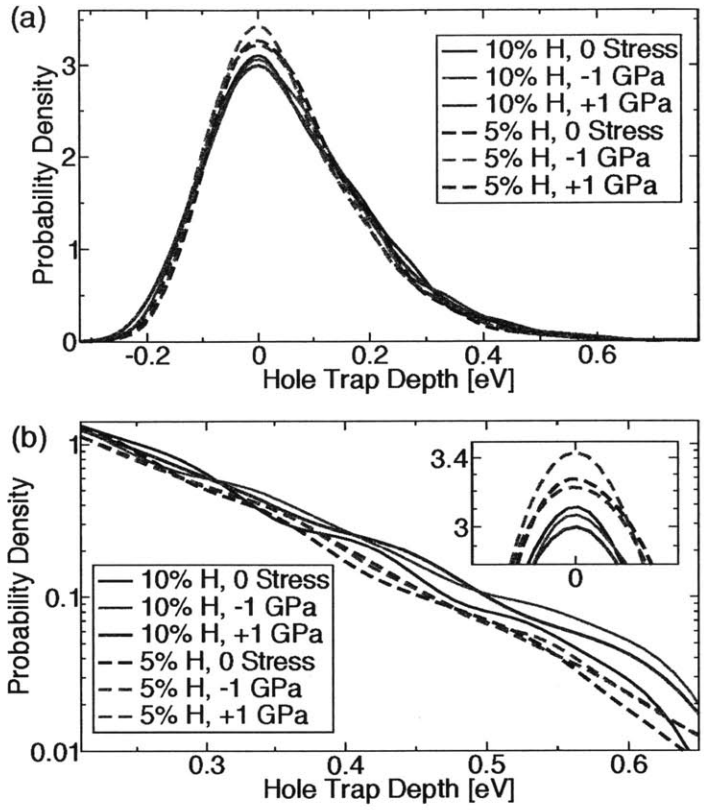

Figure 4-4: Full probability density distributions of the hole trap depths across the six investigated ensembles, on linear (a) and semi-log (b) scales, with inset shown to highlight peak behavior.

4.3.2 Coordination Defects

In Fig. 4-3b, we investigate the influence of structures containing one or more floating or dangling bonds in our ensembles, with bonded silicon defined as atoms with a separation of less than 2.75 Å [79]. We plot density functions of the probability of finding hole trap depths in the ensemble when filtered by said conditions (*e.g.* contains FB). This allows us to ascertain the prevalence and severity of the FBs and DBs on the hole trapping in the full ensemble (gray). Moving from 10% [H] to 5% [H] (solid to dashed curves) reduces the density of FB across the entire HTD distribution, while the application of compressive stress (red) increases the density of FB relative to the unstressed (black) ensembles, and tensile stress (blue) reduces said

density. These trends are easily understood: decreasing the hydrogen in the structure limits the number of bonds needed to be satisfied, and thus decreases the propensity toward FB creation in the structure, while compressing the material decreases bond distances, making FBs more likely. DBs were observed to universally contribute less substantially to the band tails within the studied ensembles, in agreement with previous results [79, 83]

4.3.3 Ionization Displacement Defects

In Fig. 4-3c, we observe that ID defects increase with both increasing H concentration and decreasing the magnitude of stress in a sample. Here we define IDs as those samples containing an atomic displacement greater than .11 Å under the charge removal. We see that in both hydrogen content ensembles the application of stress reduces the incidence of moderately high HTD ID defects (HTD $>$ 0.1 eV), but also that decreasing the hydrogen in the samples causes the expression of fewer IDs. We believe that this is due to the less-constrained Si-H bonds (hydrogen is usually bonded to only one, or at most two silicon atoms [84]) allowing a higher degree of bond rearrangement under the added potential of a hole being introduced into the system, and thus allowing stronger hole trapping. In the tensile stress regime, it is interesting to note that the decrease in occurrence of IDs and FBs does not explain the overall increased tails in the full hole trap distributions (seen in the generally higher values in the positive stress columns of Fig. 4-3a), nor the correspondingly decreased experimental mobility (Fig. 3-11a). To understand these features we look beyond atomic defects, and investigate the behavior of the hole wavefunction.

4.3.4 Lattice Expansion

In Fig. 4-5 we plot the hole trap depth distribution as a function of the localization length of the hole wavefunction in our samples, calculated using the methods set forward by Silvestrelli [60], and Resta and Sorella [59]. We observe that the lattice expansion caused by tensile stress allows delocalization of the hole wavefunction around

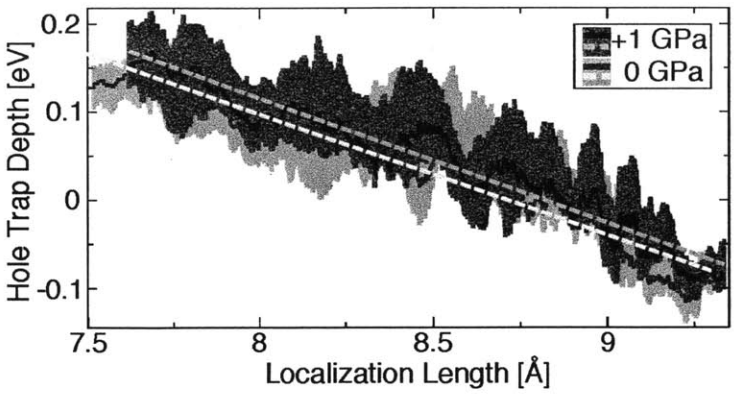

Figure 4-5: 10% hydrogen ensemble HTD distributions represented by the peaks (solid lines) and first quartiles (shaded regions) of the probability density, plotted continuously against localization length of the hole wavefunction. Dashed lines represent linear regressions to the peak values.

potential trapping structures, lowering the kinetic energy penalty of a highly localized wavefunction, thereby yielding deeper trap depths. Considering the mechanism by which IDs trap holes (increasing localization lengths in a given area, causing stronger trapping), it is fitting that by expanding the a-Si:H lattice, tensile stress is essentially leading to the same effect as the IDs in unstressed samples. We see that while both stress states express strong correlations between hole trapping and the localization of the hole, the tensile ensemble shows: 1) longer localization lengths than the unstressed ensemble, indicating that tensile stress is indeed allowing delocalization; and 2) that the hole trap depth becomes more dependent on the localization length when tensile stress is applied, seen through the higher slope (0.0044 eV/Å), confirmed to 99% confidence, as well as the +1 GPa peak (black) remaining nearly uniformly above the unstressed ensemble (blue). These effects, combined with the rapid increase of hydrogenated voids in our experimental samples, begin to explain why we obtain a sharp decline in hole mobility of our films with increasing tensile stress, as well as agreeing with previous experiments measuring decreased hole mobility under applied stress in polycrystalline films [85].

4.3.5 Electronic Density of States

In Fig. 4-6 we show the electronic densities of states (DOS) for the six different computational ensembles we explore here. We note that all of the DOS are quite similar, with the main variation being a slight increase in state density on the valence band side of the 10% hydrogen ensembles. This fits with the results shown in Fig. 4-4, with the 10% hydrogen content HTD distributions appearing slightly less ideal, namely with increased tails on the negative trap depth side. This would correlate to increased band tail states on the conduction band side, as observed here in Fig. 4-6.

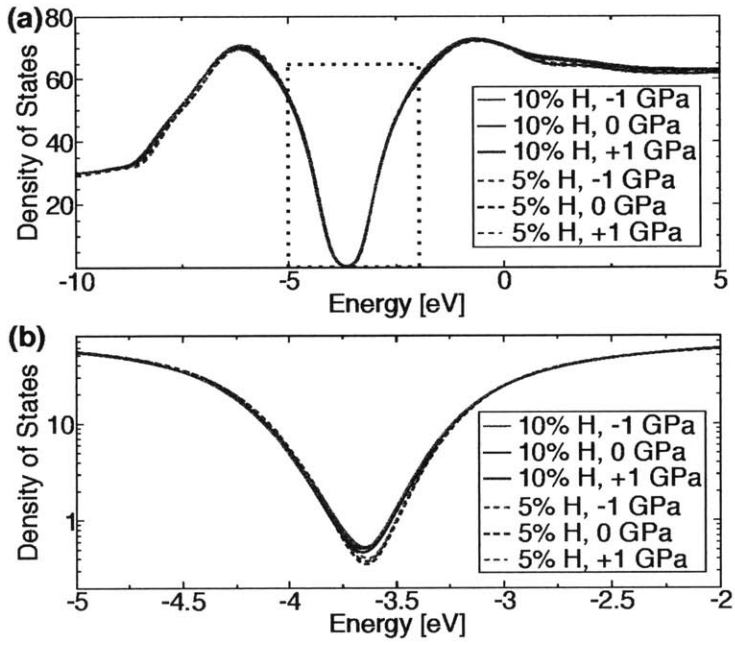

Figure 4-6: Comparison of averaged electronic densities of states (DOS) for the six different ensembles, showing **a**, full calculated DOS, and **b**, a semi-log plot of the band gap region.

We next examine how coordination and ionization defects influence the electronic density of states (DOS) of the ensembles. In Fig. 4-7 we compare the full ensemble average DOS (black) to that of the presence and removal of the three examined defect states - dangling bonds, floating bonds, and ionization displacement. In Fig. 4-7a, we note that the DOS of the DB defects increase the density of states mid-

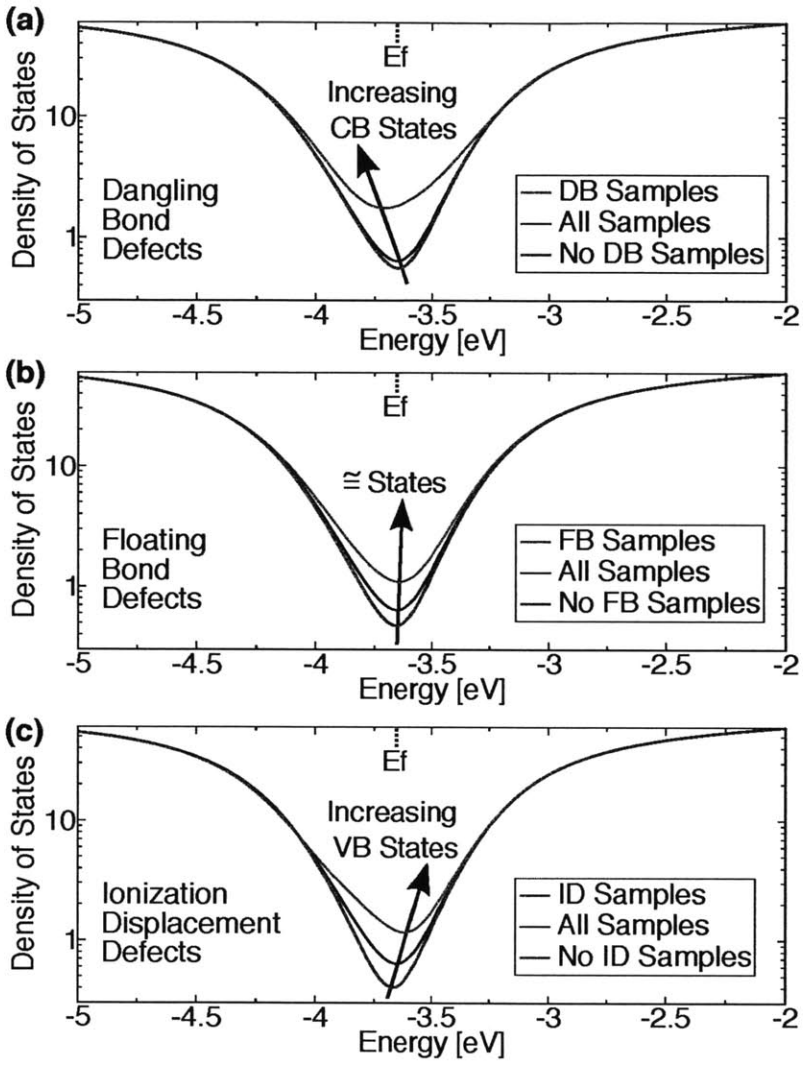

Figure 4-7: Semi-log plots of the electronic densities of states in the 10% hydrogen, neutral stress ensemble, shown for the positively charged structures. Indicators display relative increases in conduction band (CB) and valence band (VB) state densities, and the bulk fermi energy (Ef).

gap considerably, but more substantially toward the conduction band states than the valence band, as visible through the arrow connecting the minima of the DOS. Furthermore, the low prevalence of these defects relative to the other two in our ensembles limits their influence on the sample hole trapping, as visible by the minor change in the DOS of the full ensemble with all DBs removed (blue).

In Fig. 4-7b, we see that FB defects have a similar influence, although with more equal distribution of defect states onto the valence and conduction bands, and also that the defect presents a greater influence on the total ensemble DOS, again visible through the difference between the full ensemble (black) and that with the FB defect-containing samples removed (blue).

Finally, in Fig. 4-7c we observe that ID defects have the most significant influence on the valence band DOS, fitting with our previous observations indicting these defects as the most highly correlated to significant hole trap depths. We also see the removal of these defects as having the most significant influence on the full distribution (difference between blue and black lines) of the three defects.

It should be noted that while the DOS here represent those calculated via GGA-DFT, which introduces systematic error in the band positions (most notably through the gap underestimation), these errors have been studied in depth and it is believed while the absolute positions of the bands contain inaccuracies, the relative behavior within a system should remain accurate [86, 79, 51]. Furthermore, we see the same trends for the uncharged samples, and little difference between the DOS for the 6 ensembles investigated here (shown in the Supplementary Material).

4.3.6 Connection between Experimental Mobility and Computational Hole Traps

Through the confluence of the results presented here, we can establish a better understanding of the mobility trends in Fig. 3-11, adapted in Fig 4-8.

In the compressive stress region, the sharp decline in mobility is attributable to two factors: the high compressive stress levels increase the density of floating bonds

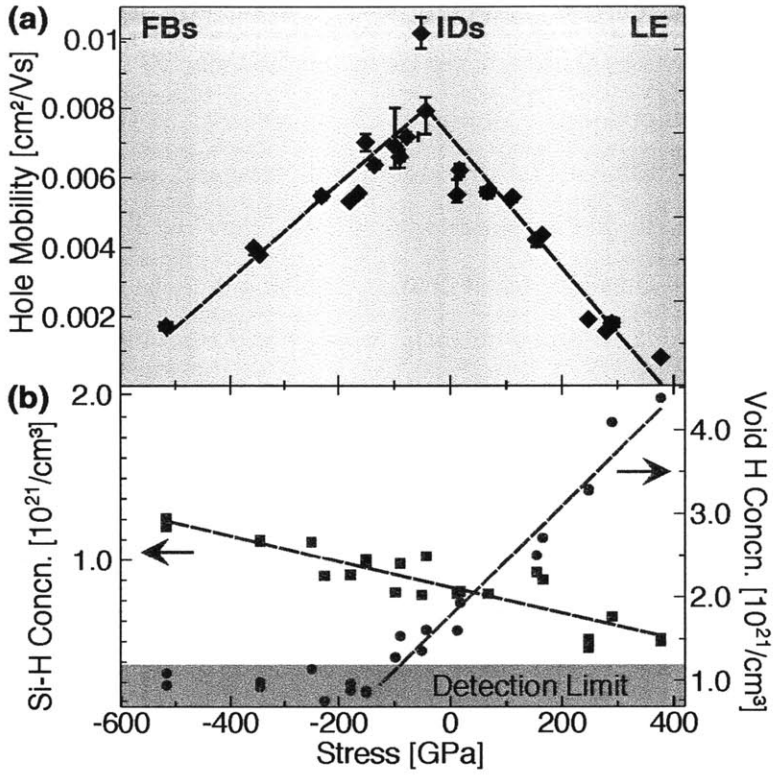

Figure 4-8: Mobility **(a)**, and film hydrogen content **(b)** separated into voids (red), and Si-H bonded H (blue), as a function of film stress. Top labels and color shadings indicate the increased defect concentrations in three regions: floating bonds, ionization defects, and lattice expansion. Dashed lines represent linear regressions.

substantially, and while the compressive stress also somewhat limits the occurrence of IDs, the concomitant increase in Si-H concentration not only counteracts this by increasing IDs, but also further increases the FB density as well. In the tensile regime, while we do see a decline in both the FB and ID concentrations computationally, we also observe the a longer localization length of hole wavefunctions, as well as a stronger dependence between localization and hole trapping in the tensile-stressed samples, indicating that the lattice expansion could be allowing holes to localize over larger regions within the structures and thus become strongly trapped, similar to the filamentary [55] and void [76, 77] structural traps explored elsewhere. Finally, these tradeoffs in our structures, between compressive stress limiting the occurrence of IDs, but promoting FBs; as well as a low Si-H density being beneficial, but occurring

experimentally under otherwise-unfavorable tensile stress, and void-rich conditions, explain why we see both a peak mobility at an intermediate stress condition, and why the repeatability of the material quality between devices becomes more unstable as the mobility increases. These findings are summarized through the shading and labeling at the top of Fig. 4-8a.

Deconvoluting Stress and Hydrogen from Mobility Experimentally

While these results elucidate atomic configurations potentially limiting the mobility in the various stress regimes of our samples, it is important that we take steps to experimentally vet our explanations. In support of this, we perform an additional experiment with the objective of deconvoluting the total stress in the a-Si:H films from the hydrogen content (and bonding configurations), and determining the independent influences on the film hole mobility. Experimentally, the film stress is modified by depositing an additional amorphous silicon film on the back side of the device substrates, which modifies the curvature of the substrates and therefore the stress in the device films without affecting their hydrogen content. We confirmed that the deposition process had no influence on the mobilities of the front-side films when the stress was not changed, and that the stress modification of the films had no measurable change in the hydrogen content of either bonding configuration in the samples (see Methods).

The key results are displayed in Fig. 4-9, confirming that lower [H] corresponds to improved mobilities. Here we focus on the compressive stress region of the trend in Fig. 3-11, as both the high prevalence of larger voids makes the tensile region less computationally accessible, and the low mobility of the region makes it less experimentally interesting. We recall from our computational results in Fig. 4-3a that while comparisons between hydrogen concentrations yield statistically relevant results for changes in HTDs, comparisons within a given hydrogen content (varying stress) were indeterminate, so we focus on samples at a single stress, investigating the trend with changing hydrogen content. The first set of samples in this study originates at low compressive stress conditions (*ca.* -80 MPa), and is shifted to increased compressive

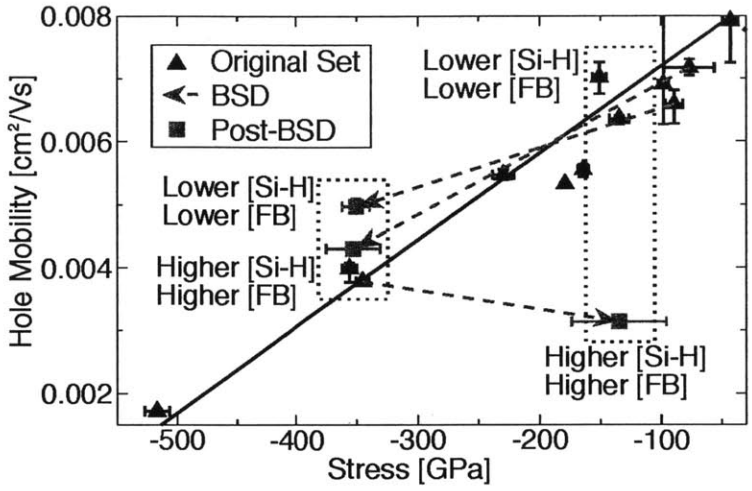

Figure 4-9: ToF-measured hole mobility of films before (black) and after back-side depositions (BSD; red). Blue dashed lines indicate the movement of samples from the BSD. Dotted boxes indicate isobaric comparisons of differing hydrogen concentrations.

stress to match previous depositions (-350 MPa; red squares). At this constant stress condition, we recall that the stress-modified samples contained a lower Si-H density than the unmodified samples immediately below them on the plot. We can thus see that at a constant stress, the samples with the lower Si-H concentration do exhibit a significantly higher mobility than those with the higher Si-H density. Additionally, by applying the opposite stress movement – taking one of the high compressive stress samples (-350 MPa) and reducing the stress to a more moderate condition (-135 MPa), we see that this sample is of a lower mobility than those containing a lower Si-H concentration. Although direct confirmation of the atomic defects dominating the hole trapping in our samples is experimentally untenable, these experiments do provide agreement with our computationally based results, supporting our postulate that the mobility-limit defects are not a single structure, but an interplay between FBs, IDs, as well as potentially further undiscovered defects. We should also note that while lower hydrogen content proved beneficial here, extreme reduction of this property could lead to a new regime in which other deleterious influences begin to dominate.

4.3.7 Mobility from Hole Trap Distributions

While hole trap depth distributions are clearly related to the mobility in a device, it is challenging, if not untenable to actually derive a hole mobility from these probability distribution functions. Three main issues preclude this conversion being done easily:

First, there exists a trade-off between the weighting of a small number of deep hole trapping structures in an ensemble against a larger number of more shallow traps – while the deeper traps will clearly confine a hole for a longer period of time (due to the exponential relationship between trap time and hole trap depth), once a structure has trapped a hole, it can be thought of as passivated, and thus will not continue to trap further holes, until either the first carrier recombines or is released. A simple thought experiment to clarify this trade-off can be examined by imagining the extreme cases of trap distributions: on one hand we could have a crystalline system (delta function at zero hole trap depth probability density), but with a single structure with an extremely deep hole trap state. An exponential weighting of our trap depths (as trap time alone would indicate) would give an extraordinarily low "mobility" for this ensemble average, as the single large trap would dominate the mean trap time, but in a physical sample this single trap would only be recombining a single carrier for the lifetime of the hole. Conversely, a distribution with quite extended tails, as shown to be quite deficient in performance in Fig. 2-1, would appear to have a higher relative mobility. This contradiction clarifies the need for a more complex system than simply considering the mean exponential trap time alone.

Second, as suggested above, it is necessary to not only know the release time of a hole trap, but the recombination time of the carrier in the sample. This requires not only accurate knowledge of the positions of the conduction and valence band densities of states for a trapping structure, but also those around it, a problem quite well known to be difficult in DFT, and part of the motivation of our examination exclusively of *relative* energies. Furthermore, experimental measurements of the hole lifetime in a-Si:H are also widely varied, precluding a simple use of empirical data for this term.

Finally, while our calculation of hole trap depths as a measurement relative to the ensemble average ionization potential (see Chapter 2) allows a convenient determination of the average trapping propensity of a structure, for a conversion to mobility, the local structure begins to matter increasing as well – we are not simply moving from a single structure to the bulk, but through a three-dimensional space of particular surrounding structures. This means that not only are the structures themselves relevant, but so are the arrangement of them we are interrogating. Furthermore, when examining the transport of carriers though a sample, we also care not only of the trapping of the carrier in the full structure, but the localization location within the sample, and the level of the other proximate geometries within said sample. While this may be possible to analyze in large configuration that can be subdivided into smaller interrogable regions, the limited size of our samples (necessary for our large averaged ensembles) make this again somewhat untenable.

These issues begin to clarify the difficulty in explaining the secondary trends observed in Fig. 4-9 – while the probability table in Fig. 4-3 helps to elucidate the trends between the atomic-level defects present in different microstructural conditions, the uncertainty in the weighting of the positive-depth hole trap tails prevents more concrete conclusions of the superiority of one ensemble over another (in terms of hole transport) from being drawn.

This said, while the exact trends are difficult to analyze, we believe the correlations between the experimental trends in Fig. 4-8 and the atomic structures demarcated in the figure not only provide valuable physical insight into the limiting phenomena present in the materials, but also hold potential suggestions for future methods to improve hole mobilities within in the material (see Chapter 6).

4.4 Conclusions

While the results discussed here cannot provide an exhaustive description of the nanostructural hole traps possible in a-Si:H, we believe that they represent an important step in understanding the changing interplay between atomic-level defects in

amorphous silicon devices. Furthermore, the presence of multiple defects, controlled by interdependent material properties (*e.g.* stress, hydrogen content) provides evidence for why despite decades of research, hole mobilities in a-Si:H still fall far below those theoretically possible for free-carrier transport through an amorphous material [33, 81, 87]. Finally, the results and methods presented here can be generalized to the study of other directionally bonded disordered semiconductors, with the evidence of the interdependent nature of defects in these materials solidifying the need for future works to be cognizant of, and adaptable to, this variability.

Chapter 5

Nanostructuring of Hydrogenated Amorphous Silicon for Improved Hole Transport

5.1 Introduction

5.1.1 Motivation

As discussed in the preceding chapters, the low hole mobility, due mainly to the extended band-tail states in a-Si:H prevents effective hole transport, and thus limits current collection. The practical implications of this, other than limiting the efficiency of a-Si:H photovoltaic devices, is that the devices are made much thinner than would absorb the majority of the available (above-band gap) solar illumination. This is demonstrated in Fig. 5-1, showing the power produced by two hypothetical a-Si:H PV material devices under solar illumination with differing band-tail states as well as a real device, as a function of thickness. The physical device and 50 meV simulation both show power saturation around 400-500 nm thicknesses, as the probability of collecting carriers excited further than this from the front contact becomes negligible. The 40 meV simulation shows that even a slight improvement in the collection proba-

bilities increases the available power density significantly as more distant carriers can be collected, and thus thicker cells become increasingly advantageous.

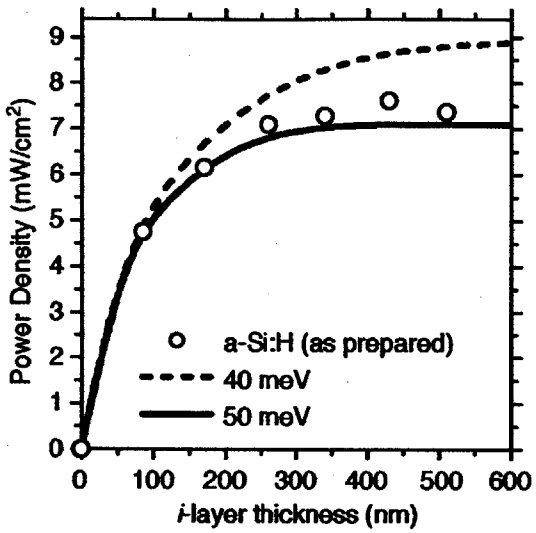

Figure 5-1: Correlation between device thickness and produced power under solar illumination, for devices with valence band-tail widths of 40 and 50 meV, and for physical samples. Reproduced from Ref. [14].

As the high number of previous investigations into the optimization of a-Si:H devices, coupled with the understanding of the innate limitations to transport in the currently-possible materials makes the further improvement of the bulk material especially challenging, in this chapter we explore methods for utilizing the beneficial properties of the material (namely the strong bulk absorption and robust surface states) to achieve a similar improvement in hole extraction (or effective mobility) from devices.

5.1.2 Previous Work

The previous work on nanostructuring of amorphous silicon (as well as other forms of silicon, for that matter) can be summarized in two categories:

The first methods aim to improve device efficiency by improving absorption, either through bulk absorption increases (*e.g.* front-side texturing allowing a longer inter-

action path length and/or decreased reflection [88, 89, 90, 91, 92], or back-side scattering or reflectors causing multiple interactions with the absorption path [93, 94]), or through increasing absorption near the surface (*e.g.* surface-plasmon enhancement [95, 96], or shallow structures causing Fabry-Perot resonance [97, 98]).

The second category focuses on improving carrier extraction from devices. This is mainly realized in the form of nanowire/-rod/-cone/ devices, but most, if not all have used crystalline silicon in order to produce these structures. This can either be done by etching bulk silicon materials away, which still requires high-efficiency (and expensive) bulk c-Si wafers [99, 100], or by a growth method known as vapor-liquid-solid (VLS), where metals are used to incorporate adsorbed and then dissolved silicon atoms into an advancing solid wire structure. These latter methods, however have suffered from very low efficiencies, usually less than a percent for reasonable device structures [101, 102], or rely on processing of single wires for higher efficiencies [103]. Other drawbacks of this method include numerous lithography and processing steps, usually involving gold, for either the VLS growth or for metal-induced etching of the materials, not only decreasing the feasibility of production due to cost and complexity, but also requiring encapsulation on the cell-level to prevent damage to the nanowire structures, and thereby reducing many of the benefits of these devices (namely their anti-reflection properties).

5.1.3 Outline

In this chapter we propose a combination of these two approaches – using ordered nanoholes etched into thick (1000+ nm) intrinsic amorphous silicon bulk layers, followed by the filling of these holes with higher mobility, p-type materials, we work to improve hole extraction from the devices through either reduced transport path lengths, increased electric field gradients, or both. This approach should also allow for increases in absorption (due to decreased reflection and increased scattering) as well as concentrated surface absorption (through optical trapping in the regions between the holes), hopefully further compounding the benefits of this approach. Finally, because the inclusion of nanoholes into bulk films should not hinder their structural

properties significantly (especially when filled), there should be no need for additional processing or encapsulation steps to ensure the devices are mechanically robust.

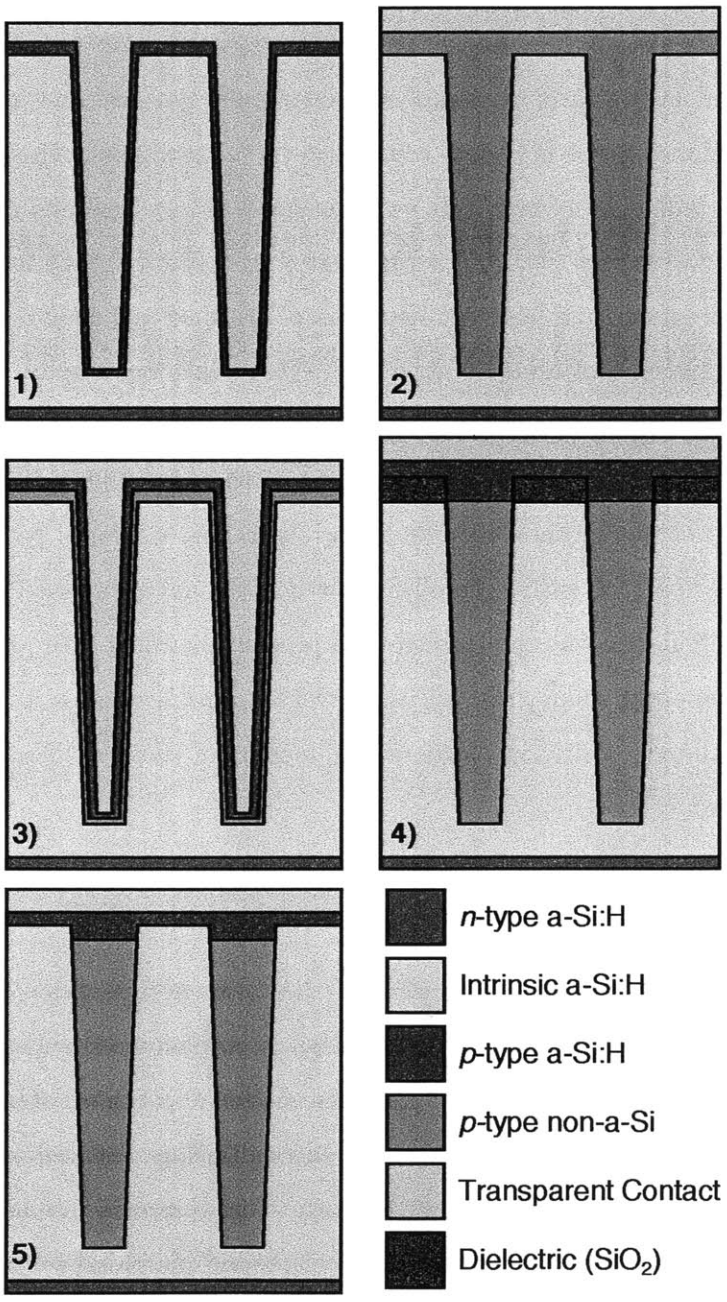

Figure 5-2: Five proposed nanohole structured a-Si:H device architectures, with the material types indicated in the lower right.

We begin by proposing five different nanohole structured a-Si:H device architectures, as depicted in Fig. 5-2:

Device 1 represents the most analogous device to planar and nanowire homojunction cells, with a *p*-type a-Si material coating the walls of the device, and a transparent conducing material (likely a transparent conducting oxide [TCO] or nano-carbon material) coating and filling the remainder of the hole volume. This would operate by shifting the transport direction from through the device to simply toward the closest hole, given that the fields align similarly to those in a planar device. Challenges in this device include ensuring the transport direction is as intended (the fields behave as expected), as well as achieving low resistivity of the filled contact (not increasing series resistance exorbitantly).

Device 2 uses a higher mobility *p*-type material (*e.g.* PEDOT:PSS or Cu_2O) to create a heterojunction cell, but without the need for permeation of the conductor into the hole. This would operate by separating holes into the p-type material, and leveraging the improved transport in this region to move the holes majority of the distance to the front contact. If the transport in the p-type material were high enough (PEDOT:PSS has reached similar conductivities as indium-tin-oxide [ITO; a popular TCO material] recently [104]), the front transparent contact could be replaced by a simple metal grid, as in c-Si devices. Challenges with this architecture include ensuring the free carrier density in the p-type material is high enough to sufficiently deplete the a-Si:H intrinsic layer, necessary to allow the space charge region to encompass the entire material and thus ensure a sufficient drift field through the device. This should be eased, however, by imposing small distances between the filled holes.

Devices 3-5 are hybrid approaches, where carriers are transitioned from the intrinsic region, to the lightly doped *p*-type heterojunction material, and then back into a thin layer of more heavily doped *p*-type a-Si:H layer. These orientations are designed to help in two regards – first, to improve depletion of the intrinsic layer by the extraction of additional free carriers into the heavily doped p-type amorphous silicon layer, and second, to provide additional field to direct carriers either more strongly toward the hole surfaces (Device 3) or toward the front contacts (selectively through

the hole interior [Device 4] or through the entire intrinsic layer [Device 5]). Specific challenges to these approaches would be tuning the doping and relative thicknesses of the materials to allow for the optimal charge extraction.

Common challenges present in all designs include the filling of small nanoscale holes, as well as ensuring good contact between the filled materials and the a-Si:H bulk, and optimization of the the layer thicknesses, hole diameters and depths.

5.2 Analytical Device Model

We begin by exploring the potential of the nanohole geometry by performing a simple analytical, semi-empirical device model comparing the performance of a hypothetical planar device to that of the a nanostructured device of the same materials.

Our model contains a few basic assumptions: that the absorption in the nanohole and planar devices are equivalent (which, as we will see later is reasonably close, if not conservative); that the field between the nanoholes is approximately the same as the field through a planar device (likely the most inaccurate simplification here); that there is no interface degradation (traps or resistances at the increased interface area); that the hole drift length is 200 nm, and the electrons are 100x that; and that there are no second-order current improvements (trap filling from the increased current density due to the smaller amount of material).

Similar to the discussion in Chapter 1, we calculate the generation rate from the solar spectrum (where $N(\lambda)$ is the number of photons present at wavelength λ), and a measured wavelength-dependent absorption coefficient of a-Si:H ($\alpha(\lambda)$), and calculate the expected current generation (I) from the collection probability of an absorbed photon (collection of the excited hole) and generation rate giving

$$I = \sum_{x}\sum_{\alpha} \alpha(\lambda)N(\lambda)Exp[\alpha(\lambda)x]d\lambda Exp[-L_{path,h}/L_{drift,h}]Exp[-L_{path,e}/L_{drift,e}]dx \tag{5.1}$$

where L_{drift} is the drift length of holes (h) or electrons (e) , x is the depth into the device, and L_{path} is the path length from the hole/electron to the p-type material;

for the planar case this is simply x for holes, and for both cases, the [cell thickness $- x$] for electrons. For the nanohole case, we assume that holes move to the closest contact, meaning it is the minimum between the distance to the front contact, and the "center of mass" average distance to a hole (calculated to be 43 nm for 150 nm holes at a 300 nm pitch). We then maximize each cell efficiency by optimizing the cell thicknesses independently in the range of 0-1000 nm, yielding an optimal planar thickness of ~500 nm, while the nanohole cell hits the limit of 1000 nm. We plot the current collection loss (carriers not collected that are generated at a given depth) for both devices in Fig. 5-3.

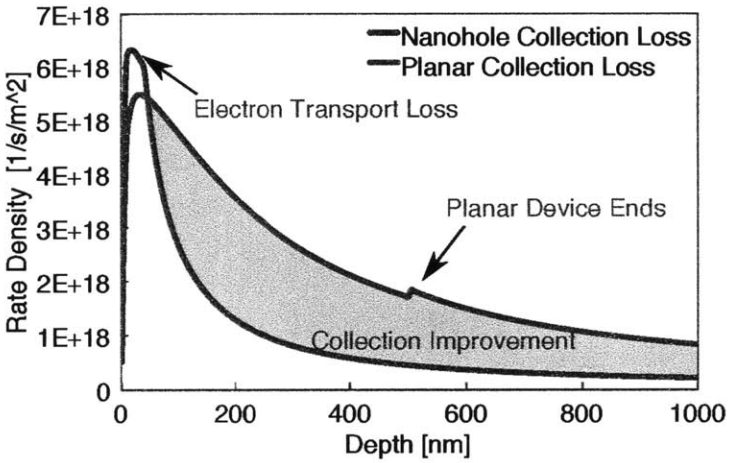

Figure 5-3: Comparison of current collection loss in planar and nanohole structured a-Si:H devices, with the shaded region indicating improved current collection in the nha-Si:H device.

One can see that the planar device loses current much more quickly as the depth is increased when compared to the nanohole device. The initial under-performance of the nha-Si:H device is due to the thinner planar cell allowing decreased electron loss due to a shorter transit distance, but is soon overcompensated by the improved hole collection in the remainder of the devices by the nha-Si:H cell. The slight uptick in loss in the planar device at ~500 nm corresponds to the device ending; all "collection loss" after that point is simply foregone absorption. The shaded red region corresponds to the improved current collection of the nha-Si:H cell relative to the planar cell, although

this must actually be discounted by the small electron transport under-performance at the surface of the devices.

The final efficiencies of the simulated devices are 9.89% for the planar device (in line with the best experimental cells [7]) and 14.29% for the nanohole device – a ~44.5% improvement. While many of the assumptions here are somewhat optimistic (namely the assumption of direct motion toward a contact in the same field as a planar device), we believe this simple simulation works well to motivate the experimental study of these devices.

5.3 Methods

In this work we focus on two of the devices proposed in Fig. 5-2, looking first at Device 1, the nanohole homojunction cell, and second (and much more briefly) at Device 2, using PEDOT:PSS as the heterojunction p-type material.

5.3.1 Nanohole Fabrication

In all devices the fabrication process begins by depositing the n-type and intrinsic a-Si:H layers. Similar to the deposition discussed in Chapter 3, plasma-enhanced chemical vapor deposition (PECVD) is used to deposit a phosphorus-doped n-type layer, of approximately 20 nm thick, followed by an intrinsic layer 1000 nm thick. A 180 nm SiO_2 layer is then deposited as a masking layer for future lithography steps.

The devices are then spun with an anti-reflection coating, and photoresist layer. Interference lithography is used to produce a linear refraction pattern on the devices, which are exposed, rotated 90°, and then re-exposed to create a circular array pattern at the intersection of the orthogonal linear refraction exposures. After development this results in a square grid of holes 150 nm in diameter with a pitch of twice the diameter (300 nm).

The patterned photoresist layer is used for etching through the SiO_2 layer, performed with CH_4 reactive ion etch (RIE), chosen for the high selectivity for SiO_2 against both a-Si:H and photoresist. This high selectivity softens the requirement

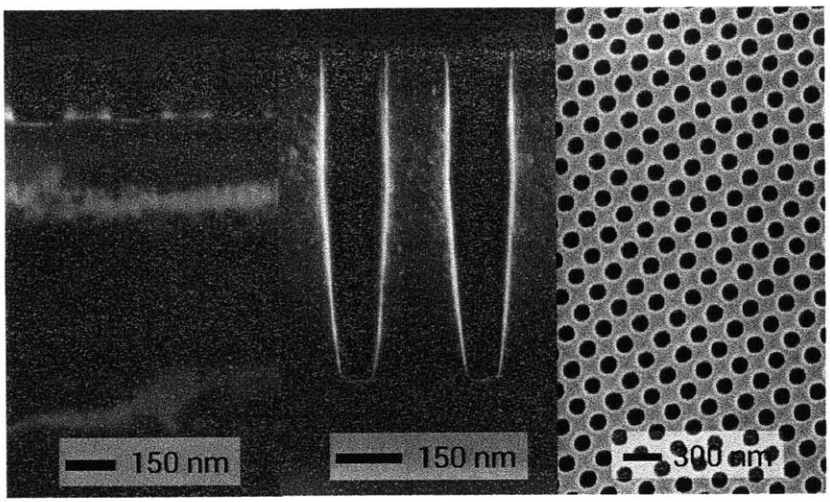

Figure 5-4: Scanning Electron Microgrpahs – **Left**: Cross-sectional view of a-Si:H layer with patterned SiO_2 layer above. **Center**: Cross-sectional view of etched a-Si:H layer with SiO_2 layer removed. **Right**: Top view of regular array of nanoholes in a-Si:H material.

on accurate etch timing as the risk of over-etching is minimal. The resulting film is shown in the left image of Fig. 5-4.

Next, the patterned SiO_2 layer is used to mask the etching of the nanoholes into the a-Si:H material. This is performed with a Cl_2 inductively-coupled plasma (ICP) RIE step. The ICP-RIE etch process is shown in Table 5.3.1. The first step is used to remove any remaining ARC material from under the SiO_2 etch on the front of the device, and the final step is to remove any further exposed ARC from removal of additional SiO_2 material during the Cl_2 etch process. The low pressure aids in both increasing the directionality of the etch, as well as slowing the etch process in order to make the etching more controllable. The etch time is of critical importance as the etch depth must be long enough to sufficiently reach the majority of the intrinsic layer, but not so deep as to short the n-type layer on the bottom of the cell to the later-filled p-type material. Because of this, cross-sectional scanning electron microscopy (SEM) images are routinely taken to ensure that the etch processes has not deviated from the nominal depth (as shown in the center image of Fig. 5-4, as well as Fig. A-1), and if there have been deviations, adjustments to the etching time are made.

Chlorine gas is chosen for the etching process for a number of reasons. First, Cl_2 plasma provides an anisotrpic (directional) etch with a high selectivity for silicon against SiO_2. Second, it does not create difficult to remove polymer films on unetched surfaces (*i.e.* sidewalls), as many deep-RIE (DRIE, or "Bosch process") processes utilizing SF_6 do. Finally, the etch is slightly less anisotropic than HBr (another common choice for hole/trench etching) allowing the formation of the slight taper on the pores, which is beneficial for certain filling processes (as explained later). It should be noted that all RIE processes can be done in a single machine at once, without requiring removal of the device in between.

Etch Step	Cl_2 Flow sccm	O_2 Flow sccm	Coil Power W	Platten Power W	Time s
1	0	20	800	0	10
2	20	1	500	75	170
3	1	20	800	0	20

Table 5.1: ICP-RIE nanohole a-Si:H etching recipe. Entire process occurs at 3 mTorr chamber pressure, with a 10 mTorr ignite step lasting for the first 4 seconds.

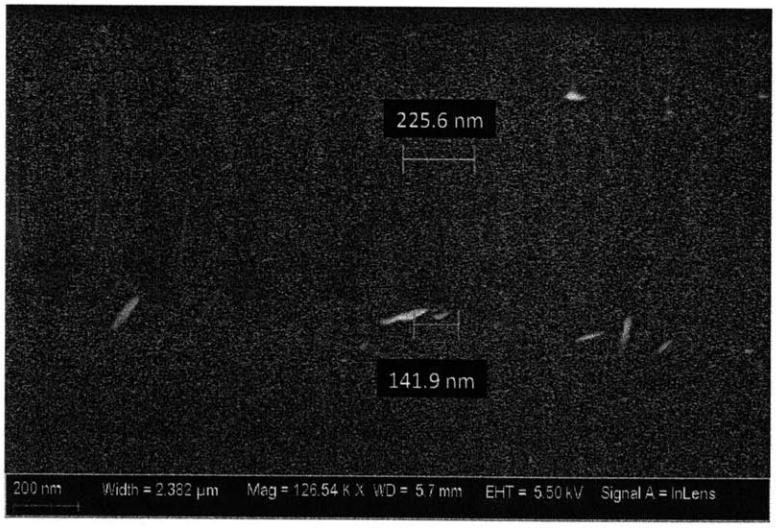

Figure 5-5: SEM image of over-etching from 15 minutes of exposure to hydroflouric acid, showing widening of the nanohole pores from ~150 nm to ~225 nm.

Once the RIE processes are complete, the SiO_2 layer is removed by wet etching in a 7:1 dilution of buffered oxide etch (BOE), a solution composed of diluted and buffered hydroflouric acid (HF). This is done for 20 seconds – care must be taken to not over-etch as the BOE solution will slowly etch the a-Si:H material as well; a fact not normally represented in the literature (see Fig. 5-5). This also confirms that the BOE solution is permeating the holes, however, and thus should also be removing any SiO2 material re-deposited from the etching process, as well as cleaning any lower-quality re-deposited a-Si:H materials. The final films show extremely regular patterns of nanholes across the entire patterned surface, as shown in the right image of Fig. 5-4, as well as a large image available in Fig. A-2.

5.3.2 Homojunction nha-Si:H Device Fabrication

After successful fabrication of the nanohole array, the holes must be filled in order to produce devices with improved current extraction capabilities. The first method of doing this is depicted in Fig. 5-6.

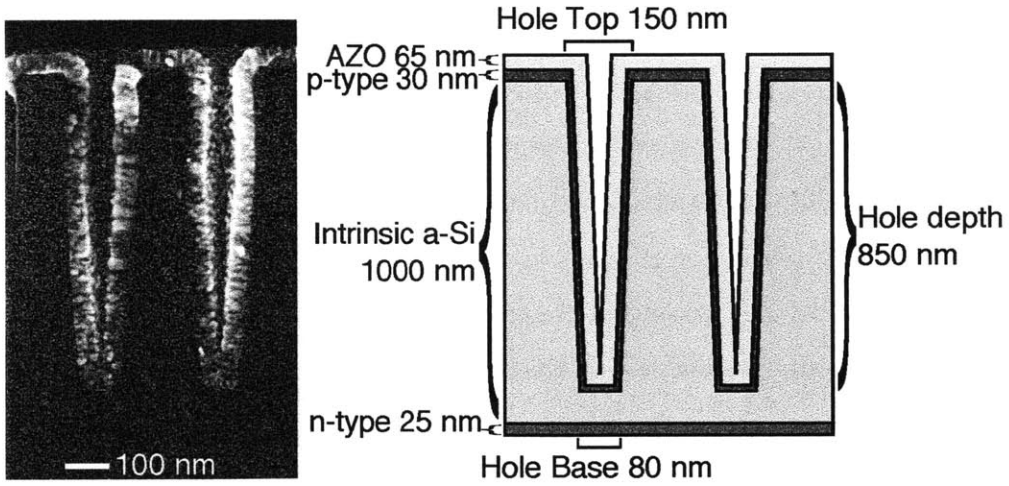

Figure 5-6: **Left**: Cross-sectional SEM image, and **Right**: schematic diagram of homojunction nha-Si:H device.

These devices are fabricated by first depositing an additional hi p-type a-Si:H layer coating the walls of the nanohole structures. In order to deposit an (at least) semi-

conformal coating, we first needed to establish the relationship between deposition conditions and PECVD conformality. Unfortunately, there existed much contradiction in the literature concerning the influence of PECVD pressure on the conformality of coatings, many references claiming PECVD is always conformal (which is not true at these aspect ratios), others claiming the conformality increases with pressure, and others claiming it decreases.

To test this, we deposited PECVD a-Si:H layers on a set of five samples, at varying deposition pressures and powers. At 100 mTorr samples were deposited at 50 and 30 W, at 500 mTorr, 30 W, and at 1000 mTorr, at 30 and 15 W, allowing us to determine the influence of both pressure (holding the 30 W power constant) and power (relative to the common 30 W case). Depositions continued long enough for the tops of the holes to become entirely covered. Through cross-sectional SEM imaging, we then measured the maximal distance between the hole sidewalls, indicating the level of coating along the walls of the nanoholes before the deposition capped the top of the features. An example image is available in Fig. A-3. The results are shown in Fig. 5-7 – we see that with increasing deposition chamber pressure and discharge power, the conformality increases, indicating the most conformal films should be deposited at high pressure and high discharge power. Unfortunately this corresponds to the highest deposition rate case as well, as deposition rate increases with both power and pressure, making thickness control, and repeatably of the deposition more difficult.

We thus deposit p-type a-Si:H layers at 1000 mTorr, at 30 W, and for 20 seconds. This is calibrated to give somewhat thick layers of 30 nm on the top surface, but should allow for more reasonable wall thickness than if we had deposited a normally more normal 20 nm layer top thickness.

After the p-type deposition we perform atomic layer deposition (ALD) of aluminum-doped zinc oxide (AZO) as the front transparent contact, using a Cambridge Nanotech Savannah Atomic Layer Deposition System. The aluminum oxide (Al_2O_3) precursor is trimethyl aluminum, and the zinc oxide (ZnO) precursor is diethyl zinc. The layer by layer nature of ALD allows precise control of both the thickness and doping ratio of the AZO, while also yielding extraordinarily conformal

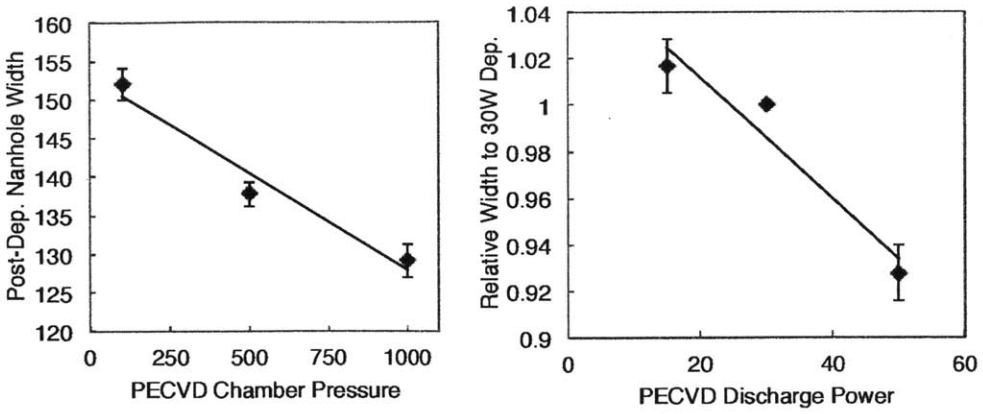

Figure 5-7: Test of PECVD coating conformality as a function of deposition pressure.

coatings. Using a 32:1 ratio of zinc oxide precursor to aluminum oxide precursor cycles, at a temperature of 150° C, we deposit 65 nm thick layers of the AZO material, necessary coating the entire sample. This thickness was experimentally determined to provide beneficial anti-reflection properties (*i.e.* was dark blue, as seen in Fig. 5-8).

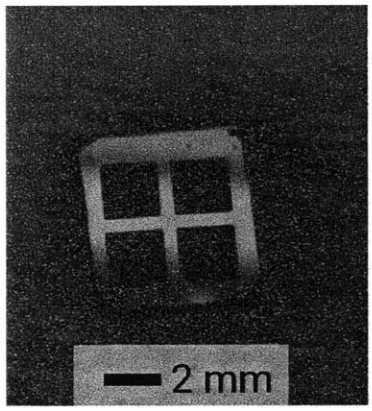

Figure 5-8: Top view of completed nha-Si:H test device.

Finally, due to the complete coating of the ALD process we must isolate devices before testing. To do this we first spin on another coating of Shipley 1805 positive photoresist, spinning at 4000 RPM, annealing the resist at 115°C, and patterning the resist using a Heidelberg uPG501 direct-write lithography system. The samples are exposed for a 27 ms dwell time, with a defocusing setting of "5." The sample is

exposed, maintaining an array of four 2x2 mm square of unexposed areas in the center of the sample, isolating the surfaces of four devices. The resist is developed using CD-26 developer for 60 seconds, rinsed in deionized water twice, and then etched using a 10% mixture of HCl diluted in deionized water for 10 seconds to remove the AZO in all exposed areas, while minimizing undercutting. The sample is then rinsed in acetone, followed by isopropyl alcohol, and dried using nitrogen. A final device is shown in cross section on the left in Fig. 5-6, and the full device is displayed in Fig. 5-8.

5.4 Results and Discussion

5.4.1 Optical Characterization

We first perform optical characterization of the unfilled a-Si:H nanohole material. By modifying the deposition to be performed on quartz substrates, we are able to acquire UV-Vis absorption data through the combination of reflection and transmission traces. Data is acquired using a Perkin Elmer Lambda 950 Spectrophotometer. Devices are fabricated identically with 1000 nm thick intrinsic layers, and in the nha-Si:H devices, an etch depth of 850 nm for the nanoholes.

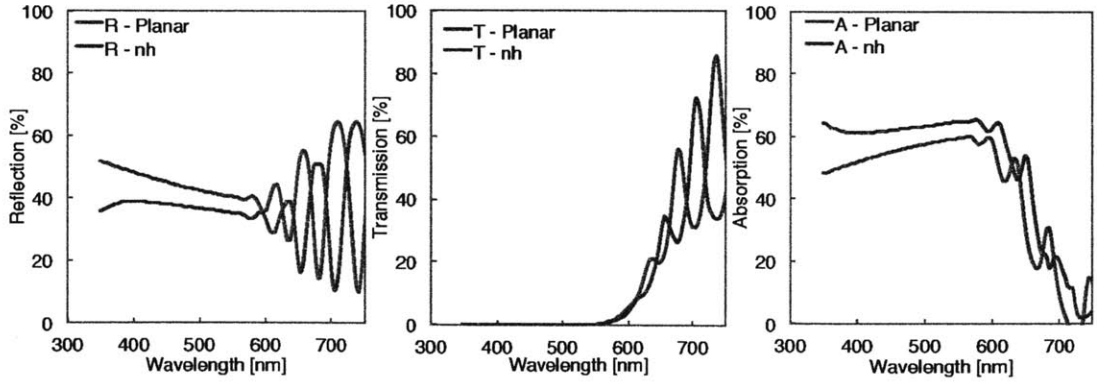

Figure 5-9: Comparison of reflection, transmission and absorption profiles for bare planar and nanohole structures.

In Fig. 5-9 we see that while the transmission of both the nanostructured and planar materials is ~0% at wavelengths below 600 nm, the nanohole material shows substantially lower reflection at these higher energies, leading to a stronger absorption profile when compared to the planar a-Si:H material. It is especially reassuring to see this lack of increased transmission as the nanohole structures have ~16% of the material removed – both preparations are identical (performed together) save the etching step removed for the planar devices. This indicates that the absorption of the nanohole structures is not simply acting as an effective medium (an average of the materials composing the nanostructure – in this case a-Si:H and air), as would be suggested by an increased level of transmission, particularly in the absorption tail region, but is actually benefiting from some constructive resonance within the a-Si:H surrounding material. While helpful in understanding the absorption mechanism in the pure nha-Si:H, these do not represent full devices and thus cannot be used directly as a validation mechanism for improvement of the devices. For this we complete the solar cells by adding the p-type layer and AZO front contact/ARC material and determine the changes in absorptance.

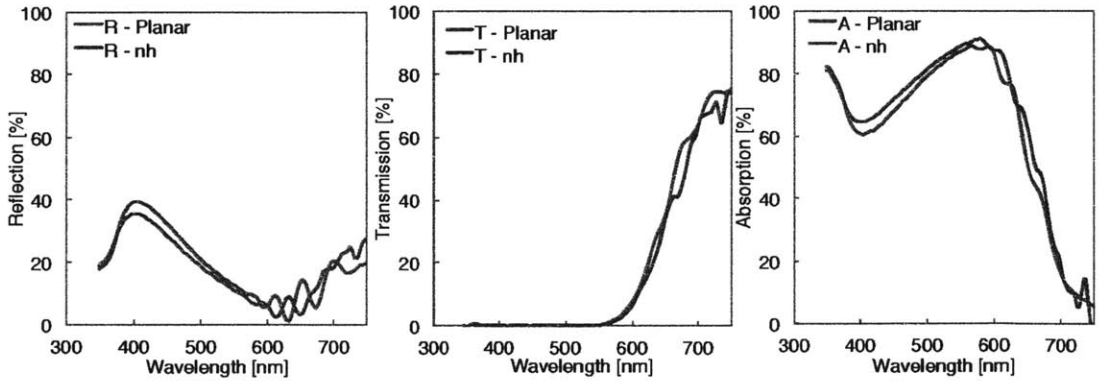

Figure 5-10: Comparison of reflection, transmission and absorption profiles for planar and nanohole structures with anti-reflection-optimized AZO coatings.

In Fig. 5-10 we observe that the inclusion of the anti-reflection AZO material has indeed worked at decreasing the reflection from both materials considerably, and most notably lowered the difference between the two architectures. We see that while the

transmission, other than the removal of the interference fringes, has not changed substantially, the reduction in reflectance has notably increased the absorption, bringing the two devices almost to parity. Through integration of the absorption of the absorption of the two devices over the solar spectrum, we can calculate that the nha-Si:H material should absorb ~4% more photons (above the band gap of the materials) than the planar devices. While this is a fairly modest improvement, it should be remembered first that this is only a secondary influence, as the main goal of this work is to test the possibility of improving efficiency though increased collection probability, rather than simply increased absorption, second, that this ~4% increase in absorbed photons is occurring despite a reduction in the amount of material by ~16%, and third, that if the collection improvement is indeed successful, devices could be made substantially thicker, further compounding these absorption increases.

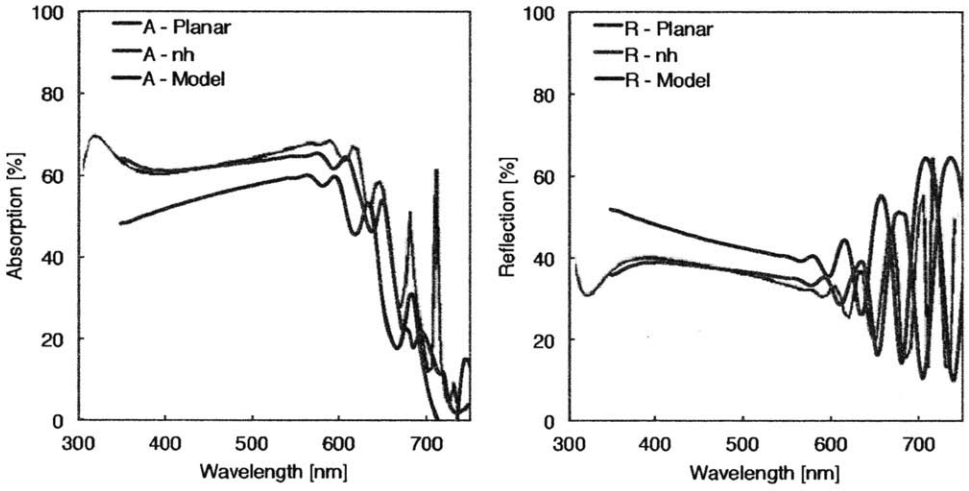

Figure 5-11: Simulated absorption and reflection (black) of bare nha-Si:H devices superimposed on experimental data. Simulation data courtesy of Jonathan Mailoa.

As an additional validation of our measurements, we have performed finite-difference time-domain (FDTD) simulations of the absorption and reflection of our nanohole devices, in order to ensure that the The results match surprisingly well, as shown in Fig. 5-11. We see very good agreement with the model, determined only from n and k values from separate planar a-Si:H films as well as the device geometries.

This indicates that we are indeed seeing the absorption improvements we expected from the geometries, and not due to increased impurities or other contamination.

5.4.2 Photovoltaic Conversion Efficiency Characterization

We begin the electrical characterization of our devices by performing current density-voltage (J-V) traces on cells illuminated under a simulated solar spectrum. A series of 16 samples were fabricated, consisting of 8 nanohole structured devices, and 8 planar devices, each pair was co-processed (all processes, *e.g.* depositions, cleanings, were done together) to eliminate any possible spurious influences improving or degrading any of the devices. All samples further contained 4 devices, in the layout depicted in Fig. 5-8. At least two devices per sample are measured, and all J-V data is averaged to produce the traces in Fig. 5-12.

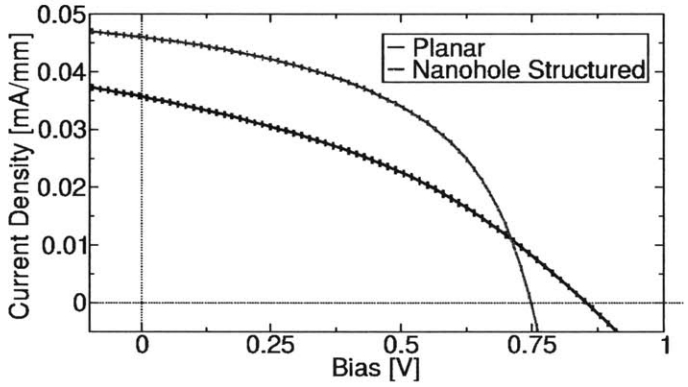

Figure 5-12: Averaged device current-voltage comparison, showing improvement in current density and fill factor of nha-Si:H devices over their planar equivalents.

From the traces in Fig. 5-12 we can see a few interesting features. First, there is a considerable increase in the short-circuit current density – we observe an average increase of 28.8% in the current output of the nanohole devices, relative to the planar average. We also see substantial increases in the fill factor of these devices – a 33.5% relative increase of the nha-Si:H devices over the planar counterparts. Unfortunately, the open-circuit voltage (V_{OC}) is observed to decrease from the planar to nanohole devices – the relative change is around a 12% drop on average. Despite this decrease

in V_{OC} we still observe a 55% relative improvement in the efficiency of the nha-Si:H devices over the planar equivalents. It is important to note, however, that these devices are of quite low efficiency still – the best cells tested showed only a 2.16% power conversion efficiency (PCE). We are currently working to establish a higher efficiency baseline (planar) device process to allow confirmation of these improvements for devices with more realistic industrial efficiencies.

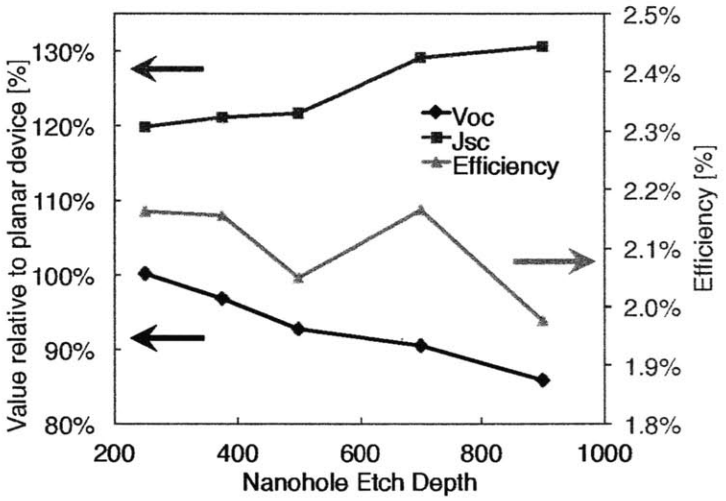

Figure 5-13: Relative performance of open-circuit voltage (V_{OC}), short-circuit current (J_{SC}) to the planar device configuration, and total cell efficiency as a function of the etch depth for nha-Si:H devices.

In order to investigate the observed decrease in open-circuit voltage, we fabricated a second series of samples, this time with varying depths of nanohole etching. Samples were tested as before, determining the efficiency, short-circuit current, and open-circuit voltage, now as a function of the nanohole depth. Results are shown in Fig. 5-13. We observe a quite linear decline in V_{OC} as the etch depth increases from ~250 nm to ~900 nm, and similarly see a slight increase in J_{SC} for the first three samples, followed by a much larger leap between ~500 nm and ~700 nm. This would fit with the theory that the majority of the transport improvement is occurring from extraction of carriers deeper in the material, as until the hole structures reach a reasonable depth, there are only slight increases in the extracted current, especially if we assume

the electric field gradient is strongest between the holes, as opposed to below them. Finally, we observe that the peak efficiency occurs at the point of this large boost in J_{SC}, as the current improvement outweighs the decline in voltage. It should also be noted that even at the lowest etch depth, we see substantial improvements in J_{SC} and efficiency of these nanostructured devices over the planar equivalents, although the V_{OC} is effectively identical for the lowest etch depth. This could be used to decouple the optical effects (increased absorption, especially preferentially at the surface) from the transport effects (improved extraction of holes excited deep in the device).

5.4.3 Effective Mobility Characterization

While we observe significant efficiency improvements in our nanohole-structured a-Si:H devices, there still remains some question as to the mechanisms permitting said improvement. It is plausible that there could be a modified drift field present, allowing holes to move toward the nanohole-filled contacts, as opposed to through the full device thickness, increasing the effective mobility through the full cell; but it also is possible that the modified absorption profile (slightly more absorption in a substantially smaller volume) is allowing the improvement of the transport to occur from band-tail state saturation, thereby increasing the average mobility of the holes moving through the device, or alternatively by simply causing a higher concentration of the absorbed photons and thus photoexcited carriers to exist closer to the surface of the cell, creating a shorter mean transit distance.

In order to test this final case, we perform time-of-flight mobility measurements (similar to those discussed in Chapter 3) on a pair of co-deposited devices, one structured with our nanohole architecture, and the other planar, to determine the effective mobility change of the nanohole structuring. It is important to note that this is indeed a measurement of effective mobility and not the true mobility directly, as we cannot immediately distinguish the first and second cases above – that is to say that from a standard ToF measurement alone, we cannot tell if a hole is appearing to transit the device more quickly due to drifting to the hole and being extracted in a shorter distance, or if the increased carrier density is causing the mean mobility of the

carriers to improve due to band-tail filling, and thus shortening transit times across a larger distance.

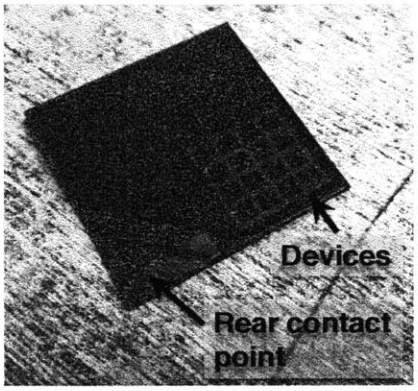

Figure 5-14: Time-of-flight nanohole structured test device, showing the grid array of 16 test devices, as well as the masked region allowing contact to the back of the device.

The samples were fabricated similar to those used for the UV-Vis absorption measurements, but with an additional deposition of indium tin oxide sputtered onto the quartz slides before the amorphous silicon deposition. This is necessary to make contact to the back of the device, and the transparent contact and substrate are necessary as we need to illuminate from the n-type side, while structuring the p-type side. Glass cover slips were used to mask all save the ALD deposition of AZO, which was etched away as described above to allow direct contact to the back TCO without shorting the devices. A sample device is shown in Fig. 5-14.

Unfortunately, the mobility measurements behaved quite anomalously for the planar devices, showing an increasing transit time with increasing applied bias on the devices, while the nanohole devices showed normal transit-voltage behavior. This could be due to improper isolation of the rear side contact from the front of the non-device regions providing unanticipated current pathways and thus preventing proper biasing of the actual test region. Despite this, we can still compare the nha-Si:H devices to those planar devices on silicon created for the study in Chapter 3. As we have found our depositions away from the mobility peak to be quite repeatable, we believe that this comparison is still appropriate.

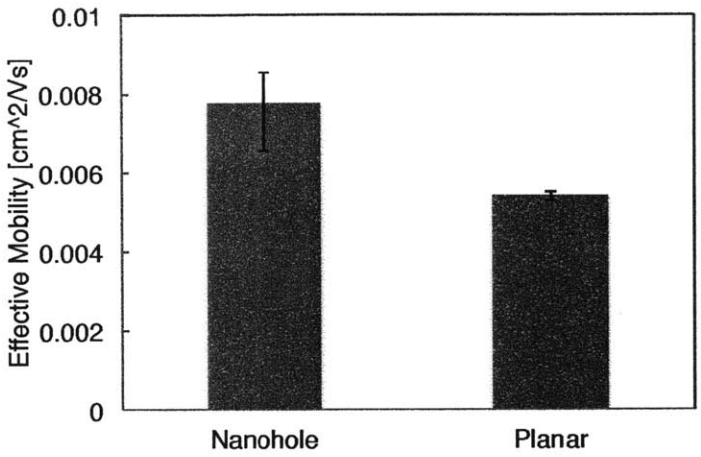

Figure 5-15: Time-of-flight determined hole mobilities for the nha-Si:H test device, compared to the planar device of similar deposition from Chapter 3. Error bars correspond to standard error of the mean.

As shown in Fig. 5-15, we see that while the uncertainty in the nanohole mobility measurement is quite large, the mobility still is significantly large than that of the similar planar device. While not entirely conclusive due to the uncertainty in the measurement, and the comparison between not entirely congruent devices, this measurement does suggest that the improved current collection mechanism is indeed resulting in an increased effective mobility, as opposed to purely increased preferential surface absorption. Furthermore, we see little to no change in the mobility of devices as a function of moderate changes in the fluence of the laser, also suggesting that we are seeing preferential extraction toward the nanohole regions, as opposed to simply an increased current density saturating valence band-tail states. This could be further confirmed through measurements varying the applied simulated solar illumination (testing under 0.5, 1, and 1.5 suns, for example) but this is not possible in the test equipment available at this time. We note that the current improvement of the low etch depth devices shown in Fig. 5-13 suggest we are seeing some additional enhancement from surface absorption, whereas the improvement due to the nanohole collection likely begins to dominate around the 750 nm depth region. The

optimization of these two effects should allow for maximization of future nha-Si:H device performance.

5.5 Heterojunction nha-Si:H devices

We are currently working to test the potential of other architectures of nha-Si:H devices. Specifically, we are investigating those similar to Design 2 in Fig. 5-2, using poly(3,4-ethylenedioxythiophene) polystyrene sulfonate (PEDOT:PSS), a high hole mobility polymer, as both the *p*-type material and transparent front contact for the devices. The main challenge insofar has been achieving good filling of the nanohole structures with the PEDOT:PSS solutions, and maintaining high content levels after annealing away the solvents used for the deposition of the polymers. Previous studies have successfully utilized PEDOT:PSS as the p-type contact in structured crystalline silicon photovoltaic devices [99, 92] with efficiencies up to 11% [89], indicating that the approach may be quite promising if the issues of filling the nanoholes can be overcome.

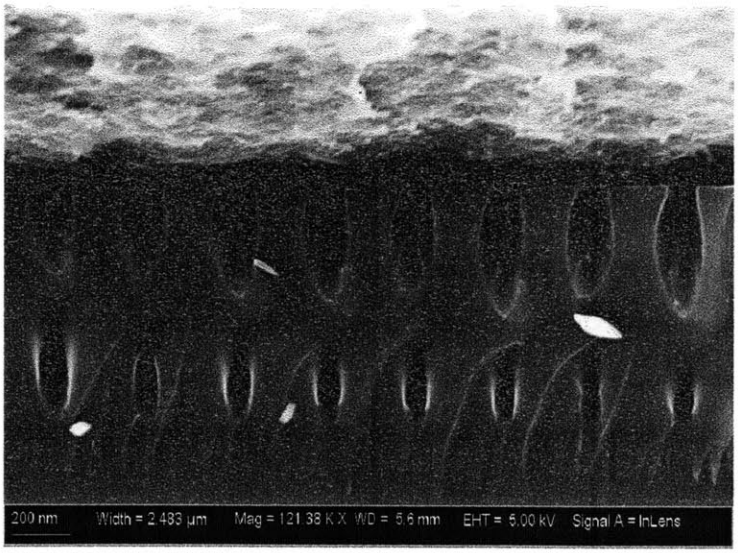

Figure 5-16: Preliminary results filling PEDOT:PSS polymers into nanohole structures to act as both the p-type material and transparent front contact for heterjunction nha-Si:H devices.

Preliminary results filling PEDOT:PSS in nanohole structures are shown in Fig. 5-16, as well as Fig. A-5. While full devices could not be completed as of this writing, the increased mobility, especially compared to the heavily doped p-type a-Si:H material used previously could allow for improvements in the efficiencies of these devices beyond those explored in the homojunction configuration previously.

5.6 Conclusions

In this chapter we discussed the motivations, simulation, fabrication and characterization of homojunction nha-Si:H devices We show both improved light absorption (a ~4% improvement) and improved current collection (a ~28.8% improvement) in our structured devices, resulting in a ~55% improvement in device efficiency, while using almost entirely scalable methods. Interference lithography allows near-instantaneous patterning of up to 1" square devices in a laboratory setting, and with a rastering Lloyd's mirror setup, full wafers or even roll processes could be feasible. ALD depositions could be replaced by more rapid pulsed CVD methods, or by solution deposition of TCO nanoparticles, or carbon-based conducting structures (nanotubes, or graphene nanoplates), or the alternative heterojunction structures (such as PEDOT:PSS as discussed above), to improve the scalability of this step. We are currently pursuing improving the efficiency of our baseline processes to validate these results for higher efficiency a-Si:H materials, as well as exploring the alternate filling materials mentioned herein.

Finally, we are currently pursuing full device modeling of nha-Si:H device to both clarify the underlying mechanisms of the improved current observed in our devices (determining if it is indeed a preferential extraction mechanism drawing charge carriers toward the nanohole structures) as well as to allow the rapid optimization of our nanohole structure architectures.

Chapter 6

Conclusions

6.1 Summary

In this work we have discussed some of the key topics related to understanding and improving hole transport in hydrogenated amorphous silicon.

In Chapter 1, we briefly introduced the case for photovoltaic energy, as well as for the continued study of hydrogenated amorphous silicon as a photovoltaic material. We discussed the advantages and disadvantages of the material, and walked through models elucidating the importance of improving hole mobility to increase photovoltaic device performance, motivating the coming chapters.

In Chapter 2, we began our exploration of the origins of hole trapping in a-Si:H. We discussed our creation and vetting of a large set of computational a-Si:H geometries, and through a statistical analysis of the influence of various structural phenomena on hole trap depths, discovered that metastable defects arising from displacement of silicon atoms under proximity to the localized hole wavefunction correlated most strongly with hole trapping in our ensemble. We also showed that while floating bonds correlated fairly strongly with hope trapping as well, dangling bonds show a statistically insignificant correlation with trap formation. Finally, we offered the explanation that these structural rearrangements are allowing for a slight delocalization of the hole wavefunction around the defective region, decreasing the kinetic energy

penalty to over-confinement of the hole, and thereby increasing the strength of the trapping.

In Chapter 3 we outlined our process of creating experimental a-Si:H samples for mobility measurements, as well as the theory and experimental setup needed to perform time-of-flight transient photocurrent measurements to obtain the hole mobilities of our samples. We discussed and presented measurements of stress and mobility of our samples as well, and used these to put in context the measurements of the hole transport in our devices.

In Chapter 4 we extended the computational study from Chapter 2 to include variations in both the stress and hydrogen content of the structures. This allowed us to investigate the correlations between these structural properties and the shifting regimes of defects present in the ensembles. We showed that increasing hydrogen content correlated with increasing prevalence of floating bonds, that limiting stress correlated with an increase in ionization displacement defects, and that tensile stress increased hole trapping through lattice expansion promoting hole delocalization. Using these theories we were able to set forward an atomic-level explanation for the observed mobility trends in Chapter 3. Finally, by decoupling the stress and hydrogen content by manipulating the stress of previously deposited films, we were able to show that, as anticipated by our calculations, increasing hydrogen content at a given stress state indeed correlated with lower mobilities, likely due to an increase in floating bond density.

In Chapter 5 we discussed the motivation for using nanohole structuring of a-Si:H devices to improve hole extraction from the material. We walked through our method of fabricating nha-Si:H materials using interference lithography and reactive ion etching to create arrays of 150 nm holes at 300 nm pitches. We discussed different geometries possible for nanohole devices, and explored one of these, creating filled devices using a semi-conformal PECVD p-type a-Si:H layer and a ALD AZO transparent front contact and anti-reflection coating. We characterized these devices, demonstrating a 55% increase in current in our low-efficiency proof of concept cells.

Finally, in Chapter 6, we summarized our work in the form you are currently reading, and set forward the future work you are about to see!

6.2 Ongoing Work

The bulk of the outstanding work rests in the improvement of hole extraction in amorphous silicon photovoltaics. We are currently working to improve our device efficiencies in order to determine how far our homojunction nanohole structured architecture can take us. We hope to see similar improvements with high efficiency (~8%) base planar a-Si:H devices, but expect the improvements to be mitigated in more efficient cells.

Additionally we are still exploring the potential for other architectures to further improve the performance of our devices, focusing most strongly on the inclusion of conductive polymers like PEDOT:PSS (see Fig. A-5) in our material. We are also however exploring other materials such as electrodeposited Cu_2O (see Fig. A-6), as well as high mobility quantum dot films (see Fig. A-7), with some success in the filling of each. There is still much work work to be done however on the completion of these devices, as well as their testing, characterization, and analysis.

6.3 Future Outlook

Despite the complexity of the structures controlling the mobility in a-Si:H, as discussed in Chapter 4, we believe the determined atomic structural trends in this work could offer some insight into future improvements of the base material.

The three main structural forces we observe computationally to exacerbate hole trapping (floating bonds, ionization displacement defects, and lattice expansion allowing for hole delocalization) all correlate to different material features. Specifically, we observe that floating bonds can be limited by a decrease in the relative density of silicon bonds, as seen in the movement toward tensile stress, and through the reduction in hydrogen contents; the prevalence of ionization displacement defects is limited

by the introduction of biaxial stress, causing the displacement of atomic structures to be energetically more expensive; and localization is limited by a lack of lattice expansion preventing the decrease in kinetic energy penalties associated with hole wavefunction delocalization.

Thus, a method allowing the reduction of bond density, while also preventing lattice expansion and atomic displacement could hypothetically avoid all of these issues. Introduction of large interstitial atoms or small crystallites of a non-electrically-active species could be one method of achieving this. Similarly, the application of structured crystalline domains could also achieve these requirements by constraining the lattice further to prevent displacements, while avoiding the compression resulting in increased floating bond density or expansion correlated with hole delocalization. Alternatively, if it were possible to specifically target regions of a specific defect using some energy-injection mechanism (e.g. a specific vibrational frequency correlated with a given defect) it could be possible to "burn out" the targeted defects through local restructuring of the offending atoms, thereby improving the material in a similar manner to what our conditional ensembles are doing computationally. While the specific exploration of these concepts is outside the scope of this work, we hope this prospectus could seed future work into the improvement of a-Si:H materials.

We also note that while the work herein focuses on purely amorphous silicon materials, some of these concepts have already been extended to micro-/nanocrystalline silicon (*nc*-Si:H) computationally, available in Ref. [84]. This work provides a further step of abstraction toward the analysis of hole trapping structures, using machine learning methods to determine specific functions most highly correlated with hole traps in materials. Further extension of this study of *nc*-Si:H to both varied microstructure, as performed here for a-Si:H in Chapter 4, as well as to experimental *nc*-Si:H samples, as in Chapter 3 here, could provide valuable insights into this related material.

6.4 Closing Remarks

While the work presented herein has been largely specific to hydrogenated amorphous silicon, we hope that the methods, procedures and techniques discussed in this thesis can be of wider application, and provide a framework for the future study of other new amorphous semiconducting materials. In particular, we call attention to the need for, and application of ensemble-based analysis, the use of statistics for determining structural correlations, the allowance for atomic reconfiguration in the charged state of structures, and the necessity of examining a wide array of structural phenomena in order to determine the most applicable correlations.

I would also like to close by once again thanking all of the people mentioned in the beginning acknowledgments section – without all of their assistance none of this work would have been possible. And finally, thank you for your interest in reading this document!

Appendix A

Additional Images of nha-Si Creation Process

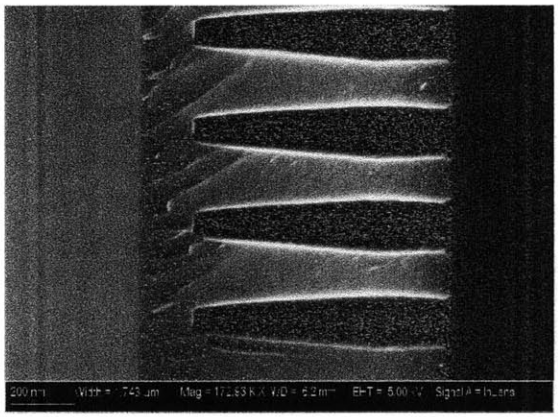

Figure A-1: Example cross-sectional SEM image of etched nanohole structures after BOE cleaning.

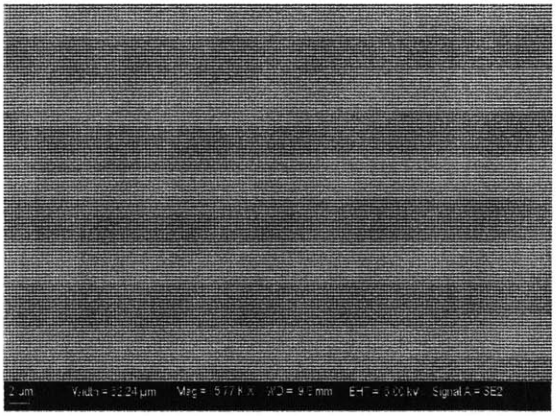

Figure A-2: Lower magnification top view of nha-Si:H structure showing extreme regularity of the nanohole pattern.

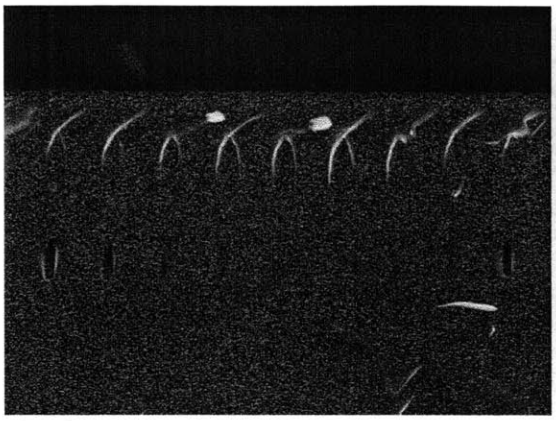

Figure A-3: Example cross-sectional SEM image of the test used to determine PECVD a-Si:H deposition conformality. The lighter layer on top of the nanohole structure corresponds to the test p-type deposition material.

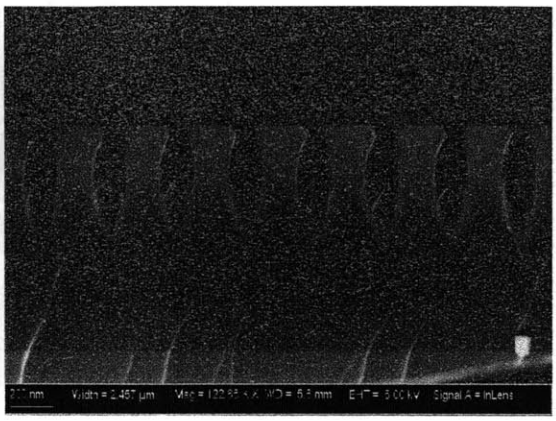

Figure A-5: Preliminary results in filling nanoholes with PEDOT:PSS for heterojunction solar cells.

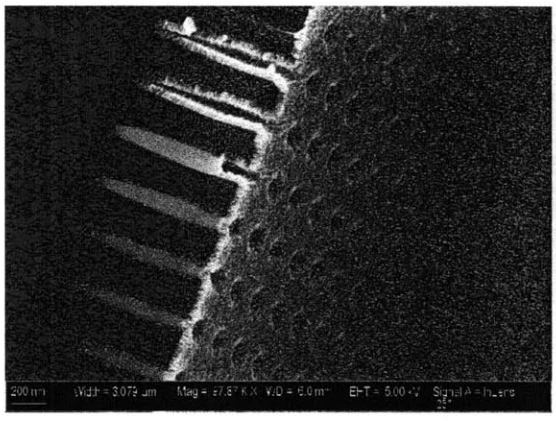

Figure A-4: Isometric view of ALD AZO coating for nha-Si:H devices.

Figure A-6: Preliminary results in filling nanoholes via electrodeposition of Cu_2O for heterojunction solar cells. Thanks to Yun Lee and Riley Brandt for assistance with Cu_2O electrodeposition.

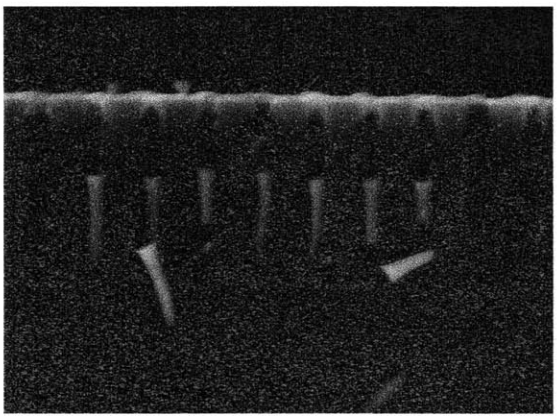

Figure A-7: Preliminary results in filling nanoholes with high mobility quantum dot films for heterojunction solar cells. Thanks to Jennifer Scherer for help with the quantum dot deposition.

Appendix B

SIESTA Input Files

This appendix includes the flexible data format (FDF) input file used to relax the charged and uncharged samples of any stress state in SIESTA.

The comments in the file indicate the positions where modifications are made for differing hydrogen contents, stresses and charges.

B.1 Sample FDF Input Configuration

```
SystemLabel         a-SiHsample
NumberOfAtoms       236     #For 10% hydrogen ensemble
SpinPolarized       .true.
NumberOfSpecies     2
SaveRho
XC.functional       GGA
XC.authors          PBE
PAO.BasisSize       DZP
PAO.EnergyShift     300 meV
%block ChemicalSpeciesLabel
   1  14  Si
   2   1  H
%endblock ChemicalSpeciesLabel
DirectPhi           .true.
%block ProjectedDensityOfStates
   -10.00  5.00  0.200  800  eV
```

```
%endblock ProjectedDensityOfStates
MeshCutoff         100.0 Ry
MaxSCFIterations   100
DM.MixingWeight    0.1
DM.NumberPulay     3
NetCharge 0                #Set to "1" for charged system
SolutionMethod     diagon
ElectronicTemperature  25 meV
MD.UseStructFile .true.
MD.TypeOfRun       CG
MD.VariableCell        .true.
MD.TargetPressure 0 GPa    #Set to stress level
%block  MD.TargetStress    #Only used for stressed calculations
   1.0    1.0    0.0    0.0    0.0    0.0
%endblock  MD.TargetStress
WriteMDXmol .true.
WriteCoorXmol .true.
WriteKpoints .true.
MD.NumCGsteps 500
LongOutput .true.
AtomicCoordinatesFormat  Ang
```

Bibliography

[1] U.S. Energy Information Administration, "International Energy Outlook 2013," tech. rep., 2013.

[2] R. T. Pierrehumbert, "Short-Lived Climate Pollution," *Annual Review of Earth and Planetary Sciences*, vol. 42, pp. 341–379, May 2014.

[3] S. Shafiee and E. Topal, "When will fossil fuel reserves be diminished?," *Energy Policy*, vol. 37, pp. 181–189, Jan. 2009.

[4] Greenpeace and European Photovoltaic Industry, "Solar Generation 6: Solar photovoltaic electricity empowering the world," 2011.

[5] D. Powell, M. Winkler, H. Choi, C. Simmons, D. Needleman, and T. Buonassisi, "Crystalline silicon photovoltaics: a cost analysis framework for determining technology pathways to reach baseload electricity costs," *Energy Environ. Sci.*, vol. 5, pp. 5874–5883, 2012.

[6] National Science Board, *Science and Engineering Indicators 2012.* 2012.

[7] M. A. Green, K. Emery, Y. Hishikawa, W. Warta, and E. D. Dunlop, "Solar cell efficiency tables (version 43)," *Progress in Photovoltaics: Research and Applications*, vol. 22, no. 1, pp. 1–9, 2014.

[8] R. E. Schropp and M. Zeman, *Amorphous and Microcrystalline Silicon Solar Cells: Modeling, Materials and Device Technology.* Boston: Kluwer Academic Publishers, 1998.

[9] A. Gallagher, "Neutral radical deposition from silane discharges," *Journal of Applied Physics*, vol. 63, no. 7, pp. 2406–2413, 1988.

[10] E. Johlin, N. Tabet, S. Castro-Galnares, A. Abdallah, M. I. Bertoni, T. Asafa, J. C. Grossman, S. Said, and T. Buonassisi, "Structural origins of intrinsic stress in amorphous silicon thin films," *Physical Review B*, vol. 85, p. 075202, 2012.

[11] M. A. Green and M. J. Keevers, "Optical Properties of Intrinsic Silicon at 300 K," *Progress in Photovoltaics: Research and Applications*, vol. 3, no. 3, pp. 189–192, 1995.

[12] M. A. Green, "Limiting photovoltaic ef fi ciency under new ASTM International G173-based reference spectra," *Progress in Photovoltaics: Research and Applications*, vol. 20, no. 8, pp. 954–959, 2012.

[13] S. Kim, J.-W. Chung, H. Lee, J. Park, Y. Heo, and H.-M. Lee, "Remarkable progress in thin-film silicon solar cells using high-efficiency triple-junction technology," *Solar Energy Materials and Solar Cells*, vol. 119, pp. 26–35, Dec. 2013.

[14] E. A. Schiff, "Low-mobility solar cells: a device physics primer with application to amorphous silicon," *Solar Energy Materials and Solar Cells*, vol. 78, pp. 567–595, July 2003.

[15] D. Staebler and C. Wronski, "Reversible conductivity changes in discharge-produced amorphous Si," *Applied Physics Letters*, vol. 31, no. 4, p. 292, 1977.

[16] R. A. Street, *Hydrogenated Amorphous Silicon*. Cambridge: Cambridge University Press, 1991.

[17] E. A. Schiff, "Hole mobilities and the physics of amorphous silicon solar cells," *Journal of Non-Crystalline Solids*, vol. 352, pp. 1087–1092, June 2006.

[18] H. Fritzsche, "Development in Understanding and Controlling the Staebler-Wronski Effect in a-Si:H," *Annual Review of Materials Research*, vol. 31, pp. 47–79, 2001.

[19] J. Shirafuji, M. Kuwagaki, T. Sato, and Y. Inuishi, "Effect of Substrate Temperature on Properties of Glow-Discharged Hydrogenated Amorphous Silicon," *Japanese Journal of Applied Physics*, vol. 23, pp. 1278–1286, Oct. 1984.

[20] J. Shirafuji, K. Shirakawa, and S. Nagata, "Dangling Bond Creation in Hydrogenated Amorphous Silicon by Light-Soaking," *Japanese Journal of Applied Physics*, vol. 25, pp. L634–L636, Aug. 1986.

[21] D. K. Biegelsen and M. Stutzmann, "Hyperfine studies of dangling bonds in amorphous silicon," *Physical Review B*, vol. 33, no. 5, p. 3006, 1986.

[22] M. Stutzmann and D. K. Biegelsen, "Dangling or Floating Bonds in Amorphous Silicon?," *Physical Review Letters*, vol. 60, no. 16, pp. 1682–1682, 1988.

[23] M. Stutzmann, "The defect density in amorphous silicon," *Philosophical Magazine B*, vol. 60, p. 531, 1989.

[24] Y. Bar-Yam and J. D. Joannopoulos, "Dangling Bond in a-Si:H," *Physical Review Letters*, vol. 56, no. 20, pp. 2203–2206, 1986.

[25] H. M. Branz and E. A. Schiff, "Dangling-bond relaxation and deep-level measurements in hydrogenated amorphous silicon," *Physical Review B*, vol. 48, no. 12, p. 8667, 1993.

[26] Z. E. Smith and S. Wagner, "Band Tails, Entropy, and Equilibrium Defects in Hydrogenated Amorphous Silicon," *Physical Review Letters*, vol. 59, no. 6, p. 688, 1987.

[27] R. A. Street, J. Kakalios, and T. M. Hayes, "Thermal equilibration in doped amorphous silicon," *Physical Review B*, vol. 34, no. 4, pp. 3030–3033, 1986.

[28] S. Pantelides, "Gap states in amorphous silicon-dangling and floating bonds," *Journal of Non-Crystalline Solids*, vol. 97, pp. 79–82, 1987.

[29] S. Pantelides, "Pantelides Replies," *Physical Review Letters*, vol. 60, no. 16, p. 1683, 1988.

[30] S. T. Pantelides, "Defects in Amorphous Silicon: A New Perspective," *Physical Review Letters*, vol. 57, no. 23, pp. 2979–2982, 1986.

[31] J. H. Stathis and S. T. Pantelides, "Quantitative analysis of EPR and electron-nuclear double resonance spectra of D centers in amorphous silicon: Dangling versus floating bonds," *Physical Review B*, vol. 37, no. 11, p. 6579, 1988.

[32] J. H. Stathis, "Analysis of the superhyperfine structure and the g tensor of defects in amorphous silicon," *Physical Review B*, vol. 40, no. 2, p. 1232, 1989.

[33] J. Liang, E. A. Schiff, S. Guha, B. Yan, and J. Yang, "Hole-mobility limit of amorphous silicon solar cells," *Applied Physics Letters*, vol. 88, no. 6, p. 063512, 2006.

[34] Q. Wang, H. Antoniadis, and E. A. Schiff, "Electron drift mobility measurements on annealed and light-soaked hydrogenated amorphous silicon," *Applied Physics Letters*, vol. 60, no. 22, p. 2791, 1992.

[35] J. Dong and D. A. Drabold, "Atomistic Structure of Band-Tail States in Amorphous Silicon," *Physical Review Letters*, vol. 80, pp. 1928–1931, Mar. 1998.

[36] D. A. Drabold, "Silicon: the gulf between crystalline and amorphous," *Physica Status Solidi (RRL) - Rapid Research Letters*, vol. 5, pp. 359–360, Nov. 2011.

[37] P. Khomyakov, W. Andreoni, N. Afify, and A. Curioni, "Large-Scale Simulations of a-Si:H: The Origin of Midgap States Revisited," *Physical Review Letters*, vol. 107, p. 255502, Dec. 2011.

[38] Y. Pan, F. Inam, M. Zhang, and D. A. Drabold, "Atomistic origin of Urbach tails in amorphous silicon," *Physical Review Letters*, vol. 100, no. 20, p. 206403, 2008.

[39] L. Wagner and J. Grossman, "Microscopic Description of Light Induced Defects in Amorphous Silicon Solar Cells," *Physical Review Letters*, vol. 101, no. 26, p. 265501, 2008.

[40] R. Biswas, Q. Li, Y. Yoon, and H. M. Branz, "Dangling-bond levels and structure relaxation in hydrogenated amorphous silicon," *Physical Review B*, vol. 56, no. 15, pp. 9197–9200, 1997.

[41] H. M. Branz, "Hydrogen collision model: Quantitative description of metastability in amorphous silicon," *Physical Review B*, vol. 59, no. 8, pp. 5498–5512, 1999.

[42] H. M. Branz, S. Asher, H. Gleskova, and S. Wagner, "Light-induced D diffusion measurements in hydrogenated amorphous silicon : Testing H metastability models," *Physical Review B*, vol. 59, no. 8, p. 5513, 1999.

[43] S. Zafar and E. A. Schiff, "Hydrogen and Defects in Amorphous Silicon," *Physical Review Letters*, vol. 66, no. 11, pp. 1493–1496, 1991.

[44] J. Melskens, A. H. Smets, M. Schouten, S. W. Eijt, H. Schut, and M. Zeman, "The Relation Between Vacancies and the Dominant Defects in Hydrogenated Amorphous Silicon," in *2012 38th IEEE Photovoltaic Specialists Conference*, 2012.

[45] A. Mahan, J. Carapella, B. Nelson, R. Crandall, and I. Balberg, "Deposition of device quality, low H content amorphous silicon," *Journal of Applied Physics*, vol. 69, no. 9, pp. 6728–6730, 1991.

[46] F. Wooten, K. Winer, and D. Weaire, "Computer generation of structural models of amorphous Si and Ge," *Physical Review Letters*, vol. 54, no. 13, pp. 1392–1395, 1985.

[47] P. Keating, "Relationship between the Macroscopic and Microscopic Theory of Crystal Elasticity. I. Primitive Crystals," *Physical Review*, vol. 152, no. 2, p. 774, 1966.

[48] J. M. Soler, E. Artacho, J. D. Gale, A. Garcia, J. Junquera, P. Ordejón, and D. Sánchez-Portal, "The SIESTA method for ab initio order-N materials simulation," *Journal of Physics: Condensed Matter*, vol. 14, p. 2745, 2002.

[49] J. Perdew, K. Burke, and M. Ernzerhof, "Generalized Gradient Approximation Made Simple.," *Physical review letters*, vol. 77, pp. 3865–3868, Oct. 1996.

[50] D. E. Carlson and K. Rajan, "The reversal of light-induced degradation in amorphous silicon solar cells by an electric field," *Applied Physics Letters*, vol. 70, no. 16, p. 2168, 1997.

[51] S. E. Taylor and F. Bruneval, "Understanding and correcting the spurious interactions in charged supercells," *Physical Review B*, vol. 84, p. 075155, Aug. 2011.

[52] H. Ohsaki and Y. Tatsumi, "8.1 Density of a-Si, a-SiNx, a-SiC and a-SiGe," in *Properties of Amorphous Silicon and its Alloys* (T. Searle, ed.), ch. 8, pp. 347–371, Institution of Engineering and Technology, 1998.

[53] K. Laaziri, S. Kycia, S. Roorda, M. Chicoine, J. Robertson, J. Wang, and S. Moss, "High Resolution Radial Distribution Function of Pure Amorphous Silicon," *Physical Review Letters*, vol. 82, no. 17, pp. 3460–3463, 1999.

[54] R. Bellisent, A. Menelle, W. Howells, A. C. Wright, T. Brunier, R. Sinclair, and F. Jansen, "The structure of amorphous Si:H using steady state and pulsed neutron sources," *Physica B: Condensed Matter*, vol. 156-157, pp. 217–219, Jan. 1989.

[55] D. A. Drabold, Y. Li, B. Cai, and M. Zhang, "Urbach tails of amorphous silicon," *Physical Review B*, vol. 83, p. 045201, Jan. 2011.

[56] F. Kail, J. Farjas, P. Roura, C. Secouard, O. Nos, J. Bertomeu, and P. R. I. Cabarrocas, "The configurational energy gap between amorphous and crystalline silicon," *physica status solidi (RRL) - Rapid Research Letters*, vol. 5, pp. 361–363, Nov. 2011.

[57] E. Parzen, "On Estimation of a Probability Density Function and Mode," *The Annals of Mathematical Statistics*, vol. 33, no. 3, pp. 1065–1076, 1962.

[58] M. Rosenblatt, "Remarks on Some Nonparametric Estimates of a Density Function," *The Annals of Mathematical Statistics*, vol. 27, no. 3, pp. 832–837, 1956.

[59] R. Resta and S. Sorella, "Electron Localization in the Insulating State," *Physical Review Letters*, vol. 82, no. 2, p. 370, 1999.

[60] P. L. Silvestrelli, "Maximally localized Wannier functions for simulations with supercells of general symmetry," *Physical Review B*, vol. 59, pp. 9703–9706, Apr. 1999.

[61] H. Gleskova, P. Hsu, Z. Xi, J. Sturm, Z. Suo, and S. Wagner, "Field-effect mobility of amorphous silicon thin-film transistors under strain," *Journal of Non-Crystalline Solids*, vol. 338-340, pp. 732–735, June 2004.

[62] H. Gleskova and S. Wagner, "Electrical response to uniaxial tensile strain of a-Si:H TFTs fabricated on polyimide foils," *Journal of Non-Crystalline Solids*, vol. 354, pp. 2627–2631, May 2008.

[63] R. Koenenkamp and T. Shimada, "Electron and hole transport in amorphous silicon solar cells," *Applied Physics Communications*, vol. 12, no. 1, pp. 11–44, 1993.

[64] W. E. Spear, "The study of transport and realted properties of amorphous silicon by transient experiments," *Journal of Non-Crystalline Solids*, vol. 60, pp. 1–14, 1983.

[65] T. Tiedje, C. R. Wronski, B. Abeles, and J. M. Cebulka, "Electron transport in hydrogenated amorphous silicon: drift mobility and junction capacitance," *Solar Cells*, vol. 2, no. 3, pp. 301–318, 1980.

[66] G. Ganguly, I. Sakata, and A. Matsuda, "Time of flight mobility measurements in a-Si: H grown under controlled-energy ion-bombardment," *Journal of Non-Crystalline Solids*, vol. 198, pp. 300–303, 1996.

[67] P. Roca i Cabarrocas, P. Morin, V. Chu, J. P. Conde, J. Z. Liu, H. R. Park, and S. Wagner, "Optoelectronic properties of hydrogenated amorphous silicon films deposited under negative substrate bias," *Journal of Applied Physics*, vol. 69, no. 5, p. 2942, 1991.

[68] M. Brinza and G. J. Adriaenssens, "The time-of-flight photocurrent analysis revisited," *Journal of Optoelectronics and Advanced Materials*, vol. 8, no. 6, pp. 2028–2034, 2006.

[69] R. P. Barclay, G. Seynhaeve, G. J. Adriaenssens, and J. M. Marshall, "Investigation of Time of Flight Photocurrents in a-Si:H," in *MRS Proceedings*, vol. 118, pp. 519–524, Jan. 1988.

[70] E. A. Schiff, "Transit-time measurements of charge carriers in disordered silicons: Amorphous, microcrystalline and porous," *Philosophical Magazine*, vol. 89, pp. 2505–2518, Oct. 2009.

[71] C. Main, R. Brüggemann, D. P. Webb, and S. Reynolds, "Determination of gap-state distributions in amorphous semiconductors from transient photocurrents using a fourier transform technique," *Solid State Communications*, vol. 83, pp. 401–405, Aug. 1992.

[72] A. A. Langford, M. L. Fleet, B. P. Nelson, W. A. Lanford, and N. Maley, "Infrared absorption strength and hydrogen content of hydrogenated amorphous silicon," *Physical Review B*, vol. 45, p. 13367, 1992.

[73] L. B. Freund and S. Suresh, *Thin Film Materials: Stress, Defect Formation and Surface Evolution*. Cambridge, U.K.: Cambridge University Press, 2004.

[74] R. B. Wehrspohn, S. C. Deane, I. D. French, I. Gale, J. Hewett, M. J. Powell, and J. Robertson, "Relative importance of the Si âĂŞ Si bond and Si âĂŞ H bond for the stability of amorphous silicon thin film transistors," *Journal of Applied Physics*, vol. 87, no. 1, pp. 144–154, 2000.

[75] B. A. Korevaar, G. J. Adriaenssens, A. H. M. Smets, W. M. M. Kessels, H. Z. Song, M. C. M. van de Sanden, and D. C. Schram, "High hole drift mobility in a-Si:H deposited at high growth rates for solar cell application," *Journal of Non-Crystalline Solids*, vol. 266-269, pp. 380–384, May 2000.

[76] M. Fehr, A. Schnegg, B. Rech, O. Astakhov, F. Finger, R. Bittl, C. Teutloff, and K. Lips, "Metastable Defect Formation at Microvoids Identified as a Source of Light-Induced Degradation in aâĹŠSi:H," *Physical Review Letters*, vol. 112, p. 066403, Feb. 2014.

[77] J. Melskens, A. H. M. Smets, M. Schouten, S. W. H. Eijt, H. Schut, and M. Zeman, "New Insights in the Nanostructure and Defect States of Hydrogenated Amorphous Silicon Obtained by Annealing," *IEEE Journal of Photovoltaics*, vol. 3, pp. 65–71, Jan. 2013.

[78] H. M. Branz, "Hydrogen diffusion and mobile hydrogen in amorphous silicon," *Physical Review B*, vol. 60, no. 11, pp. 7725–7727, 1999.

[79] E. Johlin, L. K. Wagner, T. Buonassisi, and J. C. Grossman, "Origins of Structural Hole Traps in Hydrogenated Amorphous Silicon," *Physical Review Letters*, vol. 110, p. 146805, Apr. 2013.

[80] G. Ganguly and A. Matsuda, "Control of the Electron and Hole Drift mobilities in Plasma Deposited a-Si:H," *Materials Research Society Symposium Proceedings*, vol. 336, pp. 7–18, Feb. 1994.

[81] J. M. Marshall, "Carrier diffusion in amorphous semiconductors," *Reports on Progress in Physics*, vol. 46, p. 1235, 1983.

[82] S. Reynolds, "Carrier mobility and density of states in microcrystalline silicon film compositions, probed using time-of-flight photocurrent spectroscopy," *Journal of Optoelectronics and Advanced Materials*, vol. 11, no. 9, pp. 1086–1092, 2009.

[83] G. Pfanner, C. Freysoldt, J. Neugebauer, F. Inam, D. Drabold, K. Jarolimek, and M. Zeman, "Dangling-bond defect in a-Si:H: Characterization of network and strain effects by first-principles calculation of the EPR parameters," *Physical Review B*, vol. 87, p. 125308, Mar. 2013.

[84] T. Mueller, E. Johlin, and J. C. Grossman, "Origins of hole traps in hydrogenated nanocrystalline and amorphous silicon revealed through machine learning," *Physical Review B*, vol. 89, p. 115202, 2014.

[85] P.-C. Kuo, A. Jamshidi-Roudbari, and M. Hatalis, "Effect of mechanical strain on mobility of polycrystalline silicon thin-film transistors fabricated on stainless steel foil," *Applied Physics Letters*, vol. 91, no. 24, p. 243507, 2007.

[86] M. Legesse, M. Nolan, and G. Fagas, "A first principles analysis of the effect of hydrogen concentration in hydrogenated amorphous silicon on the formation of strained Si-Si bonds and the optical and mobility gaps," *Journal of Applied Physics*, vol. 115, p. 203711, May 2014.

[87] J. M. Marshall, R. A. Street, M. J. Thompson, and W. B. Jackson, "The energy distribution of localised states, and the mobilities of free carriers in a-Si:H, from time of flight and other measurements," *Journal of Non-Crystalline Solids*, vol. 97-98, pp. 563–566, Dec. 1987.

[88] Q. G. Du, C. H. Kam, H. V. Demir, H. Y. Yu, and X. W. Sun, "Enhanced optical absorption in nanopatterned silicon thin films with a nano-cone-hole structure for photovoltaic applications.," *Optics letters*, vol. 36, pp. 1713–5, May 2011.

[89] S. Jeong, E. C. Garnett, S. Wang, Z. Yu, S. Fan, M. L. Brongersma, M. D. McGehee, and Y. Cui, "Hybrid silicon nanocone-polymer solar cells.," *Nano letters*, vol. 12, pp. 2971–6, June 2012.

[90] J. Zhu, Z. Yu, G. F. Burkhard, C.-M. Hsu, S. T. Connor, Y. Xu, Q. Wang, M. McGehee, S. Fan, and Y. Cui, "Optical absorption enhancement in amorphous silicon nanowire and nanocone arrays.," *Nano letters*, vol. 9, pp. 279–82, Jan. 2009.

[91] K.-Q. Peng, X. Wang, L. Li, X.-L. Wu, and S.-T. Lee, "High-performance silicon nanohole solar cells.," *Journal of the American Chemical Society*, vol. 132, pp. 6872–3, May 2010.

[92] L. Hong, X. Wang, H. Zheng, L. He, H. Wang, and H. Yu, "High efficiency silicon nanohole/organic heterojunction hybrid solar cell," *Applied Physics Letters*, vol. 104, p. 053104, Feb. 2014.

[93] C.-M. Hsu, C. Battaglia, C. Pahud, Z. Ruan, F.-J. Haug, S. Fan, C. Ballif, and Y. Cui, "High-Efficiency Amorphous Silicon Solar Cell on a Periodic Nanocone Back Reflector," *Advanced Energy Materials*, vol. 2, pp. 628–633, June 2012.

[94] R. Biswas, J. Bhattacharya, B. Lewis, N. Chakravarty, and V. Dalal, "Enhanced nanocrystalline silicon solar cell with a photonic crystal back-reflector," *Solar Energy Materials and Solar Cells*, vol. 94, pp. 2337–2342, Dec. 2010.

[95] D. Derkacs, S. H. Lim, P. Matheu, W. Mar, and E. T. Yu, "Improved performance of amorphous silicon solar cells via scattering from surface plasmon polaritons in nearby metallic nanoparticles," *Applied Physics Letters*, vol. 89, no. 9, p. 093103, 2006.

[96] Y. a. Akimov, W. S. Koh, and K. Ostrikov, "Enhancement of optical absorption in thin-film solar cells through the excitation of higher-order nanoparticle plasmon modes.," *Optics express*, vol. 17, pp. 10195–205, June 2009.

[97] X. Meng, V. Depauw, G. Gomard, O. El Daif, C. Trompoukis, E. Drouard, C. Jamois, A. Fave, F. Dross, I. Gordon, and C. Seassal, "Design, fabrication and optical characterization of photonic crystal assisted thin film monocrystalline-silicon solar cells.," *Optics express*, vol. 20 Suppl 4, pp. A465–75, July 2012.

[98] N. Nguyen-Huu, M. Cada, and J. Pištora, "Imperfectly geometric shapes of nanograting structures as solar absorbers with superior performance for solar cells," *Optics Express*, vol. 22, p. A282, Jan. 2014.

[99] X. Shen, B. Sun, D. Liu, and S.-T. Lee, "Hybrid heterojunction solar cell based on organic-inorganic silicon nanowire array architecture.," *Journal of the American Chemical Society*, vol. 133, pp. 19408–15, Dec. 2011.

[100] G. Jia, M. Steglich, I. Sill, and F. Falk, "CoreâĂŞshell heterojunction solar cells on silicon nanowire arrays," *Solar Energy Materials and Solar Cells*, vol. 96, pp. 226–230, Jan. 2012.

[101] E. C. Garnett and P. Yang, "Silicon nanowire radial p-n junction solar cells.," *Journal of the American Chemical Society*, vol. 130, pp. 9224–5, July 2008.

[102] L. Tsakalakos, J. Balch, J. Fronheiser, B. A. Korevaar, O. Sulima, and J. Rand, "Silicon nanowire solar cells," *Applied Physics Letters*, vol. 91, no. 23, p. 233117, 2007.

[103] B. Tian, X. Zheng, T. J. Kempa, Y. Fang, N. Yu, G. Yu, J. Huang, and C. M. Lieber, "Coaxial silicon nanowires as solar cells and nanoelectronic power sources.," *Nature*, vol. 449, pp. 885–9, Oct. 2007.

[104] Y. Xia and J. Ouyang, "PEDOT:PSS films with significantly enhanced conductivities induced by preferential solvation with cosolvents and their application in polymer photovoltaic cells," *Journal of Materials Chemistry*, vol. 21, no. 13, p. 4927, 2011.